FACULDADE DE ENGENHARIA DA UNIVERSIDADE DO PORTO

Design and test of the on-board electronics of an Autonomous Solar Aircraft

Teresa Jorge Barbosa Pintão

Mestrado em Engenharia Eletrotécnica e de Computadores

Supervisor: António Pina Martins

Co-supervisor: António Pedro Aguiar

July 27, 2022

Resumo

Tendo como objetivo a redução do consumo de combustíveis fósseis e gás natural, a produção e utilização de energias renováveis tem vindo a aumentar ao longo dos anos, nomeadamente a energia solar. Acompanhada pelo desenvolvimento tecnológico das células solares e do armazenamento de energia através de baterias, a utilização de painéis fotovoltaicos é cada vez mais comum quer a nível doméstico ou industrial, especificamente na indústria aeroespacial e aeronáutica.

O sistema de *Maximum Power Point Tracking* (MPPT) possibilita a operação de um painel fotovoltaico no seu ponto de potência máxima, maximizando a energia produzida conforme as condições de temperatura e irradiância. Apesar da evolução das células fotovoltaicas, a sua baixa eficiência aumenta a necessidade de utilizar um sistema que permita a extração da potência máxima do painel solar.

Esta Dissertação de Mestrado versa sobre o estudo, projeto e desenvolvimento da eletrónica de um veículo aéreo (*Unmanned Aerial Vehicle* - UAV), que está a ser desenvolvido pelo Laboratório C2SR pertencente ao SYSTEC. O UAV será construído com um painel solar de potência máxima igual a 193 W e bateria de Li-ion como fontes de energia.

O trabalho é iniciado com um estudo teórico dos componentes que compõem o sistema elétrico do UAV. Considerando as características dos painéis e baterias a utilizar, é dimensionado um conversor DC/DC abaixador. Foi desenvolvido o algoritmo MPPT, sendo escolhido o método *Perturb and Observe*.

Posteriormente, é utilizado o software MATLAB (Simulink - Simscape Electrical) para simular o sistema elétrico, com o objetivo de validar o algoritmo de MPPT e simular regimes permanentes e transitórios com variação de cargas conectadas em paralelo com a bateria.

Por fim, é apresentada a fase de projeto e implementação do circuito (potência, controlo e condicionamento), incluindo o desenvolvimento da *Printed Circuit Board* (PCB) e a montagem dos componentes. São realizados testes ao protótipo final de modo a verificar a sua operação em malha aberta e fechada, e validar o funcionamento do algoritmo de MPPT em regime permanente, com variação da irradiância e de carga.

O algoritmo de MPPT desenvolvido foi verificado, e foi validado o projeto da PCB protótipo através do seu funcionamento com o nível de potência previsto.

Abstract

Intending to reduce the consumption of fossil fuels and natural gas, the production and use of renewable energies have been increasing over the years, especially solar energy. Due to the technological development of photovoltaic cells and energy storage through batteries, photovoltaic panels are more common in domestic and industrial contexts, specifically in the aerospace and aeronautical industries.

The Maximum Power Point Tracking (MPPT) system enables the operation of a photovoltaic panel at its maximum power point, maximizing the produced energy according to the temperature and irradiance conditions. Despite the evolution of photovoltaic cells, their low efficiency increases the need to use a system that allows maximum power extraction from the solar panel.

This Master's Dissertation approaches the study, design, and development of the electronics of an Unmanned Aerial Vehicle (UAV), which is being developed by the C2SR Laboratory belonging to SYSTEC. The UAV will use a solar panel with a maximum power of 193 W and a Li-ion battery as power sources.

The work begins with a theoretical study of the components of the UAV's electrical system. A step-down DC/DC converter is sized considering the characteristics of the chosen panels and batteries. The MPPT algorithm is developed with the chosen Perturb and Observe method.

Then, MATLAB software (Simulink - Simscape Electrical) is used to simulate the electrical system in order to validate the MPPT algorithm and simulate permanent and transient regimes with variable loads placed in parallel with the battery.

Finally, the circuit design (power, control and conditioning) and implementation are presented, including the Printed Circuit Board (PCB) design and component assembly. The final prototype is tested to verify its operation in open and closed-loop and to validate the MPPT algorithm's operation in steady-state, with load and irradiation variations.

The developed MPPT algorithm was verified, and the prototype PCB design was validated through its operation with the desired power level.

Agradecimentos

Quero agradecer ao meu orientador, Prof. Doutor António Pina Martins, por todo o apoio, disponibilidade e interesse, pela constante partilha de conhecimento, essenciais para o desenvolvimento deste trabalho. Quero também agradecer ao meu co-orientador, Prof. Doutor António Pedro Aguiar por permitir a realização deste projeto.

Quero agradecer aos Engenheiros Pedro Alves e Nuno Guerra pelo suporte dado na parte prática deste trabalho.

Quero agradecer ao Engenheiro Anuj Regmi, membro da equipa do laboratório C2SR, pelo apoio dado ao longo do projeto, mesmo à distância.

À FEUP e a todos os Professores que enriqueceram a minha educação e formação académica.

Aos meus pais, Rosa e Jorge, e à minha irmã Rita que durante toda a minha vida me educaram, motivaram e apoiaram para seguir as minhas escolhas. Foram muito importantes para que conseguisse progredir, alcançar os meus objetivos, e tornar-me na pessoa que sou. Estarei eternamente grata por isso.

Ao João Sá, uma das pessoas que mais me suportou durante este percurso, que me tranquilizou nos momentos menos bons e que tornou esta jornada mais especial e inesquecível.

Aos meus amigos e colegas, que partilharam estes 5 anos comigo e que os tornaram num percurso cheio de alegrias, partilhas e aprendizagens, tanto a nível pessoal como profissional.

Teresa Pintão

"Sê todo em cada coisa.
Põe quanto és no mínimo que fazes."

Fernando Pessoa

Contents

List of Figures

List of Tables

Abbreviations

AC	Alternating Current
BLDC	Brushless DC
BMS	Battery Management System
CC	Constant Current
CCM	Continuous Conduction Mode
CV	Constant Voltage
DCM	Discontinuous Conduction Mode
DC	Direct Current
DC/DC	Direct Current to Direct Current
ESC	Electronic Speed Controller
FMEA	Failure Mode and Effects Analysis
GPS	Global Positioning System
HALE	High Altitude Long Endurance
IC	Integrated Circuit
Li-ion	Lithium-ion
LiPo	Lithium-ion Polymer
MOSFET	Metal Oxide Semiconductor Field Effect Transistor
MPP	Maximum Power Point
MPPT	Maximum Power Point Tracking
PCB	Printed Circuit Board
PMU	Power Management Unit
PWM	Pulse-Width Modulation
P&O	Perturb and Observe
PV	Photovoltaic
SR	Spectral Response
STC	Standard Test Conditions
UAS	Unmanned Aerial System
UAV	Unmanned Aerial Vehicle

Chapter 1

Introduction

1.1 Motivation and Goals

Nowadays, with the increasing global awareness of the environment and rapidly progressive technological advancement in solar cells and batteries, the world is adapting to ecological and sustainable alternatives regarding transportation, energy sources, and industry.

When carefully designed, solar-electrically powered fixed-wing Unmanned Aerial Vehicles (UAVs) exhibit significantly increased flight endurance over purely electrical or gas-powered aerial, with applications ranging from surveillance to pseudo-satellite.

The Cyber-Physical Control Systems and Robotics Laboratory (C2SR-Systec), [1], is currently developing a long endurance solar UAV for seven days of nonstop flight to fly at an altitude above 20 km. This project is being collaborated with multiple research teams in Portugal. Currently, the Laboratory is working on the first prototype to test and develop the concept. The latter will be tested to fly at an altitude of 3000 m and will be able to test multiple electronic equipment in the payload bay.

Specific challenges include the fact that the electronics will be used at lower temperatures and pressure. The best fit size and weight of the on-board electronics must be considered concerning application and performance in coordination with the aircraft design team.

This dissertation aims to contribute to the electronics part of the aircraft, sizing, design, and prototyping of a Maximum Power Point Tracking (MPPT) system.

1.2 Problem Statement

The initial general layout of the electrical system for the aircraft is shown in Figure 1.1. This project includes the study of the colored blocks on the left side of the DC bus in Figure 1.1, namely the photovoltaic (PV) cells, the batteries, the MPPT controller, and the Battery Management System (BMS).

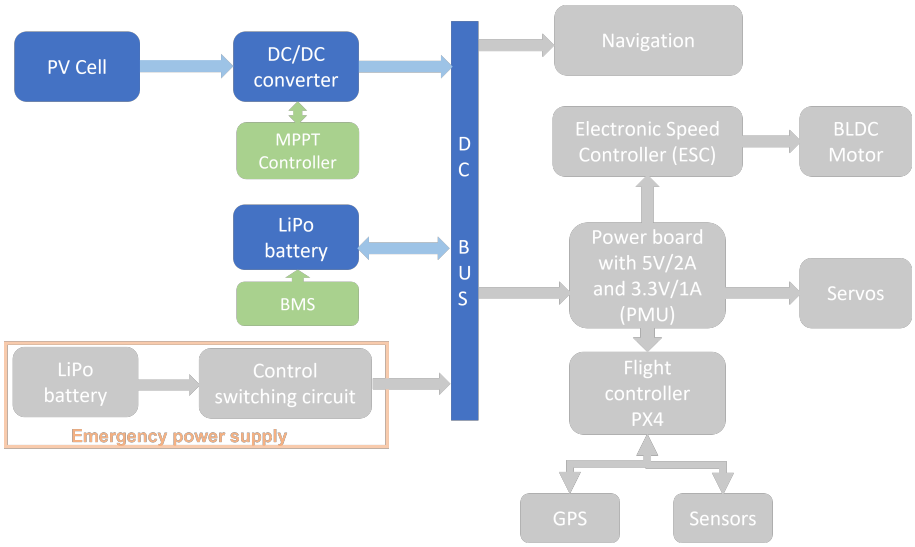

Figure 1.1: Electrical system of the aircraft.

The emergency power supply will allow a safe landing in case of any power failure. This system will be powered by a Lithium Polymer (LiPo) battery, which is safer, easier and faster for this aircraft when compared to a Lithium-ion (Li-ion) battery. The emergency system is controlled by a control switch (possibly a MOSFET) linked to a microcontroller and activated in case of power failure from the main power supply or the PV cells.

Based on the power consumption of the electrical system and the capacity of the emergency battery, this system can be implemented in two different ways:

1. **High current battery pack:** In this option, a high current capacity battery will power all the systems, including the brushless DC motor (BLDC), which will allow bringing the aircraft to any desired location in an emergency. The disadvantage of this system is that it will increase the unusable weight of the aircraft, thus impacting the overall endurance.

2. **Lower capacity battery:** In this option, the autopilot, radio devices, and control actuators (Servos) will be powered, cutting off the BLDC motor from the DC bus. The Global Positioning System (GPS) will be active, and we can receive the GPS location through the telemetry. The battery in this system would be lighter, but with the downside of landing the aircraft in the current area, without the possibility of choosing the landing location.

The initial concept of the solar panel is to turn it as adaptable as possible. Therefore, there will be 10 available rows, as represented in Figure 1.2, each one with 14 SunPower C60 solar cells connected with a interconnect tab, [2]. The connection between the rows will depend on the aircraft dimensions and the necessary output voltage of the panels. The first idea is to have one main solar panel with four rows in series, i.e., 56 cells. Later on, there is the possibility of adding

two panels each with three rows in series, i.e., 42 cells in each additional panel. With every cells in series, it is feasible to use only one MPPT, i.e., a single DC/DC converter.

Figure 1.2: Single row of the solar panel.

1.3 Context

Solar energy was recognized as an alternative energy source in the 1970s. Nowadays, the interest in solar-powered airplanes increased due to the technological progress of high-efficiency solar cells and high energy density batteries. They are ecofriendly, satisfy global environmentalism, and are capable of continuous flight, high altitude and long endurance (HALE) flights.

In this section, a brief history of solar aircrafts, UAVs, and MPPTs will be presented.

1.3.1 Solar Aircrafts

A solar aircraft presents many challenges, such as the energy system (solar cells and batteries), the aerodynamic and propulsion systems, [3].

The first solar-powered airplane, named Sunrise, was designed by Astro Flight, Inc., and it first flew in November 1974 in California. The Sunrise's wing span was 9.8 m, with a gross weight of 12.3 kg. On its first flight, the aircraft reached an altitude of approximately 150 m for about 20 minutes. Back then, the used solar cells had an efficiency of only 10% and total output power of 450 W. The Sunrise survived for 28 flights, but in the last, it was damaged by a sandstorm. Sunrise II was tested in September 1975 with better characteristics: solar cells output power of 600 W with 14 % efficiency and reduced weight to 10.2 kg, [4].

Figure 1.3: Sunrise II solar aircraft, 1975 [4].

The first European solar aircraft was Solaris, built in 1976 in Germany. Over the years, the autonomy of solar aircraft's flight increased. Flying with solar energy was becoming more affordable and efficient due to solar cells and battery developments, creating the chance to perform high altitude and long endurance flights.

In 1999, Helios, developed by AeroVironment, Inc., under NASA's Environmental Research Aircraft and Sensor Technology (ERAST) program, incorporated energy storage for nigh-time flight. It was designated as "eternal airplane", and in 2001 it reached a world record altitude of 29261 m in a 40 minutes flight, [4].

Figure 1.4: Helios solar aircraft, 1999-2003 [5].

In 2007, a Zephyr aircraft from QinetiQ, a British company, exceeded a world record with a 54 h flight, reaching a maximum altitude of 17786 m, [4].

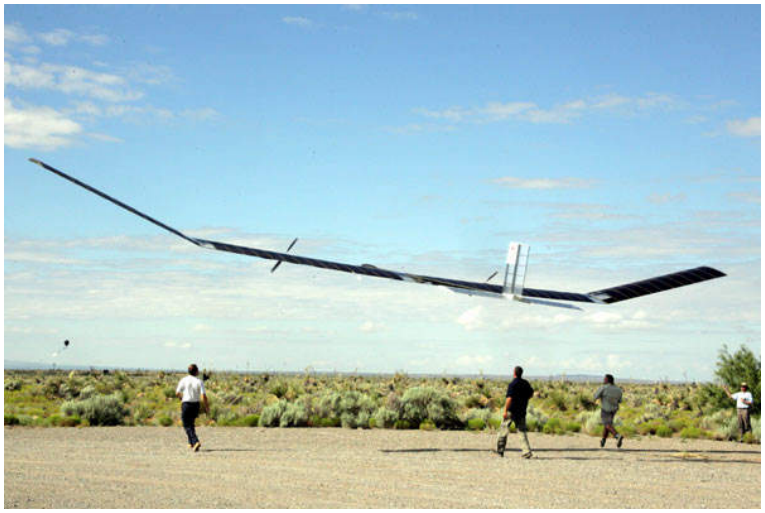

Figure 1.5: Zephyr solar aircraft, 2005-2007 [6].

The examples mentioned above are proof of the feasibility of long endurance flights for unnamed aerial vehicles. On the other hand, continuous flight with a pilot on board is a different ongoing exploration in this area.

Solar Impulse 2, or HB-SIB, is a swiss solar-powered aircraft that took off in 2015 and completed the first round-the-world flight, accomplished by two pilots, with a record of 40 000 km with several stops, [7].

Recently, in August 2021, Skydweller aircraft, by Skydweller Aero, a US-Spanish aerospace company that develops advanced solar-powered aircrafts, is its successor, relying on similar technology but completely autonomous and able to fly continuously for up to 90 days.
With 269.4 m^2 of PV cells, generating 2 kW, and a wingspan of approximately 71.9 m, it will be capable of energy storage through hydrogen fuel cells and fly at a maximum altitude of 13716 m. The tests are still ongoing. [8].

Figure 1.6: Skydweller autonomous solar aircraft [8].

One of the factors that allowed the development of solar-powered aircraft was the outgrowth of the photovoltaics industry. As it can be seen in Figure 1.7, solar cells efficiency has been increased over the years, depending on the technology. The highest registered efficiency is 47.1% for multijunction cells with four or more junctions.

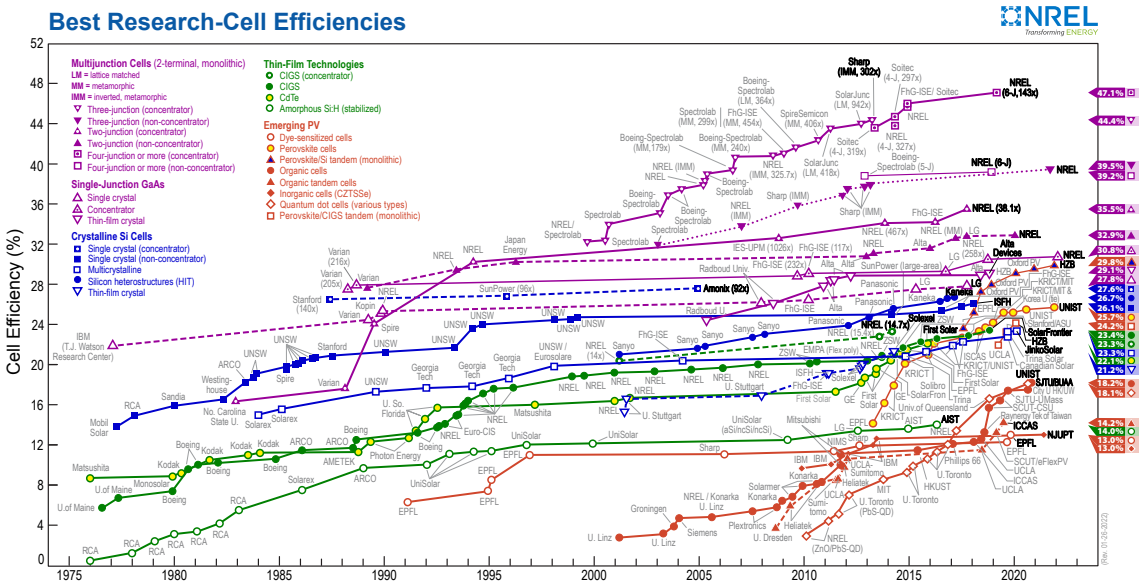

Figure 1.7: Evolution of the highest efficiencies for research cells for a range of photovoltaic technologies since 1976 [9].

1.3.2 Unmanned Aerial Vehicle

The first aircraft not requiring a human pilot dates to 1783, a hot-air balloon launched in France, [10]. An unmanned aerial vehicle can fly autonomously or be piloted remotely. Throughout history, UAVs have been used for many purposes: military, aerial photograph and reconnaissance, aerial target practice, surveillance, terrain mapping and study, real-time inspection (for the offshore wind turbines in Viana do Castelo, for example), and more recently, for personal use, such as small commercial drones. During COVID-19 pandemic, many countries used drones for border controls, disinfection missions and medical supplies deliveries, [11].

1.3.3 MPPT

Although solar cells have been increasing their efficiency, the produced power of a solar cell depends on atmospheric conditions such as irradiance and temperature. The need to extract the maximum power of a solar panel under any conditions is essential, and an MPPT solar charge controller has that function.

In 1985, Australian Energy Research Laboratories (AERL) was founded by Electrical Engineer Stuart Watkinson. He created an electronic unit called "Power Optimizer" that would be able to extract the maximum power from a PV array to assist an electrical bike called "Solar Tandem". This device's first prototype was developed and became the world's first MPPT Solar Charge Controller, also known as AERL MAXIMIZER [12].

Over the years, the MPPT algorithms have been improved, and several advanced commercial MPPT devices are available in the market. Nowadays, MPPTs are more compact, affordable, and have higher efficiency. For example, Genasun GVB-8 Boost controllers are designed to step-up

lower-voltage solar panels to charge higher-voltage lithium batteries with a typical tracking efficiency of 99%, [13]. However, these MPPTs can operate under certain specifications, depending on the PV panel current and voltage and the type and characteristics of the battery.

(a) AERL MAXIMIZER MPPT solar charge controller [12].

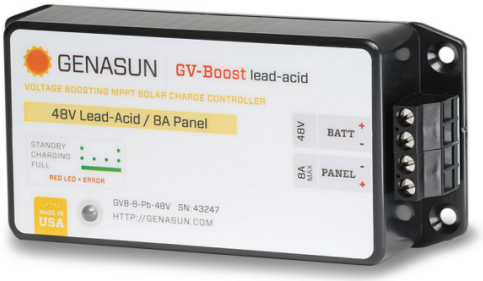

(b) Genasun MPPT solar charge controller [13].

Figure 1.8: Examples of commercial MPPT charge controllers. First (1985) MPPT (a), and current MPPT (b).

1.4 Dissertation Structure

In addition to the Introduction, this dissertation is organized into 4 chapters.

In Chapter 2, it is presented a theoretical background (state of the art) related to the main blocks of the system (PV panels, batteries, DC/DC converters, charge controllers and BMS), a brief presentation of the available alternatives for each one, and a deeper analysis of the chosen components or algorithms. The DC/DC Buck converter is presented in more detail since it is the chosen topology.

In Chapter 3, the system specifications and requirements, and the DC/DC Buck Converter sizing are presented. The electrical system is simulated in steady-state and transient regimes under different conditions, confirming the converter sizing and validating the MPPT algorithm.

In Chapter 4 it is presented the system implementation and prototyping, composed of the PCB design and assembly, and an explanation of the algorithm operation. The experimental results are presented, validating all the previous steps and confirming the prototype operation with the PV panels and an electronic load. Each aforementioned chapters have a brief summary section.

Finally, Chapter 5 presents the conclusions, approaching each work phase and respective results, and proposes future work for this project.

Chapter 2

State of the Art

This chapter will present state of the art and some essential knowledge in order to help the reading and understanding of the document.

2.1 Photovoltaic Panels

2.1.1 Photoelectric Effect

In a photovoltaic panel, there is a conversion of radiated light (solar or other) into electricity. Its generation depends on the dimension and technology of the panel, the radiation received, and the duration of the exposure.

Photons are particles of light, and their energy depends on the frequency (ν) of the radiation according to:

$$E = \frac{hc}{\lambda} = h\nu \tag{2.1}$$

where h is the Planck's constant (6.63 10^{-34} m^2kg/s), c is the speed of light in vacuum (299 792 458 m/s) and λ is the wavelength.

If the photon energy is sufficient to excite the electrons (negatively charged atomic particles) remaining in the material of the panels, usually semiconductors, an electric current is generated. This is called the photovoltaic effect, the conversion of light to electricity, [14].

A light beam can suffer three optical events when reaching a solid surface: reflection, when the light bounces off the object's surface; transmission, when the light passes through the object; and absorption, when the light penetrates the object and remains within it. Therefore, the incident flux is composed of three parts, and not all the incident light is transformed into electrical energy, only the absorbed part, [15].

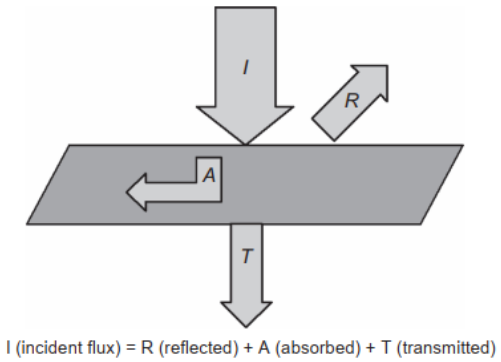

Figure 2.1: Reflection, transmission and absorption of the incident light [15].

2.1.2 Equivalent Circuit of a Photovoltaic Cell and PV Systems

A photovoltaic cell (PV cell) or a solar cell is the fundamental component to form a PV system. A solar cell can be represented through a single diode model, as presented in Figure 2.2. Voltage and current losses are represented by R_s (series resistor) and R_{sh} (shunt resistor), respectively, [16].

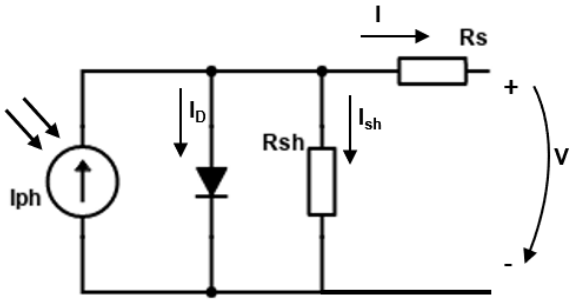

Figure 2.2: Single diode model equivalent circuit.

The output current I is given as:

$$I = I_{ph} - I_D - I_{sh} \tag{2.2}$$

where I_{ph} is a photo-generated current source, I_D is the diode current and I_{sh} is the shunt resistor current.

The Shockley equation expresses the diode current since its I-V characteristic is nonlinear, as illustrated in Equation (2.3), [16].

Replacing the shunt resistor current I_{sh}, the diode current I_D and considering the thermal voltage V_t ($=\frac{kT}{q}$), the Equation (2.2) can be rewritten:

$$I = I_{ph} - I_s\left(e^{\left(\frac{V+R_sI}{nV_t}\right)} - 1\right) - \frac{V+R_sI}{R_{sh}} \tag{2.3}$$

where I_s is the reverse bias saturation current (A), n is the diode ideality factor, q is the electron charge (1.60 x 10^{-19} C), K is the Boltzmann's constant (1.38 x 10^{-23} J/K), T is the absolute temperature (K) at Standard Test Conditions (STC), and V is the cell output voltage.

In order to solve the equation, one needs to quantify I_s and I_{ph}, considering two situations: short circuit and open circuit.

In short circuit (sc), assuming $R_{sh} >> R_s$, $I_D \approx 0$ and the cell output voltage is zero (V=0).

$$I_{sc} = I_{ph} - \underbrace{I_s\left(e^{\frac{V+R_sI}{nVt}} - 1\right)}_{I_D \approx 0} - \underbrace{\frac{V+R_sI}{R_{sh}}}_{\approx 0} \Leftrightarrow I_{sc} = I_{ph} \tag{2.4}$$

Therefore, the short circuit current, I_{sc}, will be approximately equal to I_{ph}, as presented in Figure 2.3 (a).

In open circuit (oc), the cell output current is zero ($I_{oc} = I = 0$), so $I_{ph} = I_D$, as presented in Figure 2.3 (b). Assuming that $R_{sh} >> R_s$, and using the Equation (2.4), it can be consider the following equation:

$$\underbrace{I_{oc}}_{=0} = \underbrace{I_{ph}}_{=I_{sc}} - I_s\left(\underbrace{e^{\frac{V_{oc}+\overbrace{R_sI}^{=0}}{nVt}}}_{>>1} - 1\right) - \underbrace{\frac{V+R_sI}{R_{sh}}}_{\approx 0} \Leftrightarrow I_s = I_{sc}e^{-\frac{V_{oc}}{nVt}} \tag{2.5}$$

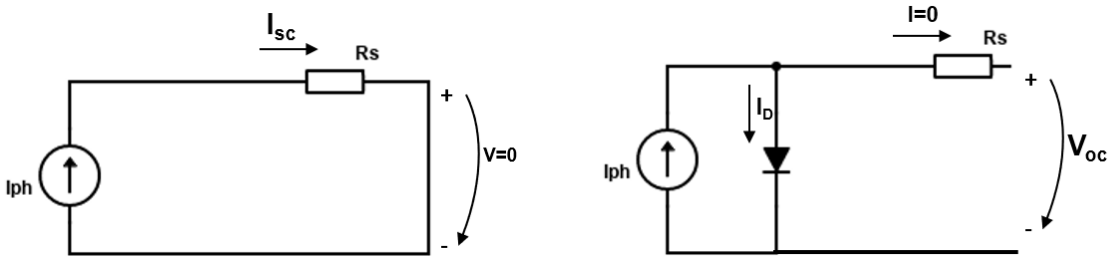

(a) Short circuit (b) Open circuit

Figure 2.3: Single-diode model short circuit and open circuit equivalent circuits.

Concluding, the previous Equation (2.3) can be rewritten as:

$$I = I_{sc} - I_{sc}\left(e^{\frac{V-V_{OC}+R_sI}{nV_t}} - e^{-\frac{V_{oc}}{nV_t}}\right) - \frac{V+R_sI}{R_{sh}} \tag{2.6}$$

where I_{sc} (short circuit current) and V_{oc} (open circuit voltage) are cell parameters. The cell I-V curve can be mathematically estimated through the manipulation of the internal resistors R_s and R_{sh}, the cell temperature and the irradiance.

The fill factor (FF) and the cell efficiency are also important expressions, which formulas are presented in Equation (2.7).

$$FF = \frac{P_{max}}{V_{oc}I_{sc}}$$
$$\eta = \frac{P_{out}}{P_{irradiance}A_{cell}} \tag{2.7}$$

where $P_{irradiance}$ is the irradiance on the cell surface (W/m^2) and A_{cell} is the cell area (m^2).

The efficiency is often measured under reference conditions: solar irradiation of 1000 W/m^2 at a temperature of 25 ºC and under a spectrum AM 1.5, which is a clear sky spectrum used as a reference to measure PV cells, [15].

A photovoltaic module consists of series and parallel solar cells electrically connected. A group of PV modules is called a string, and a group of strings is called an array. Solar PV arrays can have different configurations, such as series or parallel connections. The PV units in growing complexity from a single cell to a solar PV array is shown in Figure 2.4.

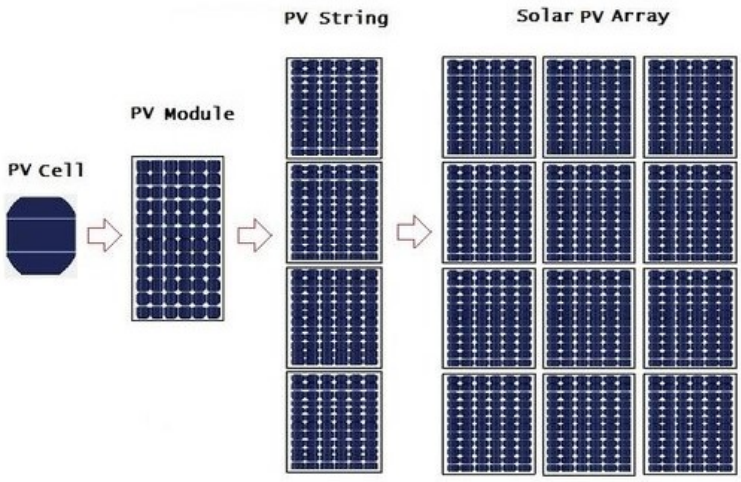

Figure 2.4: PV cell arrangements [17].

The final equation that relates currents and voltages of a PV module with N_p parallel cells and N_s series cells is expressed in the following equation, where, as aforementioned, $I_s = I_{sc}.e^{-\frac{V_{oc}}{n \cdot V_t}}$, [16].

$$I = I_{sc}N_p - I_sN_p\left(exp\left(\frac{\frac{V}{N_s} + \frac{R_s}{N_p}I}{nV_t}\right) - 1\right) - \frac{V\frac{N_p}{N_s} + R_sI}{R_{sh}} \tag{2.8}$$

A PV module is typically integrated with other elements, and the whole constitutes a PV system. There are two main PV installations: grid-connected installations in which the produced energy is sent to the collective grid and stand-alone installations where the produced energy is intended to power certain isolated systems, [15].

The stand-alone systems have different configurations, as illustrated in Figure 2.5.

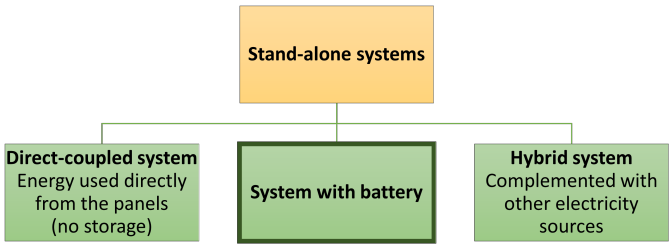

Figure 2.5: Types of PV stand-alone systems.

The stand-alone systems with batteries are the most usual configuration. The battery is a permanent reservoir of energy connected to a charge controller responsible for managing its charge and discharge, which consequently affects the demand and production of energy [15].

Since this dissertation addresses the on-board electronics of an autonomous solar aircraft, the PV system will have a configuration of a stand-alone system with two batteries, the main battery, and the emergency battery.

2.1.3 Solar Panel Technologies

PV material can be classified into two main groups: solid crystalline silicon materials and thin film. Amorphous silicon is a thin-film material. Common PV materials are presented in Table 2.1.

Table 2.1: Common PV materials.

Composition	Acronym
Mono/single crystalline silicon	Mono-c-Si
Multi/poly crystalline silicon	Poly-c-Si
Cadmium Telluride	CdTe
Copper indium gallium selenide	CIGS
Amorphous silicon	a-Si

Current technology shows that crystalline silicon allows higher efficiency. On the other hand, specific thin-film technology allows for low-cost materials and a more straightforward manufacturing process, [18].

One important characteristic of each material is the spectral response (SR), the fraction of useful irradiance according to the wavelength of the incident radiation. Figure 2.6 shows the spectral response concerning different technologies, namely: a-Si (amorphous Silicon); CIS (Copper Indium Selenide); HIT (heterojunction with intrinsic thin layer), composed of a mono thin crystalline silicon wafer surrounded by ultra-thin amorphous silicon layers; p-Si (polycrystalline Silicon);

EFG (Edge-defined Film-fed Growth); CdTe (Cadmium Telluride); and m-Si (monocrystalline Silicon).

As it is illustrated in Figure 2.6, monocrystalline silicon (m-Si) and polycrystalline silicon (p-Si) have a better response in the area with a wavelength of around 700-1100 nm, which includes the wavelength of the red light in the visible light spectrum. Amorphous silicon (a-Si) has a better response in the area with a wavelength of 450-650 nm, which corresponds approximately to the wavelength of the purple and blue light in the visible light spectrum, as shown in Figure 2.7.

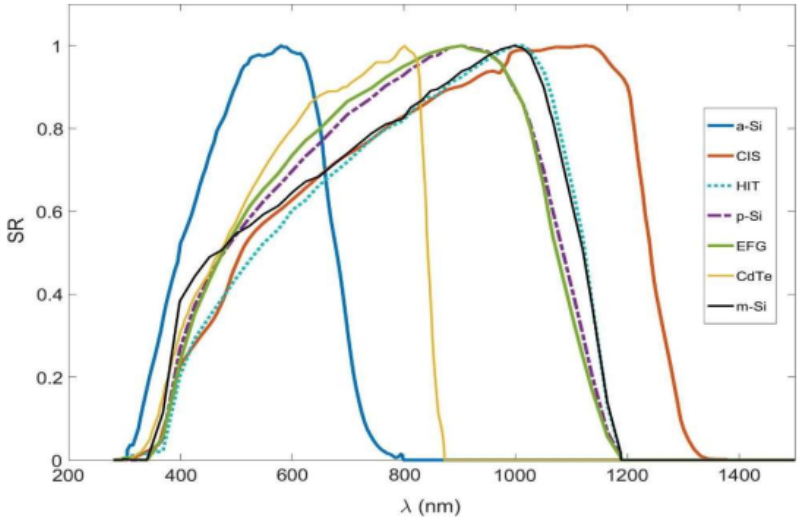

Figure 2.6: Spectral Response of different technologies [19].

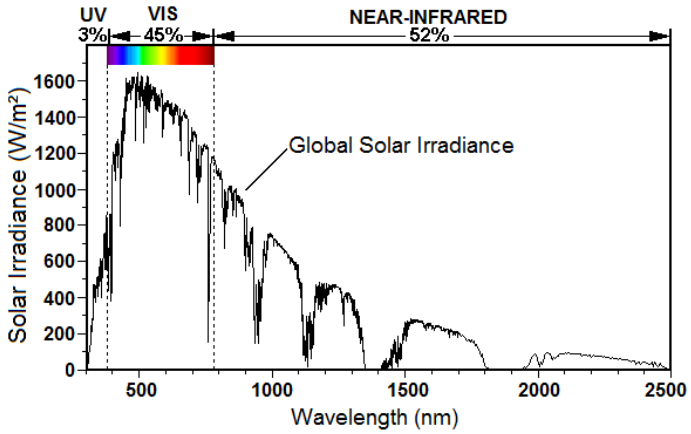

Figure 2.7: Solar spectrum [20].

2.1.4 C60 Solar Cells

The aircraft's solar cells will be SunPower C60 monocrystalline silicon solar cells, with electrical characteristics at STC given in Table 2.2. These cells deliver a high efficiency and performance, maximum light capture, broad spectral response and a flexible arrangement in the wingspans, [2].

Table 2.2: Electrical characteristics of the C60 cell at STC: 1000 W/m^2, AM 1.5 g and Cell Temperature 25 ºC [2].

$\eta(\%)$	$P_{mpp}[W_p]$	$V_{mpp}[V]$	$I_{mpp}[A]$	$V_{oc}[V]$	$I_{sc}[A]$
22.5	3.42	0.582	5.93	0.687	6.28

C60 cell I-V curve is shown in Figure 2.8, depending on the irradiance with 25 ºC or 50 ºC. Figure 2.9 illustrates the cell's excellent performance with radiation's wavelength length of ≈ 400-1050nm, which practically covers the visible light part of the solar spectrum (≈380-750nm).

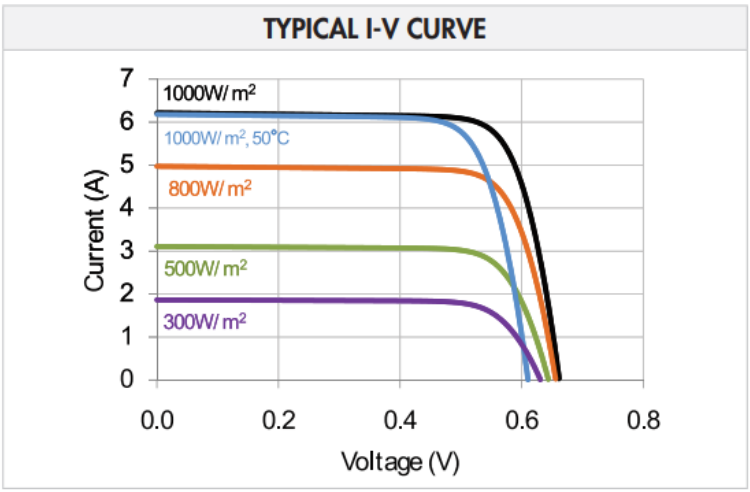

Figure 2.8: SunPower C60 solar cell characteristics: Typical I-V curve [2].

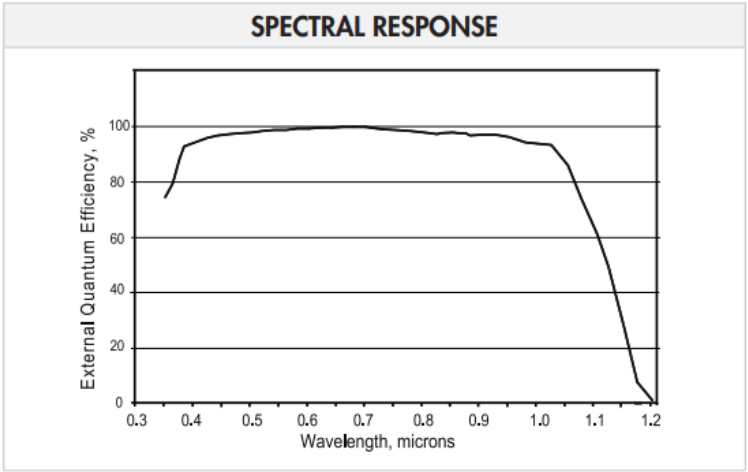

Figure 2.9: SunPower C60 solar cell characteristics: Spectral Response [2].

2.1.5 Bypass Diodes

Single solar cells can be placed in series, meaning that the same current will pass through all the cells. In this case, if one or more cells are shaded, they will not be able to produce much current as the others, so the current will be limited by the cell that produces less current.

To prevent this problem, a solution may be implemented with bypass diodes connected in parallel, with opposite polarity, to all singles cell or a set of cells, allowing the current to pass around shaded cells. Under normal conditions, the bypass diode will be reverse biased. A certain leakage current may exist and reduce the solar module efficiency, but the bypass diodes are still beneficial, [15].

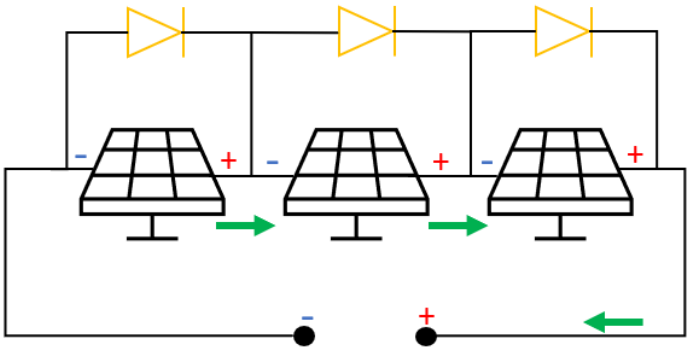

Figure 2.10: Normal operation with bypass diodes.

Under shading, the harmed cell will generate a reverse voltage, and the bypass diode will be forward biased, creating an alternative path for the current to flow. Therefore, the solar string only loses part of the produced power.

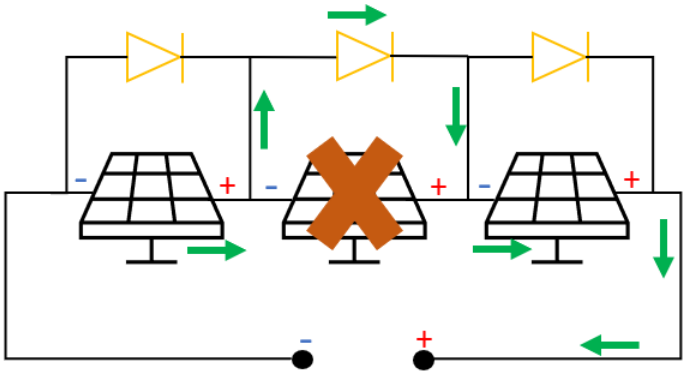

Figure 2.11: Shading condition with bypass diodes.

In this project, for a first prototype, bypass diodes will not be implemented but are an improvement that may be considered in the future.

2.2 Batteries

The two batteries, main and emergency ones, are essential to the energy system of the solar aircraft. The following section will present several fundamental battery properties and their common materials.

2.2.1 Properties

According to [21], several properties describe the performance of a battery: capacity, efficiency and overcharge; discharge and charge rate; depth of discharge and state of charge; self-discharge rate; and life cycle and maximum lifetime.

2.2.1.1 Capacity, Efficiency and Overcharge

Battery capacity is measured in Ampere-hour (Ah). The charge efficiency (or Ah efficiency) is illustrated through the Equation (2.9).

$$C_{eff} = \frac{Ah\ discharged}{Ah\ required\ for\ complete\ recharge} \tag{2.9}$$

The electrical stored energy is measured in Watt-hour (Wh). The energy efficiency of a rechargeable battery is presented in Equation (2.10).

$$E_{eff} = \frac{energy\ discharged}{energy\ required\ for\ complete\ recharge} \tag{2.10}$$

The battery capacity is not constant since it depends on certain conditions such as the voltage to which the battery is discharged, also called the end voltage, the battery discharge current, and the battery temperature (at low temperature, the battery capacity is reduced).

Overcharge is the excess Ah delivered to recharge the battery, [21].

2.2.1.2 Discharge Rate and Charge Rate

These properties are convenient for comparing currents at which batteries are charged or discharged.

$$Rate = \frac{Capacity\ (Ah)}{Time\ (h)} \tag{2.11}$$

2.2.1.3 Depth of Discharge and State of Charge

Depth of discharge (DoD) is complementary to the state of charge (SoC): the DoD is the percentage of capacity that has been used from the fully charged battery; SoC is the capacity percentage of the fully charged battery still available.

2.2.1.4 Self-Discharge Rate

Self-discharge is the lost charge when the battery is left at open circuit for a substantial time, i.e., without being used. For rechargeable batteries, this property is defined as a percentage of capacity lost per month according to the battery temperature, [21].

2.2.1.5 Life Cycle and Maximum Lifetime

The life cycle is the number of cycles a battery can deliver during its useful life, i.e., before the battery capacity reaches a certain percentage of the total charge. One cycle is equivalent to one discharge followed by one recharge.

The maximum lifetime estimates the time, generally in years, before the battery capacity reaches a certain percentage of the total charge. It is typically used in standby applications in which the batteries are not permanently in service, [21].

In a PV system, since the PV modules produced energy is variable according to the weather conditions, the battery might not have a regular charging cycle.

2.2.2 Types and Materials

This section will focus on the various types of batteries used in PV-battery systems.

According to [22] the most widely available batteries are:

- Lead-acid (LA)
- Nickel-cadmium (NiCd)
- Nickel-metal hydride (NiMH)
- Lithium-ion (Li-ion)
- Lithium-based cells, Lithium-sulfur (Li-S)
- Lithium-ion Polymer (LiPo)

Table 2.3: Different battery type characteristics. Based on [23, 24, 25].

Characteristic \ Type	LA	NiCd	NiMH	Li-ion	LiPo
Specific energy [Wh/kg]	25-50	50-60	60-120	75-250	125-300
Specific power [W/kg]	75-300	≈ 200	250-1000	500-1000	≈ 500
Self discharge	Low	High	High	Medium	Low
Cycle life [100% DOD]	200-1000	> 1500	180-2000	> 1000	similar to Li-ion
Nominal Cell Voltage [V]	2	1.2	1.2	3.7	3.7

As it is shown in Table 2.3, when compared to the others, Lead-acid (LA) have low self-discharge but low cycle life as well as low energy and power density.

Nickel-cadmium (NiCd) batteries are characterized by higher energy and power densities, and a better life cycle than LA batteries [22]. However, NiCd batteries are toxic due to the presence of Cadmium, so they must be properly recycled. This battery's operating temperatures are from -10 ºC to +40 ºC. Nickel-metal hydride (NiMH) is considered an improvement of NiCd batteries since they have higher energy and power density. The operating range temperature for these batteries is from -20 ºC to +40 ºC. However, the price per kWh is much higher than the others. [21].

Li-ion batteries have high energy density and efficiency. Their cycle life depends on the material such as Li-ion manganese oxide (LMO), Li-iron-phosphate (LFP) or Li-titanate-oxide (LTO), [23].

Among Lithium-based cells, Lithium-sulfur (Li-S) can store more energy than Li-ion but they have a low number of recharge cycles. Charging Li-S batteries degrades the cells and shortens their lifespan. Scientific investigations took place to increase the number of charging cycles and turn Li-S batteries commercially viable. Nowadays, Li-S charge and discharge cycles are being improved, increasing the cycle life of the battery and thus, creating the possibility to commercialize it, [26].

Lithium-ion Polymer (LiPo) battery is a rechargeable Li-ion battery. Lithium batteries have a barrier separating the anode and cathode, and in LiPo batteries, that barrier contains a polymer electrolyte. The construction of a LiPo battery allows a high energy density and less weight. As it is shown in Figure 2.12, comparing the LiPo batteries with the established technologies, namely the Li-ion, the first one has a higher and broader range of energy density (Wh/kg) and practically the same volumetric energy (Wh/L).

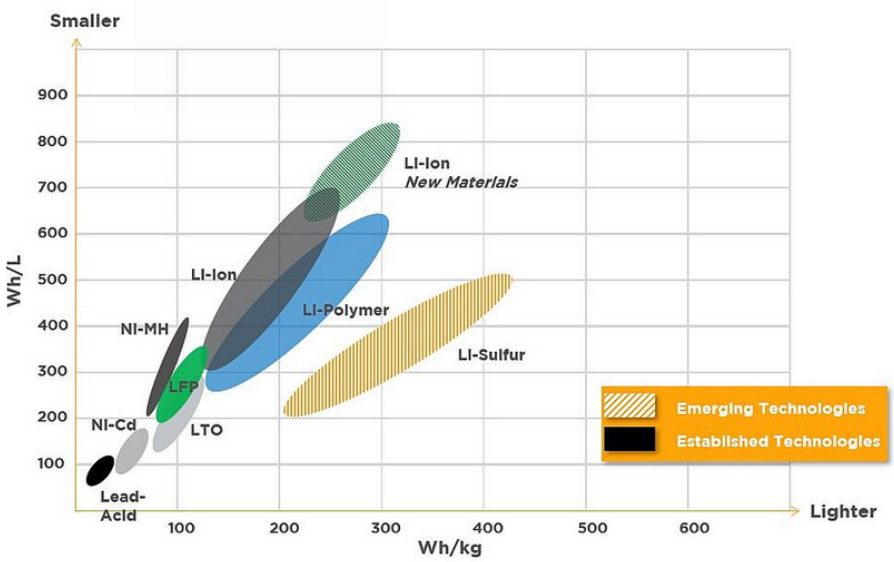

Figure 2.12: Batteries chemistry comparison chart [24].

2.3 DC/DC Converters

Switching converters require a switch such as BJT, IGBT, or a MOSFET that controls the power flow from the input source. They have higher efficiency than linear sources since their components have lower losses. Usually, solar systems use a DC/DC converter to increase or decrease the solar panels' voltage.

In this project, the energy conversion is a fundamental part of the energy system, assigned to the non-isolated DC/DC converter present in the system, Figure 1.1.

An isolated converter separates the circuit into two sections, physically and electrically, preventing current flow between the two, until certain voltage levels. The galvanic isolation is typically achieved by using a transformer, allowing power transfer using electromagnetic energy. However, non-isolated converters are less expensive, have a smaller size and weight, which is essential in this project, and are usually more efficient, [27]. Regarding this project specifications, isolation is not required, thus a non-isolated converter is suitable for the system.

The buck converter is controlled by a microcontroller, which will be programmed with the algorithm. It is important to understand its operation and fundamental equations either in steady-state and transient conditions. In any ideal DC/DC converter, it can be considered that the input power is equal to the output power, but this is a very simple approach to its operation.

It is first reviewed the main non-isolated DC/DC converter topologies using ideal models. Then, more realistic models are considered in order to obtain more reliable results.

2.3.1 DC/DC Boost Converter

A DC/DC boost converter (or a step-up) aims to generate an output voltage higher than the input voltage. Considering an efficiency of 100%, the input current will be higher than the output current.

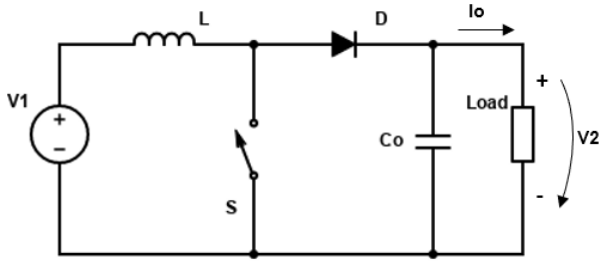

Figure 2.13: Circuit diagram of Boost converter.

In continuous conduction mode (CCM), there are two possible states according to the switch position, ON or OFF. When the switch is ON, the diode will be reverse biased, and the inductor will store energy, increasing its current. When the switch is OFF, the diode will be ON, the inductor current will decrease, and the current will flow to the output capacitor and load. These two states alternate with the switching through a control signal, a PWM signal with a defined duty-cycle (D) and frequency ($f = \frac{1}{T}$).

In the following analysis, it is assumed a lossless inductor and an ideal switch and diode. During one period T, it is possible to obtain the relations in Equation (2.13), where v_L is the voltage across the inductor and with $T = t_{on} + t_{off}$, the duty-cycle is defined as:

$$D = \frac{t_{on}}{t_{on} + t_{off}} \tag{2.12}$$

$$\begin{cases} [0,\ DT] : v_L = V_1 \\ [DT,\ T] : v_L = V_1 - V_2 \end{cases} \tag{2.13}$$

In steady-state, the average inductor voltage is zero ($v_{L,avg} = 0$), and through mathematical manipulation, one can get the ideal relation between input and output voltage according to the duty-cycle.

$$\frac{V_2}{V_1} = \frac{1}{1-D} \tag{2.14}$$

For the currents, and assuming a load resistor R_o, it is obtained:

$$I_L = i_{L,avg} = \frac{I_o}{1-D} = \frac{V_2}{R_o(1-D)} \tag{2.15}$$

In discontinuous conduction mode (DCM) or when including parasitic elements (in the switches or in the inductor) the voltages and currents relations are more complex, [28].

2.3.2 DC/DC Buck-Boost Converter

Buck-boost converter can generate an inverted output voltage higher or lower than the input voltage, which can be an advantage in some conditions.

The same analysis, with ideal components, is done in CCM. When the switch is ON, the inductor will store energy, increasing its current, and the diode is reversed biased. When the switch is OFF, the diode starts conducting, the inductor current decreases and flows to the output capacitor and load.

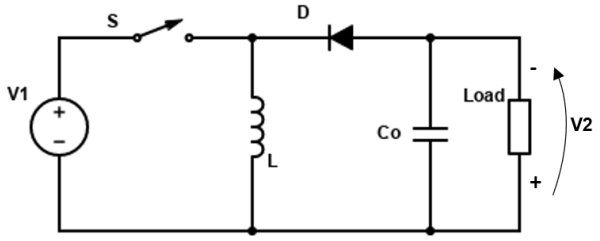

Figure 2.14: Circuit diagram of a Buck-Boost converter.

During one period T, it is possible to obtain the following relations:

$$\begin{cases} [0,\ DT] : v_L = V_1 \\ [DT,\ T] : v_L = -V_2 \end{cases} \tag{2.16}$$

Knowing that $v_L = L\frac{di_L}{dt}$ and considering a steady-state condition:

$$\frac{V_1}{L}t_{on} = \frac{V_2}{L}t_{off} = \Delta I_L \Leftrightarrow V_2 = V_1\frac{t_{on}}{t_{off}} \tag{2.17}$$

The final result is:

$$\frac{V_2}{V_1} = \frac{D}{1-D} \tag{2.18}$$

Contrarily to the boost converter, the current supplied by the input source is a highly pulsed one, which can be a disadvantage in some conditions.

2.3.3 DC/DC Cuk Converter

Similar to a buck-boost converter, the Cuk converter generates an inverted output voltage higher or lower than the input voltage. It consists of two inductors, two capacitors, one diode, and one switch. This converter was designed to overcome the drawbacks of the buck-boost, such as a high output current ripple and discontinuous input current, [27].

The analysis in CCM is as follows. When the switch is ON, the diode is reverse biased and L1 will charge. If C1 is charged, the current will flow to C2 and the load, charging L2. C1 acts as a voltage source. When the switch is OFF, L1 will discharge, and the current will flow from the source to C1. If L2 is charged, it will dissipate its energy to the output capacitor and the load along with L1, [29].

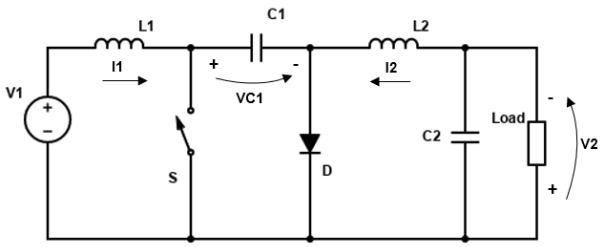

Figure 2.15: Circuit diagram of a Cuk converter.

$$\begin{cases} [0,\ DT] : v_{L1} = V_1,\ v_{L2} = -V_{C1} + V_{C2} \\ [DT,\ T] : v_{L1} = V_1 - V_{C1},\ v_{L2} = V_2 \end{cases} \tag{2.19}$$

In steady-state, the average voltage value in the inductors is zero and considering $V_2 = V_{C2}$:

$$\begin{cases} v_{L1,avg} = \frac{V_1 t_{on} + (V_1 - V_{C1}) t_{off}}{T} \Leftrightarrow 0 = V_1\ D + (V_1 - V_{C1})(1-D) \Leftrightarrow V_{C1} = \frac{V_1}{(1-D)} \\ v_{L2,avg} = \frac{(-V_{C1} + V_{C2}) t_{on} + V_2 t_{off}}{T} \Leftrightarrow 0 = (-V_{C1} + V_{C2})D + V_2(1-D) \Leftrightarrow V_2 = V_{C1} D \end{cases} \tag{2.20}$$

Then, one can conclude that

$$\frac{V_2}{V_1} = \frac{D}{1-D} \tag{2.21}$$

2.3.4 DC/DC Buck Converter

The purpose of a buck converter (or a step-down) is to lower the input voltage of an unregulated DC supply to a lower stable output voltage. The ideal DC/DC buck converter is composed by a diode (D), an inductance (L), a capacitor (C) and a switch (S). The input voltage will be named V_1 and the output voltage V_2, as it is presented in Figure 2.16 (a). With ideal components, the converter DC gain is defined by the equation:

$$\frac{V_2}{V_1} = D \tag{2.22}$$

In reality, the circuit in Figure 2.16 (a) is not ideal, as presented in Figure 2.16 (b), and has the following non-ideal components: R_S (equivalent resistor of switch S, e.g. a MOSFET), V_D (voltage drop in diode D) and R_L (parasitic resistor of inductor L).

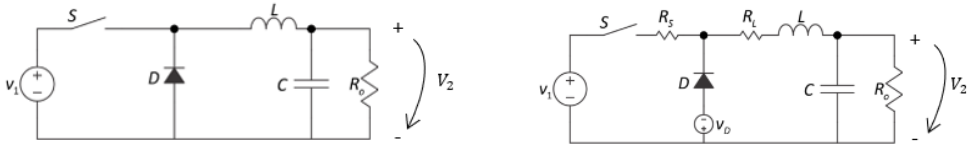

(a) Ideal DC/CDC buck converter.

(b) DC/DC buck converter with non-ideal components.

Figure 2.16: Ideal and non-ideal DC/DC Buck converters. Adapted from [30].

Considering the non-ideal model and using circuit analysis, one concludes that according to the switch position, ON or OFF, controlled by a PWM control signal, the circuit has two different states, presented in Figure 2.17, respectively.

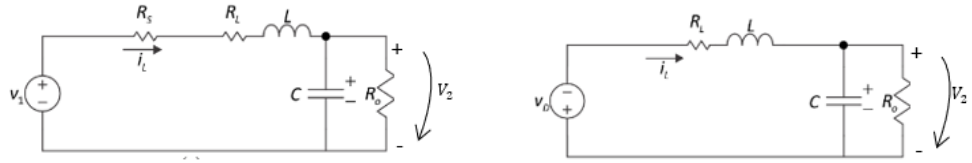

(a) Equivalent circuit with switch S ON.

(b) Equivalent circuit with switch S OFF

Figure 2.17: Operation states of non-ideal DC/DC Buck converter. Adapted from [30].

In the first state, the switch is closed, the diode is reverse biased and will behave like an open circuit. In the second state, the switch is open and the diode conducts. These two states alternate with the switching through a control signal, a PWM signal with a defined duty-cycle and frequency.

From this point onward, it will be considered that the converter is operating in CCM, with a constant frequency f, and D is the duty-cycle for the switch operation where $D \subset [0,1]$.

$$\begin{cases} [0,\ DT] \rightarrow S\ ON,\ D\ OFF \\ [DT,\ T] \rightarrow S\ OFF,\ D\ ON \end{cases} \tag{2.23}$$

Therefore, it is assumed that the first stage of operation, represented in Figure 2.17 (a), corresponds to the time interval $[0,\ DT]$ and the second stage of operation, represented in Figure 2.17 (b), corresponds to the time interval $[DT, T]$, knowing that T is the period of each cycle.

The first stage operation is represented by the following differential equations:

$$\begin{aligned} L\frac{di_L}{dt} &= -i_L(R_s + R_L) - v_2 + v_1 \\ C\frac{dv_c}{dt} &= i_L - \frac{v_c}{R_o} \end{aligned} \tag{2.24}$$

Both equations, 2.24, can be transformed into a matrix (state-space) representation and multiplied by D.

$$\begin{bmatrix} D \cdot L\frac{di_L}{dt} \\ D \cdot C\frac{dv_c}{dt} \end{bmatrix} = \begin{bmatrix} D \cdot (-R_s - R_L) & -D \\ D & -\frac{D}{R_o} \end{bmatrix} \begin{bmatrix} i_L \\ v_c \end{bmatrix} + \begin{bmatrix} D \cdot v_1 \\ 0 \end{bmatrix} \tag{2.25}$$

The second stage operation is represented by the following equations:

$$\begin{aligned} L\frac{di_L}{dt} &= -R_L \cdot i_L - v_c - v_D \\ C\frac{dv_c}{dt} &= i_L - \frac{v_c}{R_o} \end{aligned} \tag{2.26}$$

In the same way, both equations, 2.26, can be transformed into a matrix representation and multiplied by $(1-D)$.

$$\begin{bmatrix} (1-D) \cdot L\frac{di_L}{dt} \\ (1-D) \cdot C\frac{dv_c}{dt} \end{bmatrix} = \begin{bmatrix} (1-D)(-R_L) & -(1-D) \\ (1-D) & -\frac{(1-D)}{R_o} \end{bmatrix} \begin{bmatrix} i_L \\ v_c \end{bmatrix} + \begin{bmatrix} -(1-D) \cdot v_D \\ 0 \end{bmatrix} \tag{2.27}$$

Summing the two matrices 2.25 and 2.27, by applying the technique of the average model in state-space, it is obtained:

$$\begin{bmatrix} L\frac{di_L}{dt} \\ C\frac{dv_c}{dt} \end{bmatrix} = \begin{bmatrix} -D \cdot R_s - R_L & -1 \\ 1 & -\frac{1}{R_o} \end{bmatrix} \begin{bmatrix} i_L \\ v_c \end{bmatrix} + \begin{bmatrix} D \cdot v_1 - (1-D) \cdot v_D \\ 0 \end{bmatrix} \tag{2.28}$$

Therefore, the model represented in Figure 2.18 can be represented by the following two equations:

$$\begin{aligned} L\frac{di_L}{dt} &= -(D\cdot R_s + R_L)i_L - v_c + D\cdot v_1 - (1-D)\cdot v_D \\ C\frac{dv_C}{dt} &= i_L - \frac{v_c}{R_o} \end{aligned} \tag{2.29}$$

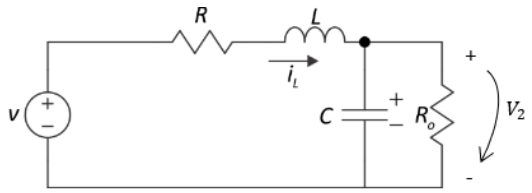

Figure 2.18: Equivalent circuit of DC/DC Buck converter. Adapted from [30].

Where $V = D\cdot v_1 - (1-D)\cdot v_D$ and $R = D\cdot R_s + R_L$.

This model, obtained using the average model in state-space, is valid for the steady-state regime. [30]

In steady-state, it is known that the average value of the inductor voltage is zero and the average value of the capacitor current is also zero. The equivalent circuit for steady-state is represented in Figure 2.19.

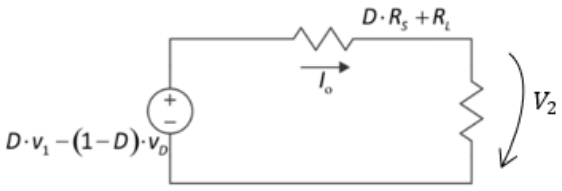

Figure 2.19: Equivalent circuit of DC/DC Buck converter in steady-state. Adapted from [30].

Using circuit analysis, it is possible to get the current I_o and then, replacing its expression in the equation $V_2 = R_o \cdot I_o$, the following equations are obtained:

$$\begin{aligned} I_o &= \frac{D\cdot v_1 - (1-D)\cdot v_D}{D\cdot R_s + R_L + R_o} \\ V_2 &= \frac{R_o\,[D\cdot v_1 - (1-D)\cdot v_D]}{D\cdot R_s + R_L + R_o} \end{aligned} \tag{2.30}$$

The voltage gain, i.e., the quotient between the output and the input voltage, as a function of the load resistor R_o, is defined as:

$$G = \frac{V_2}{V_1} = \frac{R_o[D - (1-D)\frac{v_D}{v_1}]}{D\cdot R_s + R_L + R_o} \tag{2.31}$$

In an ideal converter, where $R_s = R_L = v_D = 0$, the gain is defined as:

$$G = \frac{V_2}{V_1} = D \tag{2.32}$$

Analyzing the ideal circuit in one period T, it is possible to confirm that:

$$\begin{cases} [0;\ DT] : -V_1 + v_L + V_2 = 0 \Leftrightarrow v_L = V_1 - V_2 > 0 \\ [DT;\ T] : v_L = -V_2 \ \ (assuming\ that\ \ v_D = 0) \end{cases} \tag{2.33}$$

2.3.4.1 Load Voltage Dynamics

The aforementioned matrices that represent the two stages of operation, Equation (2.25) and Equation (2.27), are equivalent to the following matrices:

$$\begin{aligned} \underbrace{\begin{bmatrix} \frac{di_L}{dt} \\ \frac{dv_c}{dt} \end{bmatrix}}_{\dot{x}} &= \underbrace{\begin{bmatrix} -\frac{R_s+R_L}{L} & -\frac{1}{L} \\ \frac{1}{C} & -\frac{1}{R_o \cdot C} \end{bmatrix}}_{A_1} \underbrace{\begin{bmatrix} i_L \\ v_c \end{bmatrix}}_{x} + \underbrace{\begin{bmatrix} \frac{v_1}{L} \\ 0 \end{bmatrix}}_{B_1} \\ \underbrace{\begin{bmatrix} \frac{di_L}{dt} \\ \frac{dv_c}{dt} \end{bmatrix}}_{\dot{x}} &= \underbrace{\begin{bmatrix} -\frac{R_L}{L} & -\frac{1}{L} \\ \frac{1}{C} & -\frac{1}{R_o \cdot C} \end{bmatrix}}_{A_2} \underbrace{\begin{bmatrix} i_L \\ v_c \end{bmatrix}}_{x} + \underbrace{\begin{bmatrix} \frac{v_D}{L} \\ 0 \end{bmatrix}}_{B_2} \end{aligned} \tag{2.34}$$

In order to simplify the analysis for obtaining the load voltage dynamics, it will be considered that $v_D = R_s = 0$.

Furthermore, the following definitions in Equation (2.35) will be considered, where X is state vector and D represents the duty-cycle for an operating point. The variables $\bar{x}$ and $\bar{d}$ represent small variations around a defined operating point. [30]

$$\begin{aligned} x &= X + \bar{x} \\ d &= D + \bar{d} \end{aligned} \tag{2.35}$$

Assuming a state-space representation and applying the Laplace transform:

$$\begin{aligned} \frac{d\bar{x}}{dt} &= A \cdot \bar{x} + B \cdot U \cdot \bar{d} \\ \bar{x}(s)[sI - A] = B \cdot U \cdot \bar{d}(s) &\Leftrightarrow \bar{x}(s) = [sI - A]^{-1} \cdot B \cdot U \cdot \bar{d}(s) \end{aligned} \tag{2.36}$$

And considering matrices 2.34 and $v_D = R_s = 0$, it can be concluded that $A_1 = A_2$. Therefore, the following equations are obtained.

$$\begin{aligned} [sI - A] &= \begin{bmatrix} s + \frac{R_L}{L} & \frac{1}{L} \\ -\frac{1}{C} & s + \frac{1}{R_o \cdot C} \end{bmatrix} \\ [sI - A]^{-1} &= \frac{1}{M(s)} \begin{bmatrix} L(1 + C \cdot R_o \cdot s) & C \cdot R_o \\ L \cdot R_o & R_o \cdot C(R_L + L \cdot s) \end{bmatrix} \\ M(s) &= \frac{1}{R_o + R_L + L \cdot s + C \cdot R_o \cdot R_L \cdot s + L \cdot C \cdot R_o \cdot s^2} \end{aligned} \tag{2.37}$$

$$B \cdot U \cdot \bar{d}(s) = \begin{bmatrix} \frac{v1 \cdot \bar{d}(s)}{L} \\ 0 \end{bmatrix} \tag{2.38}$$

Concluding, in order to obtain $\bar{x}$, $[sI-A]^{-1}$ and $B\cdot U\cdot \bar{d}(s)$ are multiplied:

$$\bar{x}(s)=\begin{bmatrix}\bar{i_L}(s)\\ \bar{v_c}(s)\end{bmatrix}=\frac{1}{M(s)}\cdot\begin{bmatrix}v_1(1+C\cdot R_o\cdot s)\bar{d}(s)\\ v_1\cdot R_o\cdot\bar{d}(s)\end{bmatrix} \tag{2.39}$$

From Equation (2.39), assuming $R_o >> R_L$ and expanding the expression $M(s)$, one concludes that:

$$\begin{aligned}\bar{v_c}(s)&=\frac{v_1\cdot R_o\cdot\bar{d}(s)}{M(s)}\Leftrightarrow\frac{\bar{v_c}(s)}{\bar{d}(s)}=v_1\frac{R_o}{M(s)}\\ \frac{\bar{v_c}(s)}{\bar{d}(s)}&=v_1\cdot\frac{1}{L\cdot C\left[s^2+s\left(\frac{1}{C\cdot R_o}+\frac{R_L}{L}\right)+\frac{1}{L\cdot C}\right]}\end{aligned} \tag{2.40}$$

Assuming $\omega_o=\frac{1}{\sqrt{L\cdot C}}$ and $\zeta=\frac{\frac{1}{C\cdot R_o}+\frac{R_L}{L}}{2\omega_o}$, it is possible to obtain a final transfer function that relates the load voltage response with a small variation in the duty-cycle, around an operating point, presented in Equation (2.41).

$$\frac{\bar{v_c}(s)}{\bar{d}(s)}=\frac{v_1\cdot\omega_o^2}{s^2+2\zeta\omega_o\cdot s+\omega_o^2} \tag{2.41}$$

Using this equation, the parameters of the output voltage controller can be defined.

2.3.4.2 Current Control

It will be useful to control the value of the inductance current, I_L, in order of the duty-cycle D, obtaining a transfer function F:

$$F(s)=\frac{\overline{i_L}(s)}{\overline{d}(s)} \tag{2.42}$$

The system in Figure 2.20 represents a way of controlling the inductance current through the switch operation. The ideal voltage source V_2 replaces the capacitor C and the load resistor R_o.

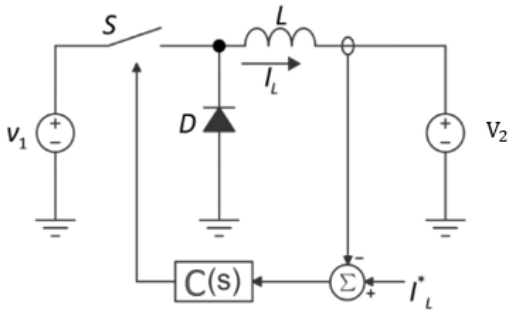

Figure 2.20: Current control for Buck converter with a controller C(s). Adapted from [30].

Then, using equations 2.29, and considering D variable in time, in order to achieve a final transfer function, a differential linear equation should be considered. Through mathematical manipulation, it is possible to obtain the Equation (2.43).

$$L\frac{d\bar{i_L}}{dt} = -(D \cdot R_s + R_L) \cdot \bar{i_L} - \bar{D} \cdot R_s \cdot I_o + \bar{D} \cdot (v_1 + v_D) \tag{2.43}$$

Applying the Laplace transform in all terms and organizing the terms, one gets:

$$\frac{\overline{i_L}(s)}{\overline{d}(s)} = \frac{(v_1 + v_D) - R_s \cdot I_o}{s \cdot L + (D \cdot R_s + R_L)} \tag{2.44}$$

Knowing that $D \cdot (v_1 + v_D) = D \cdot R_s \cdot I_o + v_2$ and assuming $\tau = \frac{L}{D \cdot R_s + R_L}$, it is obtained the final transfer function:

$$\frac{\overline{i_L}(s)}{\overline{d}(s)} = \frac{V_2}{L \cdot D \cdot (s + \frac{1}{\tau})} \tag{2.45}$$

When considering an ideal converter, $R_s = R_L = 0$, τ becomes an indetermination and tends to infinite. Therefore, considering $\frac{V_2}{D} = V_1$, $\frac{1}{\tau} = 0$ and the last equation becomes:

$$\frac{\overline{i_L}(s)}{\overline{d}(s)} = \frac{V_2}{L \cdot D \cdot s} = \frac{V_1}{L \cdot s} \tag{2.46}$$

According to Equation (2.45) the plant model is a first order equation and the design of the current controller is quite straightforward.

2.3.5 DC/DC Bidirectional Buck Converter

Unidirectional converters are used to interface with unidirectional power sources. However, depending on the system's characteristics and requirements, a bidirectional converter could be used for the battery charging and discharging operations. An ideal bidirectional converter has a similar structure as shown in Figure 2.16 (a) except that the switch (S) and diode (D) are replaced by a MOSFET with an anti-parallel diode, as it is shown in Figure 2.21.

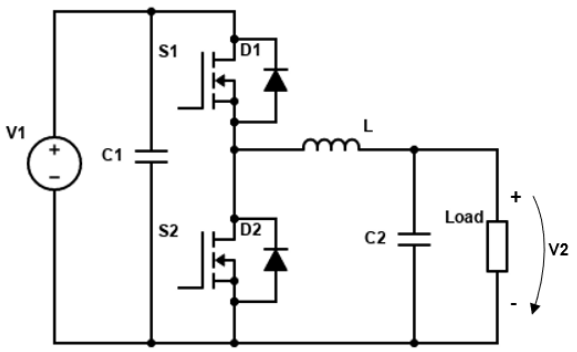

Figure 2.21: Circuit diagram of DC/DC bidirectional converter.

In the event of adding one bidirectional converter in this project, assuming the input as the DC bus and the output as the battery, it is analyzed as a buck converter. The bidirectional converter allows a current flow in both directions, from the input to the output and vice-versa. Therefore, it operates as a boost converter when the current flow is from the output (battery) to the input (DC bus).

In one of the most used battery management strategies, the two switches are driven alternately, which means that when the switch $S1$ is ON, the switch $S2$ is OFF and the converter operates in the buck mode.

The command signals of the two switches are presented in Figure 2.22.

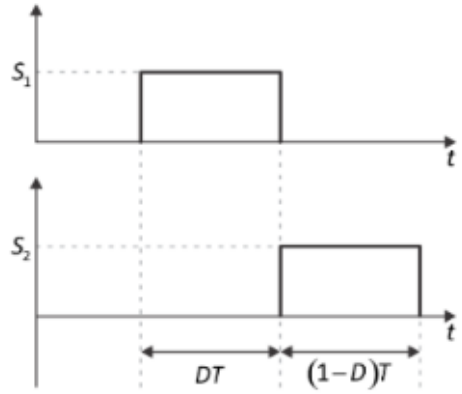

Figure 2.22: Ideal DC/DC bidirectional converter switches command signals [30].

In reality, the circuit in Figure 2.21 is not ideal, and has non-ideal components, namely the parasitic resistor of inductor L (R_L) and the equivalent resistors of the switches R_S, as shown in Figure 2.23, where it was assumed the same parasitic element (Rs) for positive and negative currents.

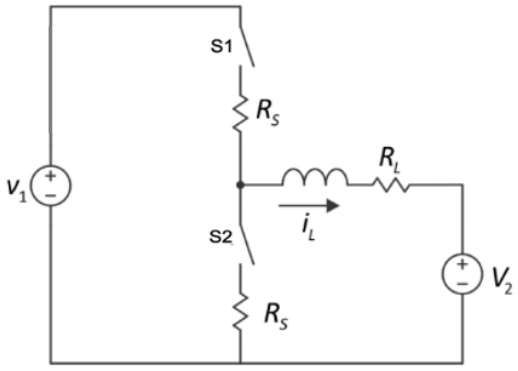

Figure 2.23: DC/DC bidirectional converter with non-ideal resistors. Adapted from [30].

For the average model in state-space analysis, it will be considered the equivalent circuit of the DC/DC bidirectional converter in steady-state. Assuming constant values for V_1 and V_2, the duty-cycle D defines the average value and direction of the current I_L.

With this command strategy, the conduction mode is always the continuous one. Then, the two stages of operation of the bidirectional converter for the time intervals $[0, DT]$ (Figure 2.24 (a)) and $[DT, T]$ (Figure 2.24 (b)), will be considered.

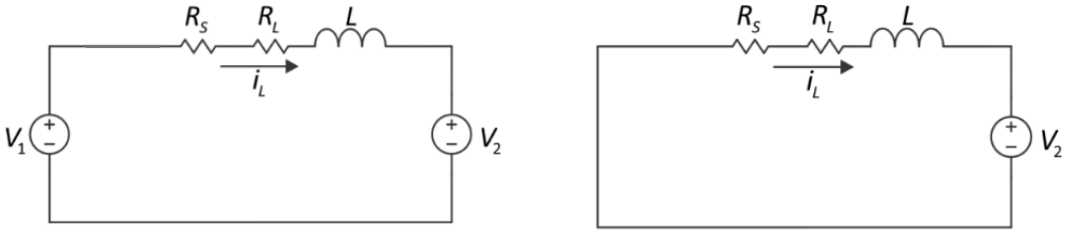

(a) Equivalent circuit with switch S_1 ON. (b) Equivalent circuit with switch S_2 ON

Figure 2.24: Operation states of non-ideal bidirectional DC/DC converter. Adapted from [30].

The operations stages, (a) and (b), are represented by the following equations, respectively.

$$\begin{aligned} L\frac{di_L}{dt} &= -(R_L + R_S)\cdot i_L - V_2 + V_1 \\ L\frac{di_L}{dt} &= -(R_L + R_S)\cdot i_L - V_2 \end{aligned} \tag{2.47}$$

Multiplying the first equation by D and the second one by (1-D), it is obtained:

$$\begin{aligned} D\cdot L\frac{di_L}{dt} &= -D(R_L + R_S)\cdot i_L - D\cdot V_2 + D\cdot V_1 \\ (1-D)\cdot L\frac{di_L}{dt} &= -(1-D)(R_L + R_S)\cdot i_L - (1-D)\cdot V_2 \end{aligned} \tag{2.48}$$

Applying the fact that at steady-state the average value of the voltage across the inductor is zero and adding both equations from Equation (2.48), it is obtained:

$$0 = -(R_S + R_L)i_L + D\cdot V_1 - V_2 \tag{2.49}$$

This equation is graphically shown in Figure 2.25.

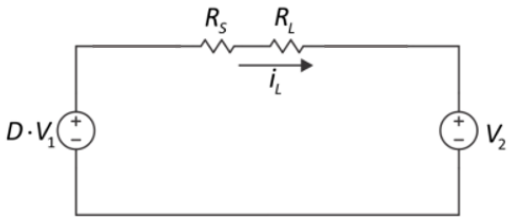

Figure 2.25: DC/DC bidirectional converter with non-ideal resistors in steady-state. Adapted from [30].

Concluding, the final equation relating input and out voltages in steady-state is:

$$\frac{V_2}{V_1} = D - \frac{(R_S + R_L) i_L}{V_1} \tag{2.50}$$

2.3.6 Synchronous Buck Converter

In a standard buck converter, there is no synchronization between the switch and the diode since the latter works in freewheeling. In a synchronous buck converter, the diode is replaced by another controlled semiconductor. Usually, the conduction and switching losses on a MOSFET, with a low on-resistance in the range of $m\Omega$, are significantly lower than of a rectification diode with a drop voltage approximately equal to 0.7 V. In a synchronous buck converter, on the OFF stage Equation (2.23), the low-side MOSFET will conduct, instead of its reverse diode. Therefore, when analyzing the total power losses on the OFF stage, the reverse diode forward voltage and reverse recovery time characteristics are not considered.

One of the advantages of using a synchronous converter is that the low-side MOSFET allows negative current through the inductance, eliminating the restriction of the CCM. Therefore, it is allowed a higher current ripple maintaining the linear regulation of the duty-cycle according to the output voltage.

However, it must be taken into account the need to control another semiconductor such that the two never conduct at the same time.

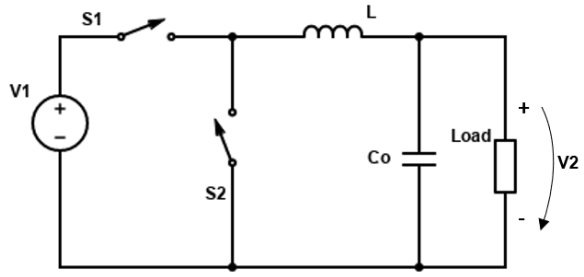

Figure 2.26: Circuit diagram of synchronous buck converter.

2.3.6.1 Dead Time in Switching

Due to the MOSFET's high switching frequency, it is essential to guarantee that they do not conduct simultaneously to prevent a short circuit that could damage several components. There are several alternatives for producing the dead time. This document introduces four alternatives: RC circuit with a Schmitt-trigger; XMC4500 controller and TMS320F28335 microcontrollers; and a simple shoot-through circuit.

RC circuit with a Schmitt-trigger

The circuit in Figure 2.27 shows the generation of the dead time using RC circuits and inverters with a Schmitt-trigger. In this project, the defined switching frequency for the DC/DC converter

is 50 kHz, which means a period equal to 20 μs. Since a reasonable dead time is 1%-2% of the period, a dead time between 200 ns and 400 ns will be appropriate.

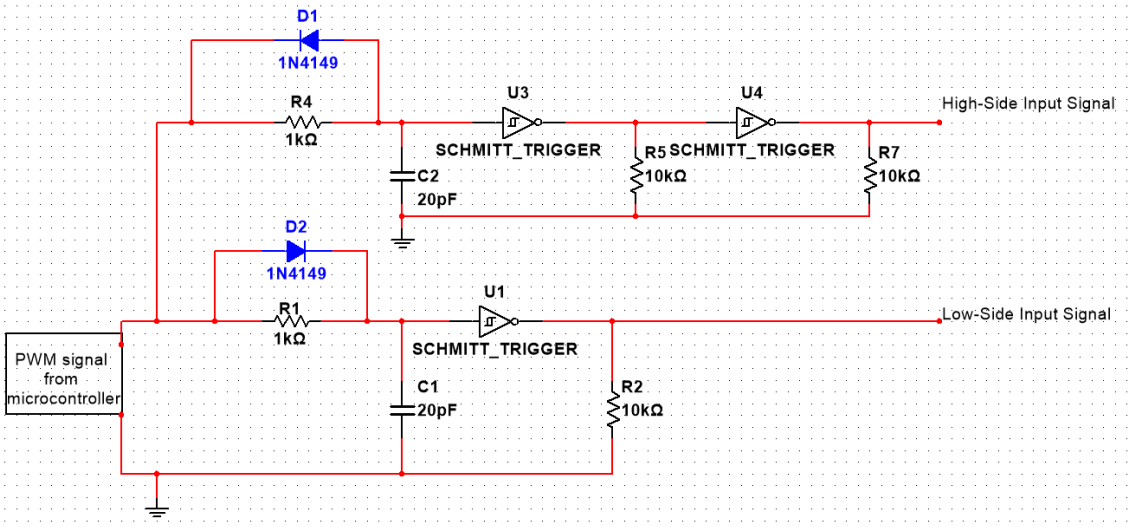

Figure 2.27: Shoot-through circuit with Schmitt-trigger.

This circuit creates two complementary command signals for the MOSFETs. The RC circuit at the input of each Schmitt-trigger avoids the overlap of the two signals. In Figure 2.27, the capacitor $C2$ will take more time to charge since the current passes through a resistor, unlike the $C1$ capacitor in which the current passes through a diode while charging. For the capacitors' discharge, it is the other way around. In conclusion, a higher RC circuit's time constant increases the lag between the two control signals.

Infineon XMC4500 and Texas Instruments TMS320F28335 microcontrollers

These two microcontrollers have dead time functions that directly implement a dead time between two PWM signals defined by the microcontroller. This alternative only requires a software implementation, decreasing the complexity of the complementary electronics circuits.

Simple Shoot-through circuit

The shoot-through circuit uses two ideal complementary signals, TG and BG.

The circuit presented in Figure 2.28 increases the rise time comparatively with the fall time. When the MOSFETs are switched ON, the current will flow through the gate resistor, $R_{gateL,H}$, which must be higher than R_a and R_b, assuming $R_a = R_b$, increasing the rise time. In the turn-off switching, the current will flow through the upper branch, with the diode in series with the lower resistor, and the fall time will be lower than the rise time.

2.3.7 Transistors Technologies

Semiconductors are materials whose electrical conductivity value is between conductors and insulators. In a conductor, the electrons can move from the valence band (electrons in the outermost

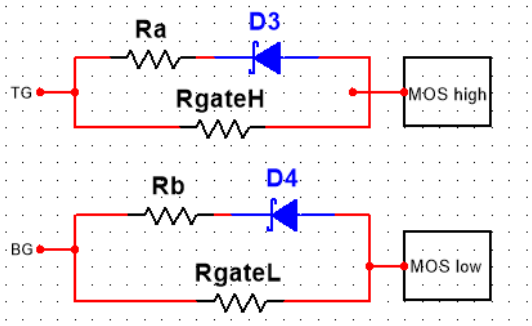

Figure 2.28: Shoot-through circuit.

layer or energy level of an atom) to the conduction band, which means there is no gap between the two bands. On the other hand, insulators have a large band between the valence and conduction band. In a semiconductor, there is a slight gap between the valence and conduction band, allowing the movement of the electrons when a specific voltage is applied.

Semiconductors in their pure form are called intrinsic semiconductors. Extrinsic semiconductors are pure semiconductors with added impurities through a process called doping. This process increases the conductivity of semiconductors. Depending on the doping material, extrinsic semiconductors can be divided into N-type or P-type semiconductors.

Characteristics of Silicon / SiC / GaN

Properties		Si	SiC	GaN
Bandgap	eV	1.1	3.3	3.4
Electron Mobility	cm^2/Vs	1350	700	1500
Breakdown Electrical Field	MV/cm	0.3	3.0	3.3
Figure of Merit	$\varepsilon\mu E_c^3$	1	440	1130

SiC /GaN Compared to Silicon:

High Breakdown Voltage Up to 10 Times Higher	High Heat Resistance Up to 1000℃
Compact Reduced Up to 1/1000	High Speed Up to 100 MHz

Figure 2.29: Characteristics comparison between Silicon, SiC and GaN [31].

Semiconductors are used in many electrical circuits and electronic components, such as diodes and transistors. In the early ages, Germanium (Ge) was the material used for semiconductors. Later, it was replaced by Silicon (Si), which has better characteristics, [31]. Nowadays, compound semiconductors such as Gallium Nitride (GaN) and Silicon Carbide (SiC) are the most used materials due to their excellent performance level, in comparison with silicon, with low power losses and higher efficiency in switching power applications, as illustrated in Figure 2.29.

Moreover, SiC and GaN are wide-bandgap semiconductors which means they have high electron mobility and bandgap energy. Therefore, they are suitable for high-voltage and high-power applications at high frequencies and temperatures. [32]

2.4 Charge Controllers

The charge controller can control the energy flux of the stand-alone PV system. One of its functions is to control the charge and discharge of the battery, protecting it against overcharging and deep discharge, [15].

The possible charge controllers of a stand-alone PV system are represented in three main groups: series regulators, which include a switch between the generator and the battery to switch off the charge; shunt regulators, which short-circuit the solar generator when the charge is complete; and the MPPT, which uses a particular electronic circuit enabling maximum power to be permanently extracted from the panel array, [15].

This project, as it is shown in Figure 1.1, uses an MPPT controller, which the next section will address.

2.4.1 MPPT Controller

Maximum Power Point Tracking (MPPT) maximizes the produced energy of a solar cell. A photovoltaic cell has nonlinear current-voltage (I-V) and power-voltage (P-V) characteristic curves that depend on factors such as irradiation and the cell temperature. In the latter, there is a point called the Maximum Power Point (MPP) in which its possible to extract the panel's maximum power allowing the maximum PV system efficiency.

An MPPT controller can be based on calculation models or search algorithms. There are four main methods: Hill-climbing techniques such as Perturb and Observe (P&O) and Incremental Conductance (IC); Fractional methods such as Fractional open-circuit voltage and Fractional short-circuit current; Artificial Neural Network (ANN) based; and Fuzzy logic (FL) based [33].

The MPPT controller is implemented in the DC/DC converter that connects the PV cells to the DC bus. It controls the PV panel operating point by changing the converter's duty-cycle, which is estimated according to the MPP. Each algorithm has its benefits and downsides regarding stability, convergency, and complexity.

The classic Perturb and Observe (P&O) method changes the operating point according to the MPP in the P-V curve imposed by the input conditions, irradiance and temperature. For this project, this algorithm is chosen because it has a simple and accessible implementation and is suitable and efficient for the system. A future improvement of the P&O method may be applied.

2.4.1.1 Perturb and Observe Method

In the classic P&O method, the PV panel voltage is periodically perturbed by a small increment or decrement, and the resulting change in the PV output power, ΔP, is measured. It requires periodic PV current and voltage measurements to calculate the PV power at each instant.

As illustrated in Figure 2.30, if ΔP is positive it means that the voltage perturbation moved the PV operating point closer to the MPP. Thus, further voltage perturbations in the same direction should be executed. If ΔP is negative, the algebraic sign of the voltage perturbation should be reversed, [34, 33]. For each situation, the voltage variation, ΔV, will define the duty-cycle's variation.

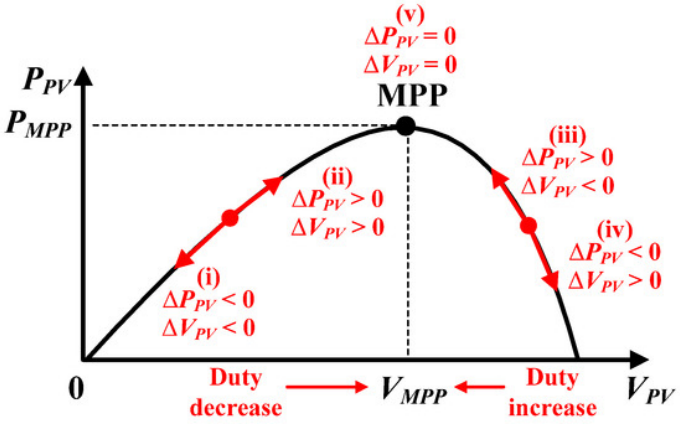

Figure 2.30: Representation of P&O method operation [35].

The flow chart in Figure 2.31 illustrates the decision process in this algorithm.

For example, assuming a DC/DC Buck converter, the goal is to increase or decrease the solar panel voltage by changing the duty-cycle's value. Knowing that in an ideal buck converter, the relation between the duty-cycle and the input and output voltages is equal to $D = \frac{V_2}{V_1}$, assuming a practically fixed value of V_2, in order to increase V_1 (the solar panel voltage), the duty-cycle must decrease and to decrease V_1 the duty-cycle must increase. The fixed duty-cycle step represented as *deltaD* in Figure 2.31 and the MPPT's algorithm frequency are very important since they influence the algorithm convergence, speed, and precision.

A common problem in the classic P&O method is that when the Maximum Power Point (MPP) is reached, the output power will oscillate around the maximum, changing the signal of the perturbation after each power measurement. This issue can be fixed by applying a stop condition when the power variation is smaller than a certain value ($\Delta P < \varepsilon$). In some cases, this problem can be partially fixed by the IC algorithm. However, it is prone to noise due to its differentiation operation.

Besides, the P&O performance can reduce under rapidly changing irradiances. There are different improvements available for the classic P&O method, such as the optimized and the three-point P&O algorithms. All three algorithms require the measurement of the PV array voltage (V_{PV}) and the PV array current (I_{PV}). The optimized technique uses an average of several samples of

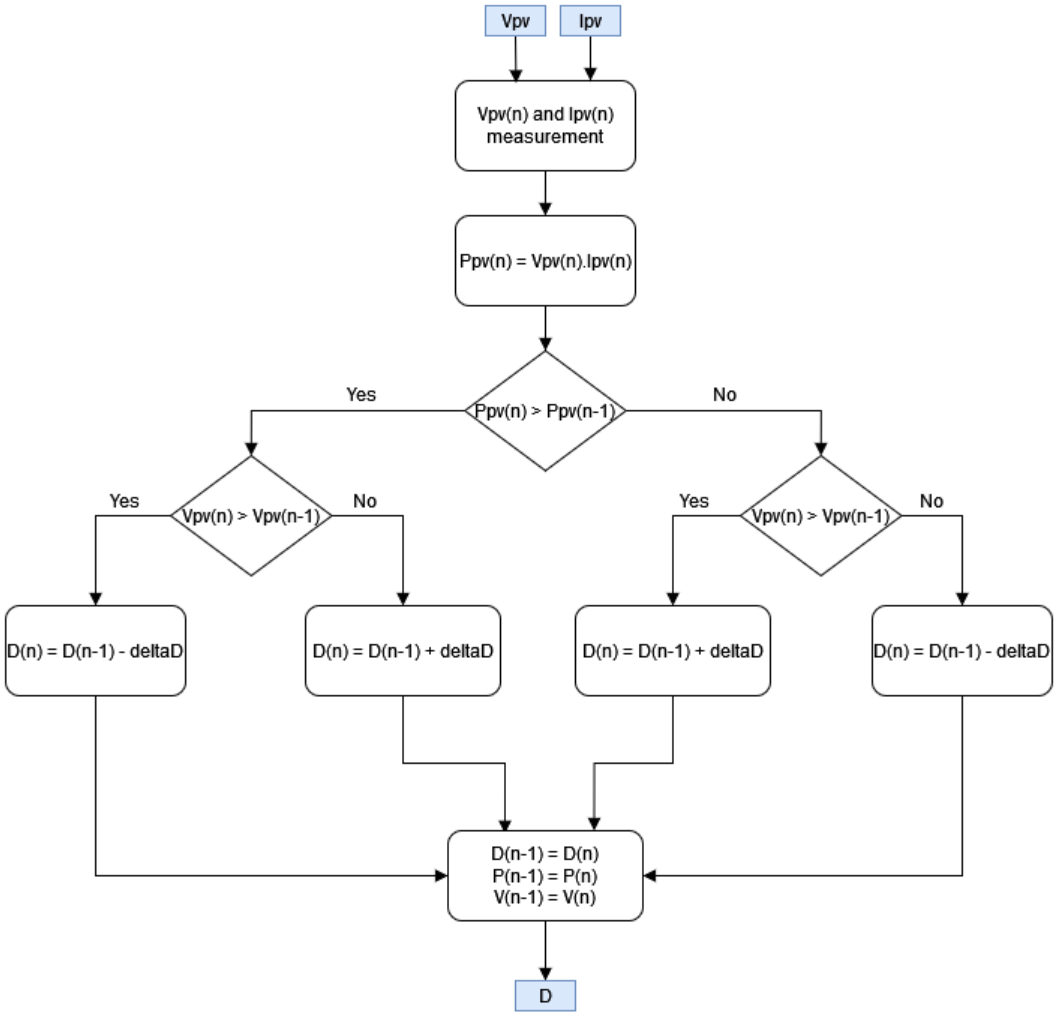

Figure 2.31: Flow chart of the classic P&O method.

the array power to dynamically adjust the magnitude of the perturbation of the operating point, increasing the complexity of the implementation. The three-point method compares the power of three points at the P-V curve to decide the perturbation direction. These three points are the current operating point (A), another point (B) perturbed from point A, and a third point (C) perturbed from point A in the opposite direction, [33].

2.5 Battery Management System

A Battery Management System (BMS) measures the battery parameters, such as total and individual cell voltage, current and temperature, playing an indispensable role in improving the battery performance, providing a longer lifespan and a safer operation of each individual cell. The BMS can interrupt the current when necessary and optimize the performance during charging and discharging, [36].

According to [36] the main functions of a BMS are :

1. Monitor the battery;
2. Protect the battery;
   (a) Prevent the voltage of any cell from exceeding a limit or dropping below a limit, by manipulating the charging current.
   (b) Prevent the temperature and discharging current from exceeding a limit.
3. Estimate the battery's state;
4. Report to users and/or external devices.

A BMS is essential when charging a Li-ion battery. LiPo cells must be connected to a BMS not only for charging but also to ensure that they are operating according to their safe operating area (SOA).

There are different BMS topologies, [37]:

- Centralized
- Modular
- Master-Slave
- Distributed

The centralized BMS is implemented on a single board from which a bundle of wires connects to the cells. It is the least expensive option for a low voltage battery, it is compact and in case of repair, it is easier to replace just a single board. [38]

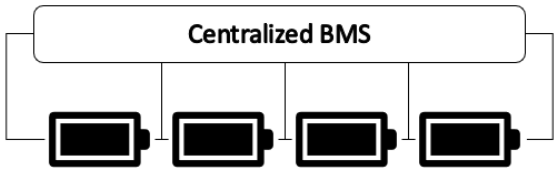

Figure 2.32: Centralized topology block diagram.

A modular BMS is similar to the centralized except that it is composed by multiple and identical boards that are connected and can communicate between themselves. Typically, one of the modules is the master and manages the entire pack and communicates with the rest of the systems, while the other modules act as remote measuring devices. It has the same advantages as the centralized BMS, plus the fact that it is easier to manage its wires since each module can be placed closer to the cells it handles, and its modularity simplifies the expansion to larger packs. However, the modular topology cost is slightly higher than the centralized one, and it requires extra wires as some points need to be connected to two modules, [37].

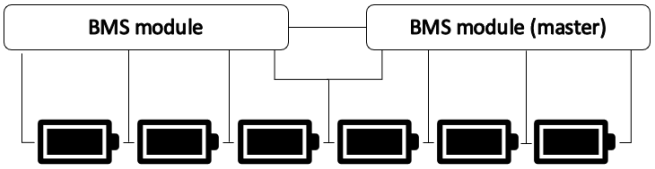

Figure 2.33: Modular topology block diagram.

The master-slave topology has a similar structure to the modular BMS since it is composed of multiple slave modules (measuring devices) that communicate with a master module. However, in this case, the master module is not connected directly to the cells, only to the slave modules. Therefore, this topology presents the same advantages and disadvantages as the modular one, except that the slave modules are optimized to measure cell voltages and the master handles the information, [37]. That allows the reduction of the overall system cost in comparison to the modular BMS.

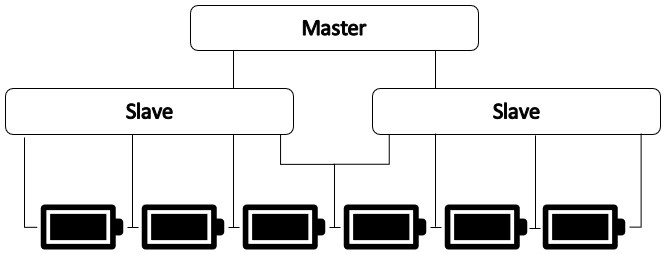

Figure 2.34: Master-slave topology block diagram.

In a distributed BMS, each cell has a cell board directly connected that is responsible for the voltage and temperature measurement and cell balancing. This configuration significantly reduces the use of wires since it just needs to connect the cell boards to the controller. [38] Despite the higher cost of this topology, its wiring is quite straightforward, and having one cell board to each cell allows high resolution voltage and temperature measurements. Besides, the expansion versatility is achieved by only changing the number of cell boards, [37].

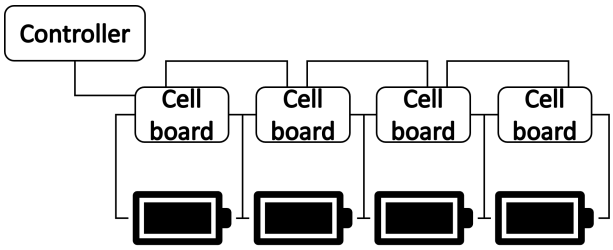

Figure 2.35: Distributed topology block diagram.

A final comparison of the four mentioned topologies is presented in Table 2.4. Regarding the costs, more stars are equivalent to a lower cost.

Table 2.4: Comparison of BMS Topologies. Adapted from [37]

	Centralized	Modular	Master-slave	Distributed
Measurement Quality	★★	★★	★★	★★★
Noise Immunity	★★★	★★★	★★★	★★
Versatility	★	★★	★★	★★★
Safety	★	★	★	★★★
Electronics cost	★★★	★★	★★	★
Assembly cost	★★	★★	★★	★★★
Maintenance cost	★★★	★★★	★★★	★★

★★★ = *Best*; ★★ = *Good*; ★ = *Normal*

2.6 Summary and Discussion

In this chapter, the characteristics and some alternatives were presented for the essential components of this project: the PV panel, the battery, the DC/DC converter and its additional protections, transistors technologies, the MPPT algorithm and the BMS.

Regarding the PV panels and the DC bus characteristics, it is chosen a buck converter. Another option could be the buck-boost or the Cuk converters. However, regarding the number of the converter's components and its associated cost, and since it is not required to invert the output voltage, allowing a common ground, the buck converter is suitable for this project.

The chosen MOSFETs for the converter are N-channel, ideal for high-frequency switching, named BSC093N15NS5. A simple shoot-through circuit to generate a dead time in switching and a Zener diode for gate protection are used.

The possible implementation of a bidirectional DC/DC converter to interface the battery and the DC bus would allow the control of the direction and amount of power flowing from/to the battery and the control of the DC bus voltage. However, since the battery voltage corresponds to the desired voltage for the DC bus and the allowed battery voltage variation is compatible with the components connected to the DC bus, in this project it is not required a converter that interfaces the battery and the DC bus. Therefore, the battery will fix the DC bus voltage and will be directly connected to the loads. In this way, control complexity and system losses are reduced.

The MPPT algorithm is the Perturb and Observe one and it does not require a current or voltage control. The BMS is a feature that should be used when connecting more than one Li-ion and LiPo cells.

Chapter 3

System Design and Simulation

According to a provided list of the components that will be connected to the DC bus, it is possible to estimate the total power consumption per day, as it can be observed in Appendix A.2. As illustrated in Figure 1.1, the main components connected to the DC bus are the BLDC motor, the Electronic Speed Control (ESC), the servo motors, the avionics part such as the GPS, the sensors, and there is also a payload related to the cameras and Raspberry Pi.

The mission profile for the UAV is shown in Figure 3.1.

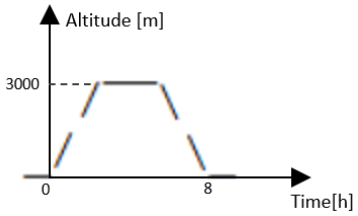

Figure 3.1: UAV mission profile.

After the take-off, the desired cruise altitude during the day is 3000 m, for about 8 h, and then the UAV lands.

The 3D modeling software CATIA V5 was used by the C2SR-Systec mechanical team to design the UAV mechanical structure. The total length of the UAV is 2.92 m, as in Figure 3.2, the tail's chord and span are 0.244 m and 0.691 m, respectively, as in Figure 3.3, the wing chord is 0.54 m, wingspan is 6.8 m, and the wing area is approximately 3.67 m^2, as shown Figure 3.4. The solar panels will be placed along the wingspan, the main panel in the middle, and later, one additional panel on each side of the main panel.

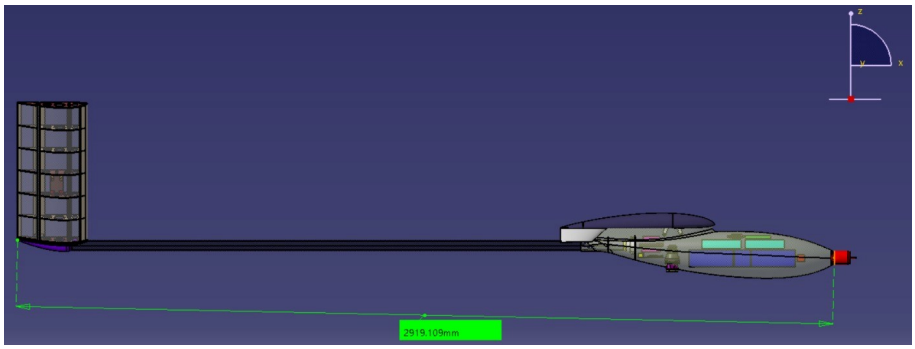

Figure 3.2: CAD representation of UAV, side view.

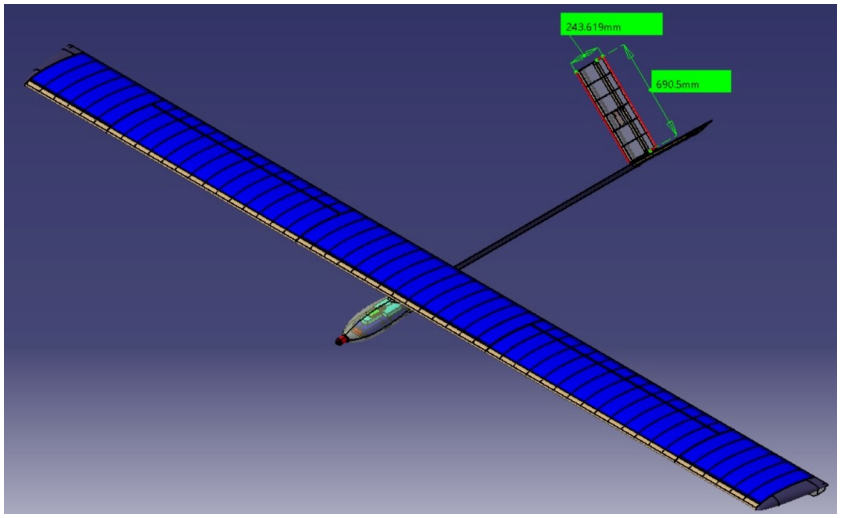

Figure 3.3: CAD representation of UAV, diagonal view.

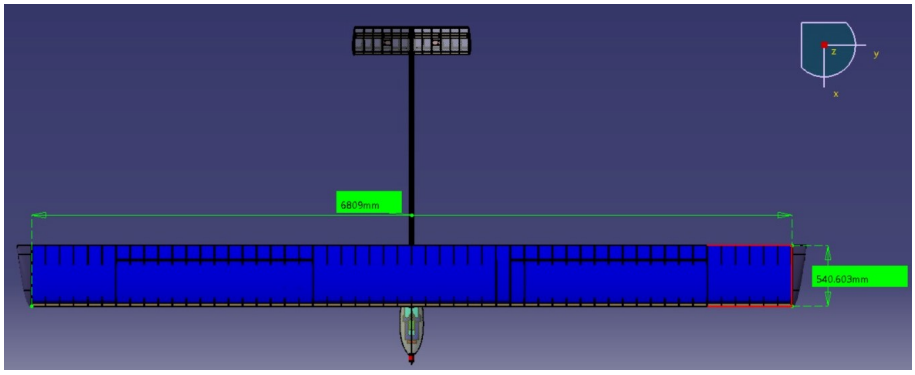

Figure 3.4: CAD representation of UAV, top view.

3.1 Energy Specifications and Components Sizing

According to the vehicle's physical characteristics, namely mass, and available surface, and mission profile, some of the preliminary requirements for the MPPT and the solar panel are presented

in Table 3.1.

Table 3.1: General characteristics of PV and MPPT.

Parameter	**Symbol**	**Value or range**	**Unit**
Nominal DC bus voltage/ battery voltage	V_{DC}	20-26	V
Continuous maximum current from the PV to the DC bus	$I_{pv_{max}}$	15	A
Maximum PV output voltage	$V_{pv_{max}}$	40	V
Minimum PV output voltage	$V_{pv_{min}}$	30	V

Projecting and sizing the solar aircraft requires a proper trade-off between the components' efficiency and their weight and size. In order to achieve an adaptable system, each component's operation range was considered.

In this project, it will only be considered the main PV panel, i.e., 56 solar cells in series (4 rows of 14 cells each) and a 6S battery with a nominal voltage of 22.2 V and a maximum voltage of 25.2 V. Since the minimum battery voltage is designed to be 20 V, a DC bus voltage variation of less than 20% is expected. This poses no special restrictions to the DC/DC converter or the MPPT operation.

This section addresses the buck converter's sizing and components selection, considering the efficiency and compatibility with the whole system. One of the most important parameters is the switching frequency which influences the values of both the inductor and the capacitors of the DC/DC converter and the ripple current flowing into/from the battery. Besides, the conduction losses of the converter also depend on the switching frequency, being directly proportional. The chosen switching frequency (f_s) for the DC/DC converter is 50 kHz.

As aforementioned, the unidirectional buck converter links the solar panel and the DC bus. Therefore, the input voltage range depends on the solar panel, and the maximum nominal voltage will be 32.6 V, considering the V_{mpp} value in Table 2.2. In the future, using the three solar panels, the main one and the two additional panels, which means 140 solar cells in series, the maximum nominal voltage will be 81.5 V. Assuming that the cells are always connected in series, the maximum nominal current of the solar panel is 5.93 A. In conclusion, assuming only the main solar panel, the maximum nominal power is 193.32 W ($P_{max} = 32.6\ V\ \times 5.93\ A$).

3.1.1 Inductor

One of the most important conditions to define the inductor's value is its maximum current.

The basic formula to calculate the inductor current is Equation (3.1), where it is considered that the inductor voltage assumes only constant values.

$$v_L = L\frac{di_L}{dt} = L\frac{\Delta i_L}{\Delta t} \tag{3.1}$$

Assuming the voltage in the inductor during the ON interval, mentioned in Equation (2.33), and replacing v_L from Equation (3.1), it is possible to conclude that the inductance value is designed according to Equation (3.3).

Assuming a 90% converter's efficiency, a realistic efficiency for a buck converter, ($P_{out} = 0.9P_{in}$) and a nominal DC bus voltage, V_2, equal to 22.2 V:

$$P_{out} = V_2 \times I_o \Leftrightarrow I_o = \frac{0.9P_{in}}{V_2} = 7.84\ A \tag{3.2}$$

Knowing that the average inductor current is equal to the output current, and considering an inductor ripple of 30% of the output current, a common estimation for this value, the inductor value can be calculated with Equation (3.3).

$$L = \frac{(V_1 - V_2)V_2}{\Delta i_L f_s V_1} \tag{3.3}$$

For the given conditions it results in $L = 60.2\ \mu H$. Concluding, there are two conditions that must be considered to choose the inductor:

$$\begin{cases} L > 60.2\ \mu H \\ I_{L,max} = I_{L,avg} + \frac{\Delta i_L}{2} = I_o + 15\% I_o = 9\ A \end{cases} \tag{3.4}$$

The selected inductor is from Würth Elektronik with an inductance equal to 68 μH and 17 A maximum DC current.

3.1.2 Output Capacitor

The output capacitor is essential to stabilize the DC bus voltage. The inductor current has a DC and AC component, $I_{L,avg}$ and $i_{L,ac}$ respectively.. As mentioned in Equation (2.24):

$$i_C = i_L - I_o \tag{3.5}$$

Knowing the capacitor impedance $X_C = \frac{1}{2\pi f \cdot C}$, it can be assumed that for high frequencies, the capacitor will behave as a short circuit, and its only associated current will be the inductor AC current. That is a valid approximation to manage calculations, so one can consider that $I_{L,avg} = I_o$ and $i_{L,ac} \approx i_C$.

Assuming that the energy balance of the capacitor is null during one period, i.e., the capacitor charges and discharges the same amount, through graphical and mathematical manipulation, it is possible to obtain the following equation of the capacitor charge variation ΔQ:

$$\Delta Q = \frac{\Delta i_L \cdot T}{8} \tag{3.6}$$

Knowing that $\Delta Q = C \cdot \Delta v_C$, it is obtained:

$$C = \frac{\Delta i_L}{8 f_s \Delta V_2}. \tag{3.7}$$

Selecting an output voltage ripple of 1% of V_2 it results in:

$$C_{o,min} = 26.5\ \mu F \tag{3.8}$$

The equivalent series resistance (ESR) of the ouput capacitor adds some more ripple, according to Equation (3.9), [39]:

$$\Delta V_{out,ESR} = ESR \times \Delta i_L \tag{3.9}$$

However, this addition will only decrease the output capacitor value. An output electrolytic capacitor with 100 μF and a nominal voltage of 50 V is selected. Besides this capacitor, a lower ceramic capacitor with 1 μF is placed in parallel to filter possible high-frequency noise.

3.1.3 Input Capacitors

3.1.3.1 Bulk Capacitor

For this capacitor, two different design equations were considered, Equation (3.10) and Equation (3.11), the latter from [40].

In Equation (3.11), the load-transient step current, I_{step}, is considered to be 50% of the output current (I_o), the D_{max} is 0.9, the converter output-current rise time during a transient is calculated from Equation (3.12), the $V_{in,tran}$ is the allowed input voltage transient and equal to 0.5 V, and f_{BW} is equal to the MPPT algorithm frequency, which in this case is considered to be 1 kHz.

$$i_C = C_{in}\frac{dV_{in}}{dt} \Leftrightarrow C_{in} = \frac{i_C \Delta t}{\Delta V_{in}} \tag{3.10}$$

$$C_{in,min} = \frac{0.5 I_{step} D_{max} T_R}{V_{in,tran}} \tag{3.11}$$

$$T_R = \frac{1}{4 f_{BW}} \tag{3.12}$$

For Equation (3.10), assuming half of the switching time $\Delta t = \frac{T}{2}$, $\Delta V_{in} = 2\% V_1$, considering a minimum value of V_{in} equal to 30 V and a maximum value of $i_C = I_{in}$ equal to 7 A.

$$C_{in} = \frac{i_C \Delta t}{\Delta V_{in}} = 117\ \mu F \tag{3.13}$$

For Equation (3.11), considering the Equation (3.12) and the aforementioned values:

$$C_{in} = 882\ \mu F \tag{3.14}$$

Therefore, considering both valid equations, an intermediate value for the input bulk capacitor was chosen, a capacitor with 560 μF and 100 V.

3.1.3.2 Ceramic Capacitor

According to [40], adding ceramic capacitors in parallel is recommended to lower the input capacitor ESL. Since the ESR of ceramic capacitors is very low, it can be ignored. For the input ceramic capacitor, the following equation uses the duty cycle value that maximizes the equation, which is 0.5, and $\Delta V_{in,pp}$ is considered equal to 2% of the maximum nominal voltage of the PV panel, V_1.

$$C_{in,min} = \frac{D(1-D)I_o}{\Delta V_{in,pp} f_s} = 60.1 \ \mu F \tag{3.15}$$

It was selected an input ceramic capacitor with 68 μF and 100 V.

3.1.4 MOSFET and Gate Driver

The MOSFETs are essential since their accurate control affects the converter's correct operation. As aforementioned in Section 2.6, the chosen MOSFETs are N-type.

The maximum current and voltage applied to the MOSFETs can be considered the same and equal to:

$$\begin{cases} V_{max} = V_{1,max} = 40 \ V \\ I_{max} = I_{L,max} = 9 \ A \end{cases} \tag{3.16}$$

The chosen MOSFETs are BSC093N15NS5 with the following performance parameters:

Table 3.2: N-MOS BSC093N15NS5 Parameters.

Parameter	$V_{DS}[V]$	$R_{DS,on}[m\Omega]$	I_D [A]	Q_{rr} [nC]	rise time $(t_r)[ns]$	fall time (t_f) [ns]
Value	150	9.3	87	58	4.3	3.8

The rise and fall times are directly proportional to the MOSFETs switching losses, and the internal on-resistance is proportional to the conduction losses. Therefore, these values should be as low as possible to reduce the MOSFETs losses. As one can observe in Table 3.2, all the aforementioned values are very low.

A proper gate driver is necessary to guarantee a safe and correct switching of the semiconductors, and the LTC4444 was selected. The LTC4444 is a high-frequency gate driver able to drive two N-channel MOSFETs in a synchronous DC/DC converter. It contains undervoltage lockout circuits and adaptive shoot-through protection that prevents both MOSFETs from conducting simultaneously. Besides, it has a pin that allows bootstrapping, creating a high-side bootstrapped supply, as illustrated in Figure 3.5.

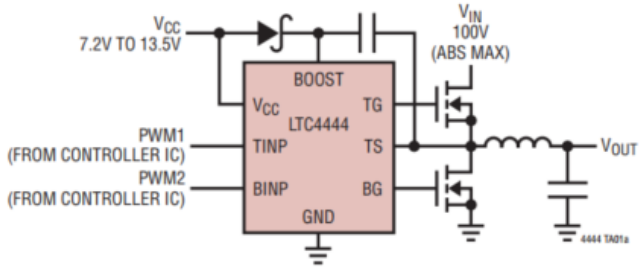

Figure 3.5: LTC4444 buck converter typical application [41].

3.1.4.1 MOSFET Protections

Shoot-through circuit

As aforementioned in Chapter 2, in order to create additional MOSFET protection, it was implemented a simple shoot-through circuit to generate a dead time, as described in Section 2.3.6.1.

In order to estimate the value of the gate resistors, Equation (3.17) and Equation (3.18) were considered:

$$I_g = \frac{V_{DD} C_{iss}}{t_{on}} \tag{3.17}$$

$$R_g = \frac{V_{DD} - V_{miller}}{I_g} \tag{3.18}$$

V_{DD} is the gate driver supply voltage, which is defined as 12 V; C_{iss} is the input capacitance of the MOSFET, the BSC093N15NS5, and its maximum value is 3.2 nF; t_{on} is the time we define to charge the input capacitance and turn on the MOSFET. It will be considered equal to 40 ns. V_{miller} is the gate threshold voltage typically equal to 3.8 V in the chosen MOSFET.

With these values, the estimated gate current I_g will be 0.96 A, and consequently, the gate resistor will be approximately 8.5 Ω. However, to decrease the gate current and thus lower the noise, i.e., the switches' $\frac{dv}{dt}$ and $\frac{di}{dt}$ gradients, a safety factor was multiplied by the gate resistor calculated value. Therefore, the selected value for $R_{gateL,H}$ is 22 Ω. R_a and R_b are defined with 5.6 Ω.

Gate Protection

A voltage transient may exceed the maximum V_{GS} at turn-on. A Zener diode can be placed as close as possible to the device to prevent this situation, as shown in Figure 3.6. Its reverse voltage must be lower than the maximum V_{GS} value to protect the MOSFETs against excessive gate-source voltages and higher than the PWM signal voltage.

3.2 Simulations

Each part of the electrical system has to be properly defined to have a behavior as close as possible to the real system, simulating its electrical model. The power system will be simulated

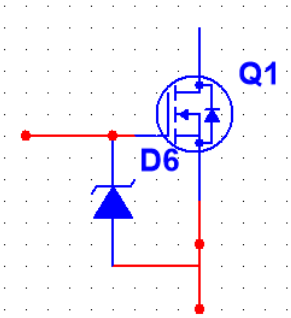

Figure 3.6: Gate protection with Zener diode.

using the converter's switching model, incorporating the power switches' details and capability of demonstrating the fast converter dynamics and the system losses. The simulation software is very important to guarantee that the results are reliable and represent the real system behavior. However, as simulation software not often represents exactly the same results as a real system, when working with the real components, some adjustments may be required.

Firstly, it was simulated a Simulink block that implements an array of photovoltaic modules. The array is built of strings of modules connected in parallel, each string consisting of modules connected in series. Later, the solar panel, the synchronous buck converter, and the battery were simulated using the switching model of the converter.

3.2.1 Static Characteristics

For an initial simulation, it was selected a PV array with one parallel string and 14 series-connected modules per string, considering that each module has only one cell (N_{cell}=1), i.e., 14 cells in series. Thus, the block defined values are specified in Table 3.3, assuming the C60 solar cells and their characteristics in Table 2.2.

The inputs of the PV array block are the irradiance in W/m^2 and the cell temperature in ºC. The outputs are a five-element vector of measurements, namely the PV array voltage (V) the PV array current (A), the diode current (A), the irradiance W/m^2 and the temperature (ºC).

Table 3.3: Defined module data in the simulated PV array.

Parameter	Symbol	Value	Unit
Open circuit voltage	V_{oc}	0.687	V
Short circuit current	I_{sc}	6.28	A
Voltage at maximum power point	V_{mpp}	0.582	V
Current at maximum power point	I_{mpp}	5.93	A
Temperature coefficient of V_{oc}		-0.36099	% / ^{o}C
Temperature coefficient of I_{sc}		0.102	% / ^{o}C

Considering a row composed of 14 solar cells, I_{sc} will be equal to 6.28 A, V_{oc} will be 9.618 V, and the maximum nominal voltage will be 8.148 V. Thus, multiplying the module's maximum voltage and current ($I_{mpp} = 5.93$ A), the maximum power output will be $5.93 \times 8.148 = 48.32$ W. These values can be verified in Figure 3.7.

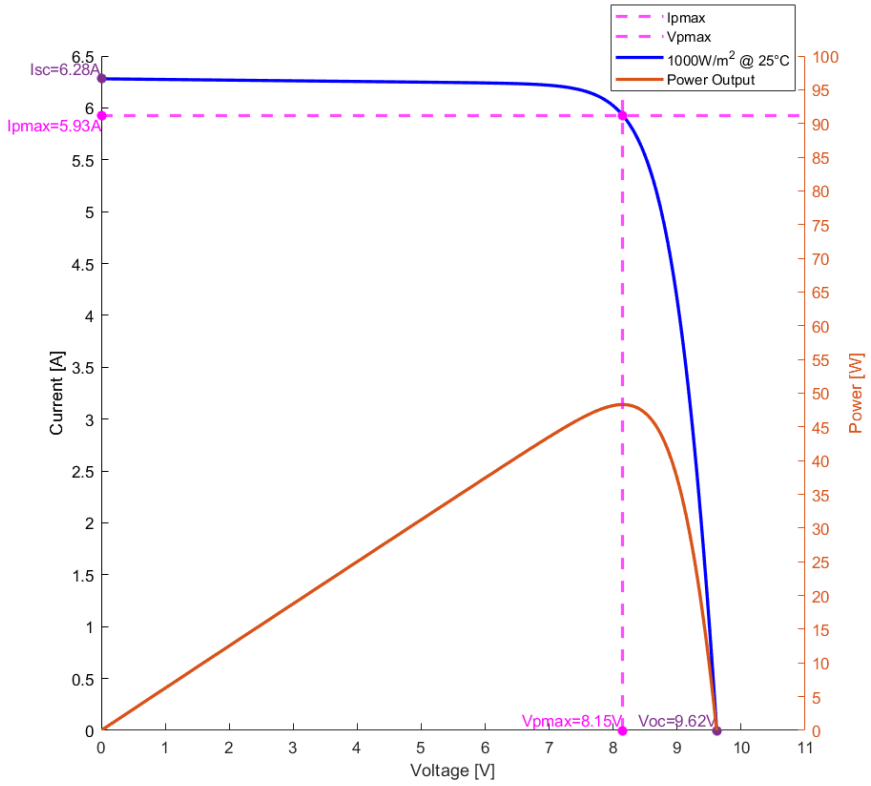

Figure 3.7: Simulated I-V and P-V curves in STC.

In order to verify the effect of the temperature and irradiance of the solar cell on the I-V and P-V characteristics, three different input conditions were simulated, and the result is presented in Figure 3.8.

Observing the I-V curves, one can conclude that maintaining the irradiance, the temperature decrease causes a decrease of the short circuit current and an increase in the open circuit voltage. Maintaining the temperature and decreasing the irradiance, both short circuit current and the open circuit voltage decrease, noticing that the short circuit current has a more significant reduction.

In Figure 3.7, comparing the blue and orange P-V curves it is possible to conclude that with the same irradiance, decreasing the temperature there is a higher maximum power point (MPP). Comparing the orange and yellow P-V curves, maintaining the temperature and decreasing the irradiance, the voltage at the maximum power point is almost the same, but the current decreases. Thus, the MPP will be lower.

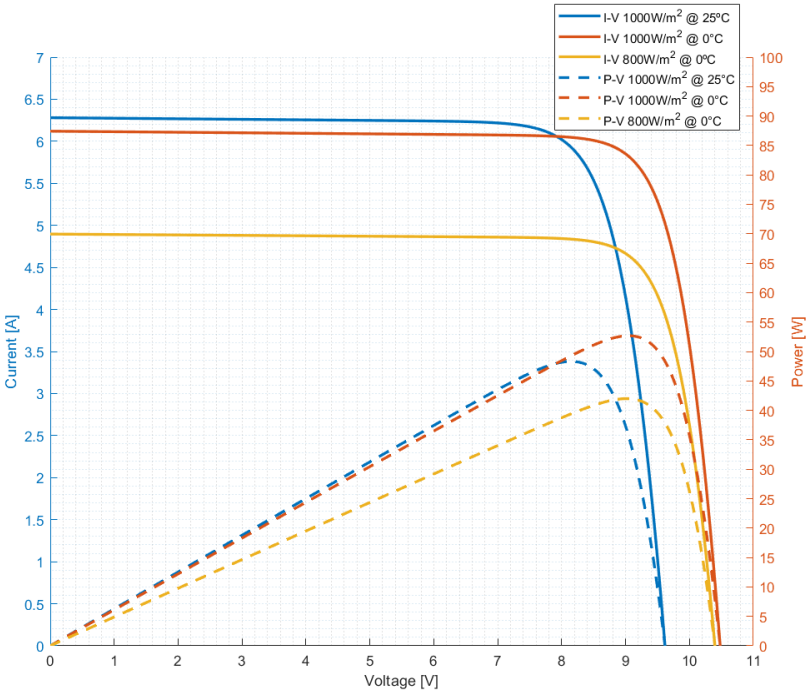

Figure 3.8: Simulated I-V curves for different input conditions.

3.2.2 Dynamic Tests

In order to evaluate different operation scenarios, the power system diagram used in the following simulations is presented in Figure 3.9, where realistic models were used either for the passive components and the active switches.

In the PV system, the panel is composed of 56 cells connected in series, giving V_{mpp}=32.6 V and a maximum power of 193 W.

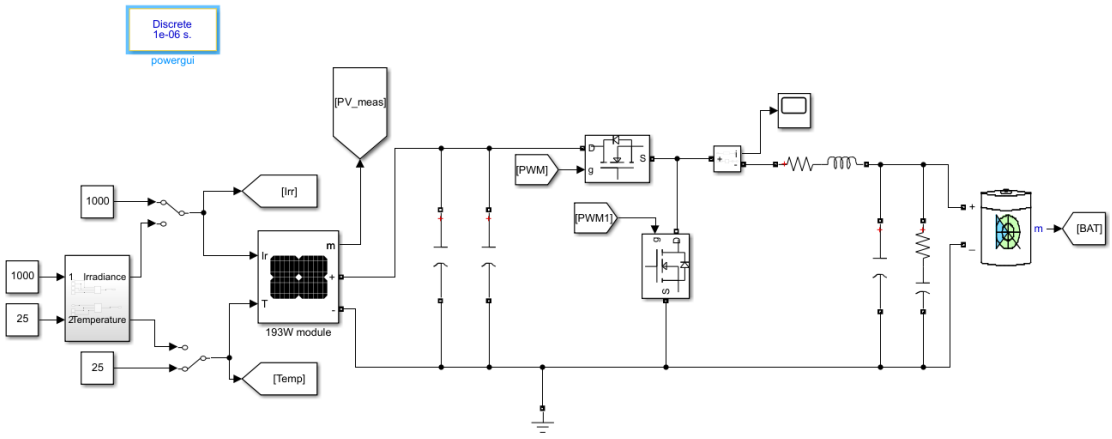

Figure 3.9: Synchronous buck converter switching model.

In order to evaluate some steady-state and transient conditions, the diagram in Figure 3.10 was

implemented for connecting and disconnecting loads. The control subsystem, including the MPPT and its stop condition is illustrated in Figure 3.11.

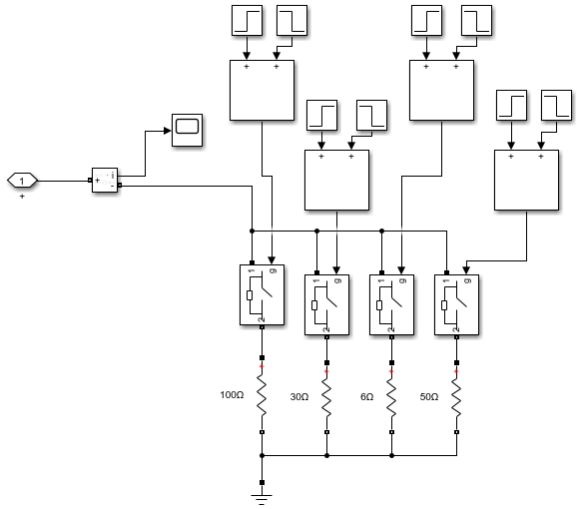

Figure 3.10: Load variation subsystem.

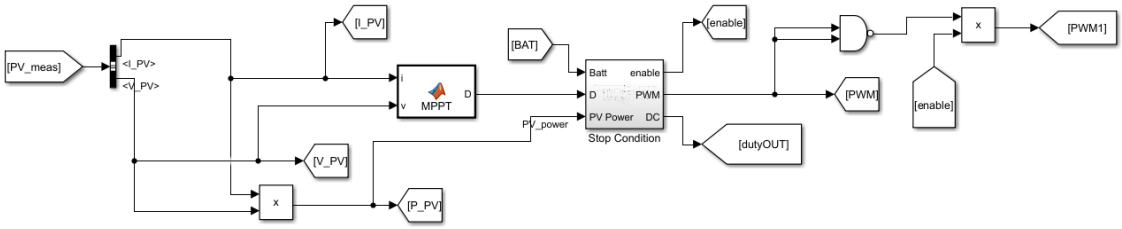

Figure 3.11: Converter control with MPPT algorithm.

It was used a 68 μH inductor with a parasitic resistance equal to 0.4 Ω, two parallel capacitors were placed at the input, one with 560 μF and a smaller one with 68 μF, two parallel output capacitors, one with 100 μF with an ESR equal to 0.025 Ω and a smaller one with 1 μF. The battery model used was the one shown in Figure 3.9, in which it was possible to define its type (Li-ion), the nominal voltage (22.2 V), capacity (3.35 A.h), and the initial state of charge in percentage.

It is essential to define a good value for the deltaD in the MPPT algorithm, i.e., the value that will increment or decrease the duty cycle at each time step in the defined MPPT frequency. The frequency of the MPPT algorithm is equal to 1 kHz, which means that the PV panel's current, voltage and power measurements will be acquired at each 1 ms, which is sufficient since the irradiance and temperature change at a very slow rate.

The MPPT algorithm generates the high-side MOSFET control signal, and a NAND logic port is used to create a complementary PWM signal to control the low-side MOSFET. The stop condition block defines an enable signal that will disable the low-side MOSFET if necessary for test conditions.

Smaller values for deltaD, in the order of 10^{-6}, were tested first in order to its final value. However, they were not suitable since they caused a very slow response. Then, higher values in the order of 10^{-4} and 10^{-3} were tested. Finally, it was fixed a deltaD equal to 2×10^{-3} that was used in the simulations presented below. It is important to mention that this value and the MPPT frequency might need to be adjusted when testing the real system.

Besides, the calculated power value used for the MPPT algorithm can have some noise in the real system, especially from the PV panel current measurement. In order to reduce that effect, it was defined that the duty cycle variation will only happen when $\Delta P_{pv} > 0.20\ W$.

3.2.3 Algorithm Test

In order to test the implemented MPPT algorithm, the system was simulated with variable step irradiances and temperatures at the PV input, as presented in Table 3.4. In this scenario, no passive load was considered, only the battery was connected. In reality, the solar irradiance and the ambient temperature will not change instantly. However, if the system can adapt to the simulated conditions, it should also have a good response to a real scenario.

Table 3.4: PV panel input values for testing MPPT algorithm.

Time interval [s]	[0; 0.5]	[0.5; 1]	[1; 1.5]	[1.5; 2]	[2; 2.5]	[2.5; 3]
MPP [W]	193.3	212.9	95.0	193.3	181.6	212.3
Irradiance [W/m^2]	1000	1100	500	1000	1000	1000
Temperature [ºC]	25	25	25	25	40	0

Figure 3.12 shows the evolution of the independent variables irradiance and temperature, the maximum power available in such conditions, and the converted power.

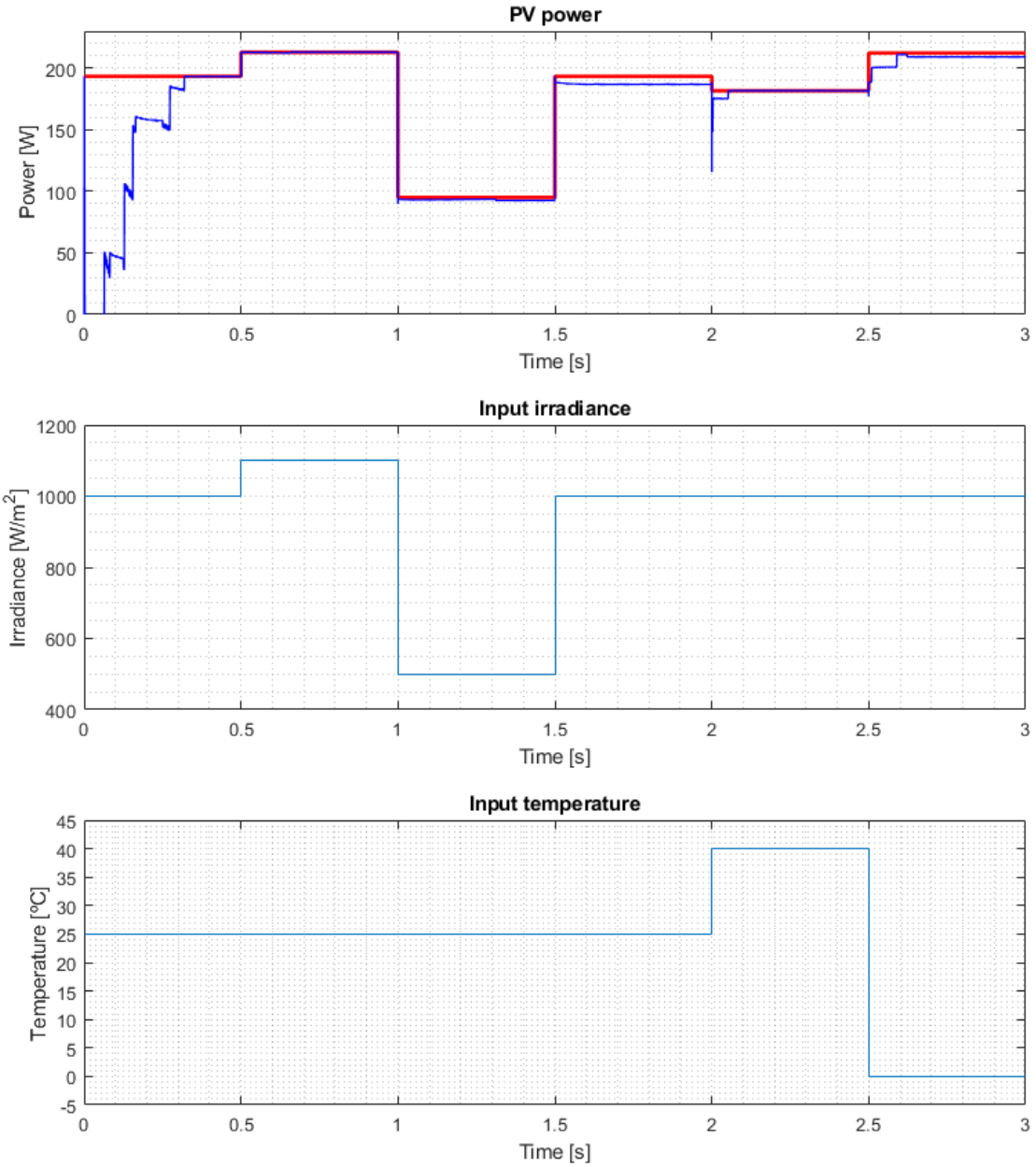

Figure 3.12: PV power variation with different irradiance and temperature levels.

As it can be observed in Figure 3.12, the system takes about 0.3 s to reach the first MPP, and then the PV power follows the maximum power value for each input conditions, represented by the red line. When the irradiance increased from 1000 W/m^2 to 1100 W/m^2, the MPP was perfectly followed. When it varies from 500 W/m^2 to 1000 W/m^2, the PV power is slightly below its MPP, probably due to the high amplitude step in irradiance. It can also be observed that the temperature changes in the last three intervals create some peaks and power variations, but the MPPT algorithm still converges to the desired power value.

For the same input conditions (irradiance and temperature), Figure 3.13 presents the inductor current, the duty-cycle of the high-side PWM signal, and the PV panel voltage.

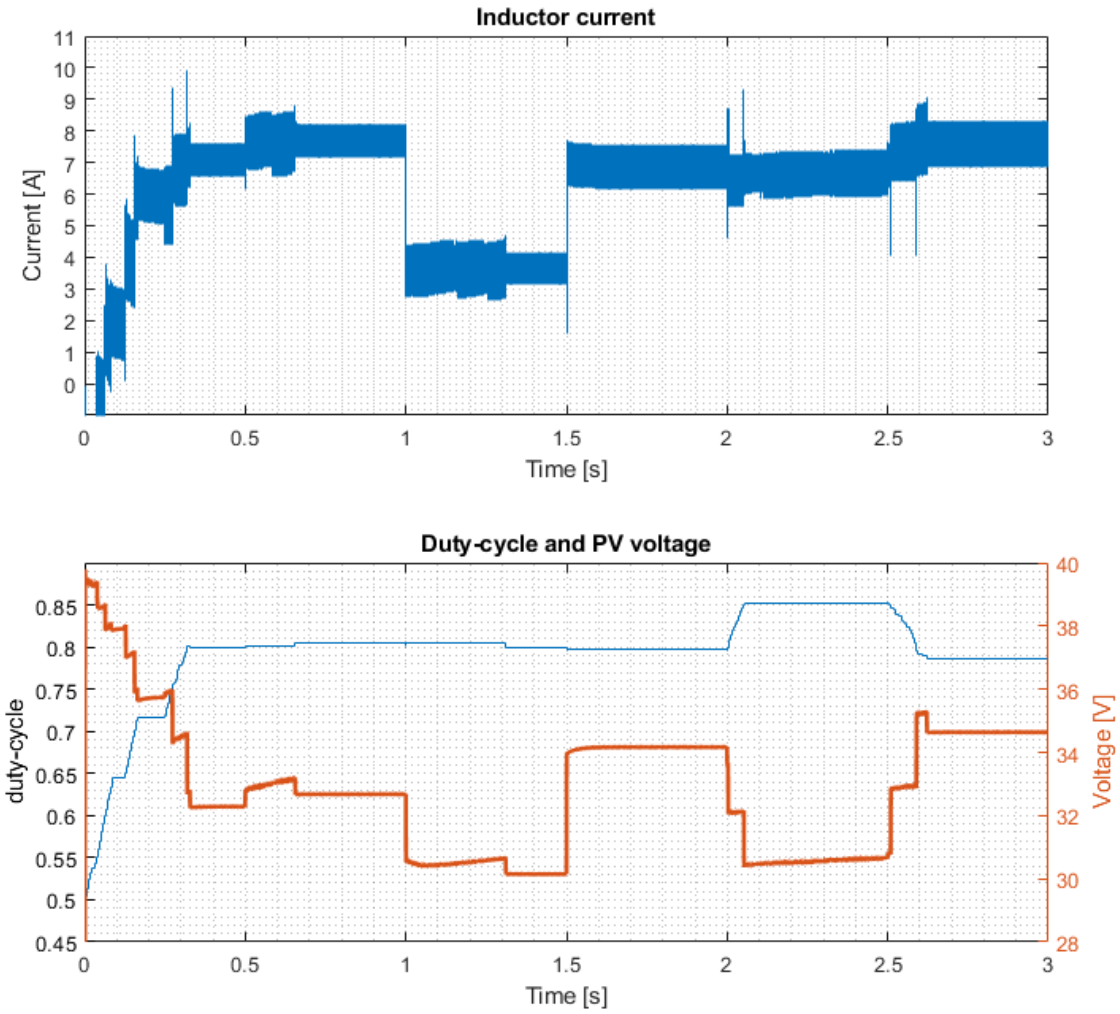

Figure 3.13: Inductor current, duty-cycle (blue) and PV voltage (orange) according to different irradiance and temperature levels.

In Figure 3.13 it can be seen that at the first interval at STC (irradiance = 1000 W/m^2 and temperature = 25°C), the inductor current has an average value of approximately 7 A, as expected. As aforementioned, the maximum current in the inductor was sized to 9 A. There are sudden peaks that occur due to more abrupt changes in the duty cycle and that exceed that current value. However, it was selected an inductor with a higher DC current (17 A). Therefore, these peaks will not be problematic.

Moreover, one can conclude that after reaching steady-state, the PV voltage is maintained approximately between 30 V and 35 V. As expected, the irradiance and temperature variations have high influence on the PV voltage.

A steady-state condition at STC, with an inductor average current of 7 A is shown in Figure 3.14.

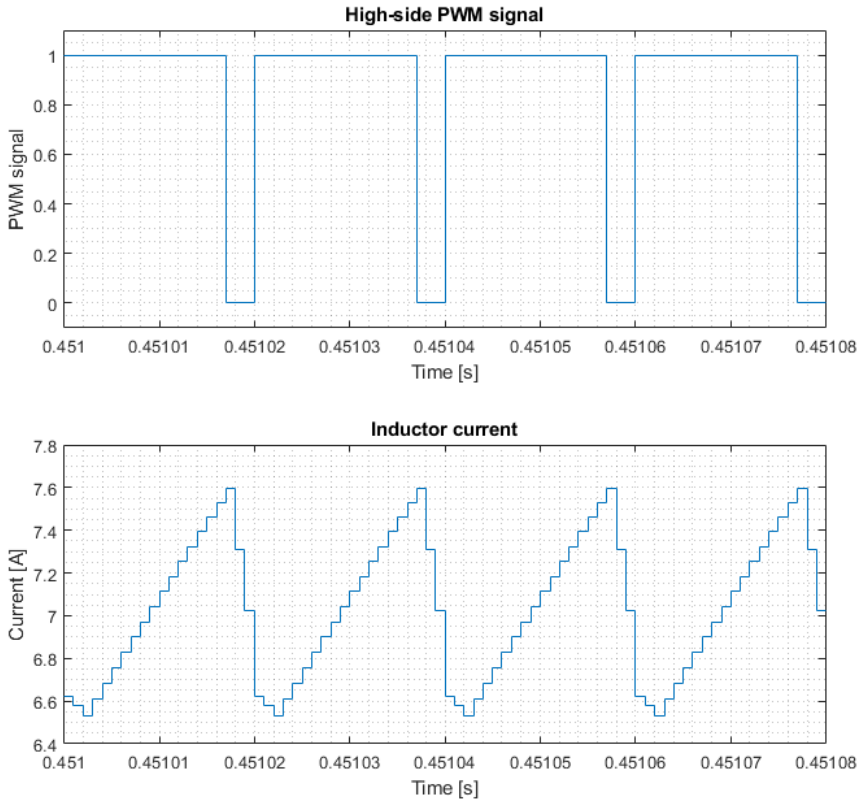

Figure 3.14: Inductor current at steady state with 1000 W/m^2 and 25°C.

The inductor current clearly shows the time step used for simulating the system (1 μs). A smaller one was used, but the results did not change significantly. Thus, this one was used in all simulations with the switching model for the converter without loss of accuracy. In steady-state, the ripple is approximately 1 A, which is within the estimated ripple of 30% in Section 3.1.1 ($30\%I_o = 2.35\ A$).

Still using the same conditions, Figure 3.15 demonstrates the battery voltage, battery current, and the state of charge (SoC) evolution.

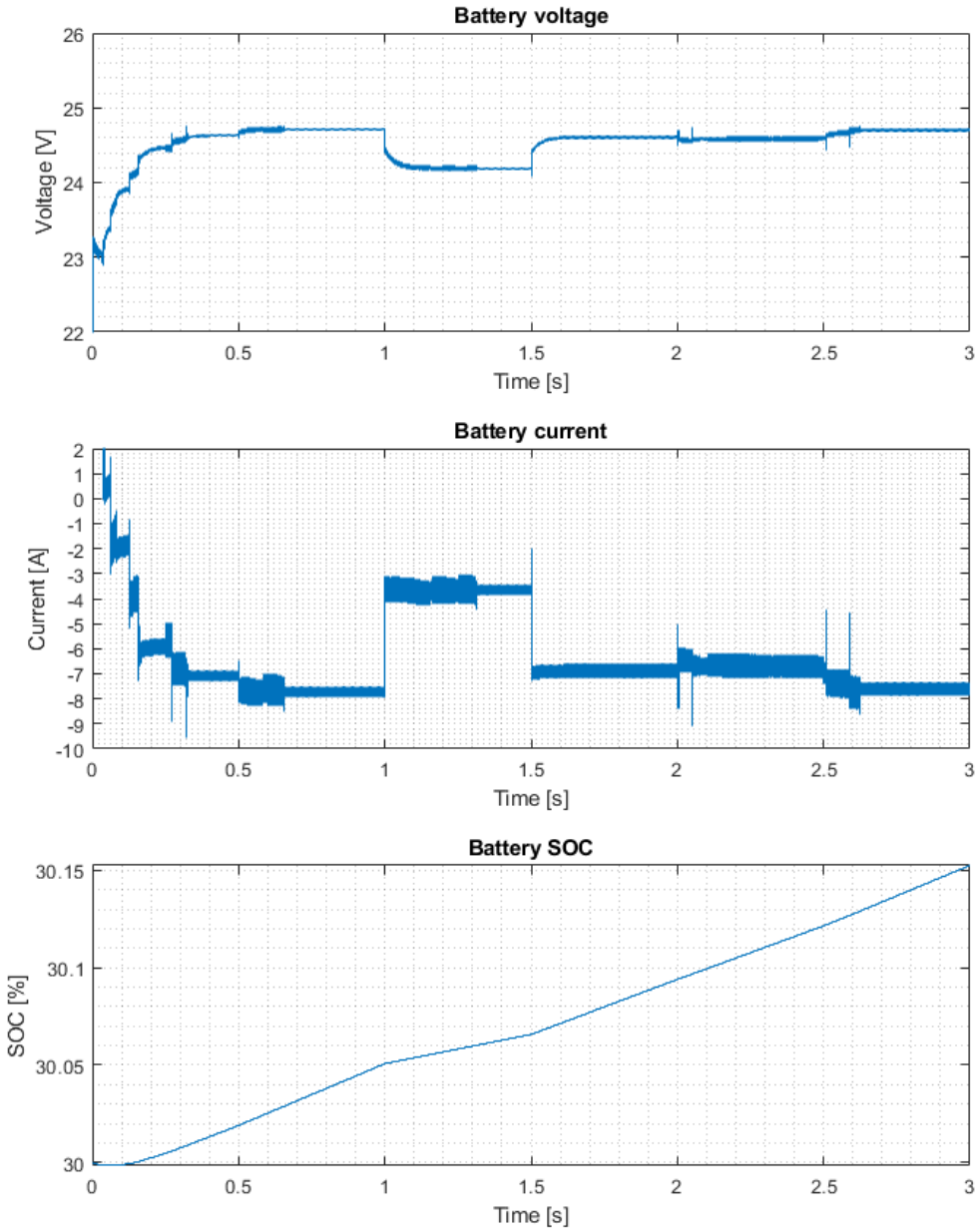

Figure 3.15: Battery measurements according to different irradiance and temperature levels.

In Figure 3.15, one can observe that the battery was only slightly charged due to the short time interval, with a current symmetrical to that of the inductor, with a smaller ripple since there was no passive load. The DC bus/ battery voltage was maintained between 24 V and 25 V.

At this point, it should be kept in mind that a realistic dynamic battery model was used in the simulation, as shown in Figure 3.15.

3.2.4 Variable Load Test

In this simulation, the irradiance and temperature were maintained constant and equal to 1000W/m^2 and 25°C, respectively, and a variable load was added in parallel with the battery. Four different loads were defined and changed at each 0.5 s of simulation, with values equal to 100 Ω, 30 Ω, 6 Ω and 50 Ω, as illustrated in Figure 3.10, corresponding to currents of 0.24 A, 0.8 A, 4 A and 0.48 A, respectively, under 24 V.

Figure 3.16 shows the evolution of the maximum power available in STC and the converted power, the inductor current and the duty-cycle of the high-side PWM signal, and the PV panel voltage.

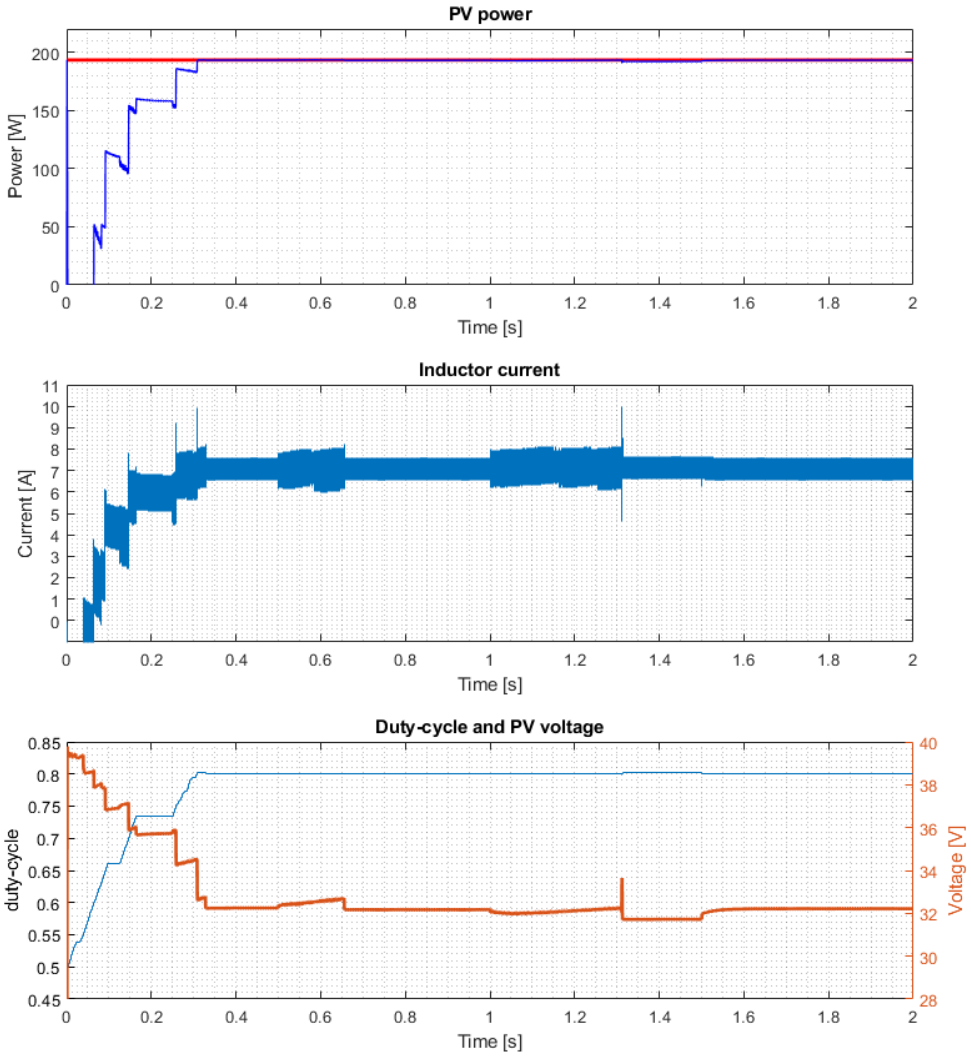

Figure 3.16: PV power variation, inductor current, duty-cycle (blue) and PV voltage (orange) with variable load and STC input conditions.

In Figure 3.16, it can be concluded that the PV power maintains its value in the same MPP (193 W) since the input PV panel variables are constant. The inductor current has an average

value of 7 A and the peaks are according to the duty-cycle changes, which influence the PV panel voltage. Apart from that, the PV voltage is around the V_{mpp} value.

In Figure 3.17 the evolution of the load and battery currents is presented according to the resistive load variation.

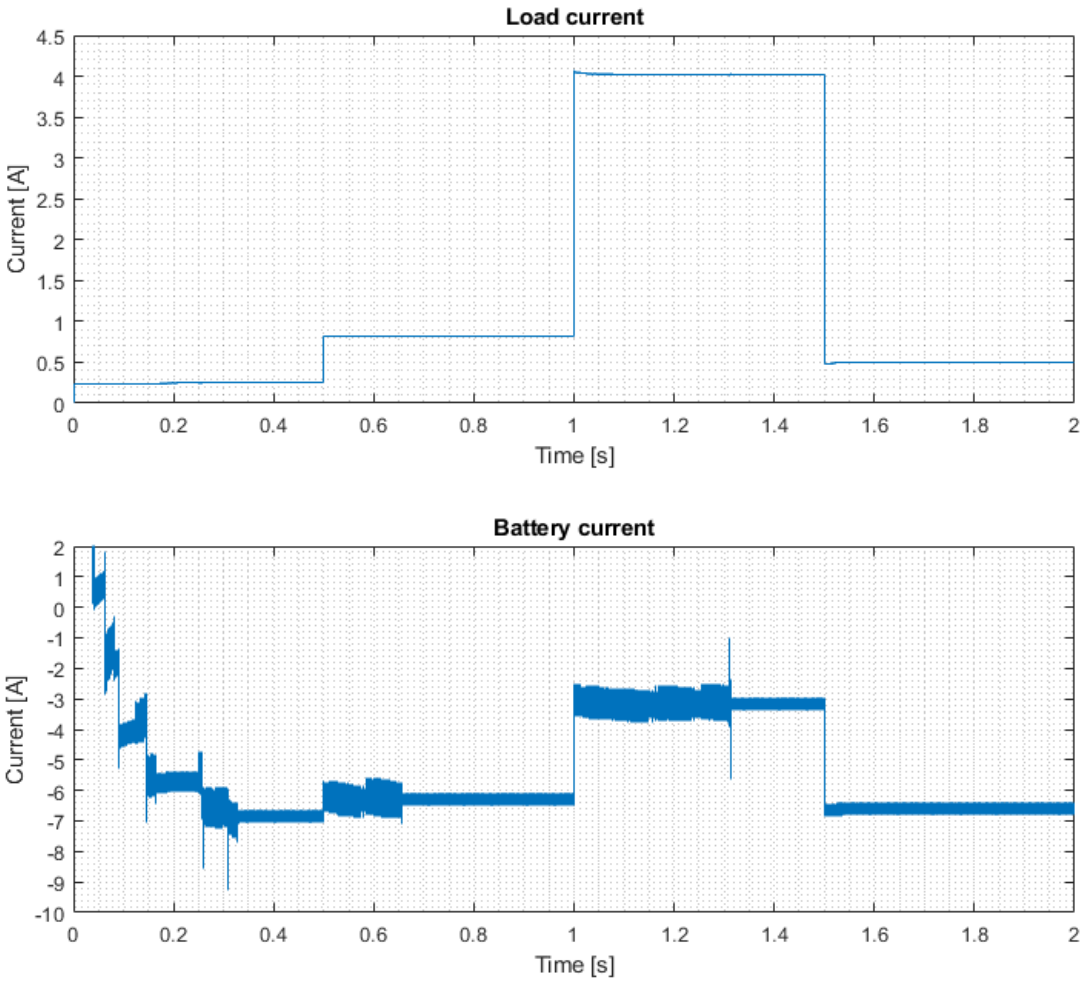

Figure 3.17: Load and battery currents according to load variation.

In the simulated scenario, the current is divided between the battery and the load. It is possible to conclude that the sum of the load current with the battery current (in module) is approximately equal to 7 A, the average inductor current value, on each of the four different time intervals.

The variable resistive load also influences the battery voltage and SoC, visible in Figure 3.18.

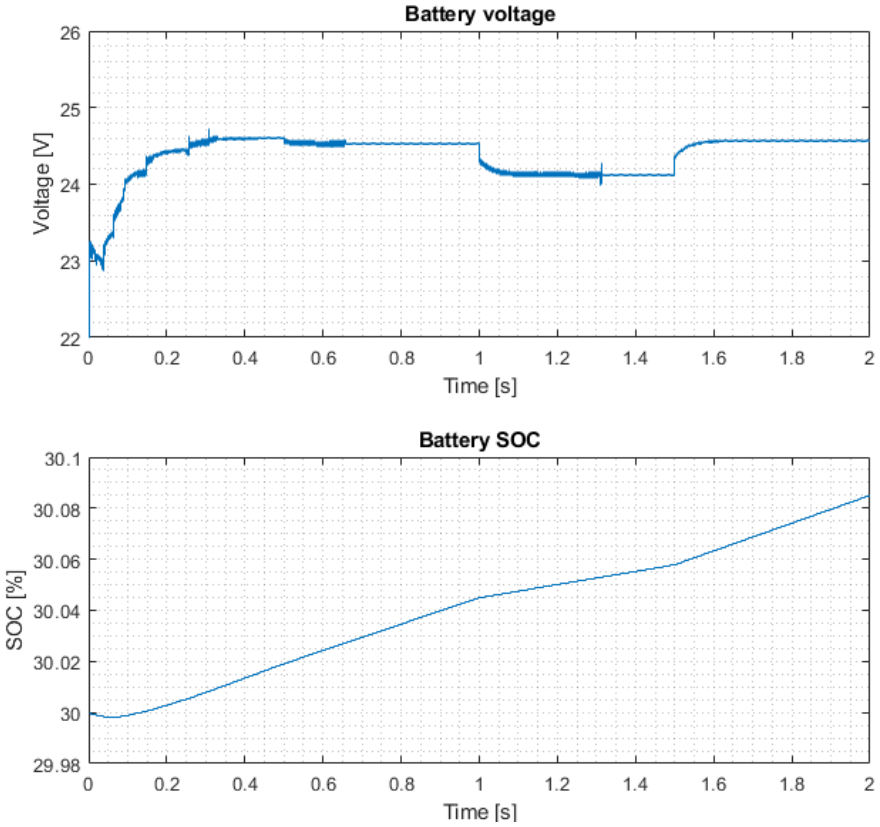

Figure 3.18: Battery measurements according to load variation.

As shown in Figure 3.18, the battery is slightly charged, and the DC bus voltage/ battery is between 24 V and 25 V.

3.2.5 MPPT Stop Condition Test

It is necessary to guarantee a stop condition for the MPPT when the battery is almost fully charged to ensure it will not exceed its maximum voltage value. For this simulation, it was considered a 6S (6 cells in series) Li-ion battery with a maximum voltage equal to 25.2 V (maximum voltage of 4.2 V per cell) and a 3500 mAh capacity. When the battery voltage reaches its maximum value, both MOSFETs are disabled and no current flows through the inductor; the battery starts discharging.

The battery's initial state of charge is defined as 79.87%. According to the implemented stop condition algorithm, if the SoC or the battery voltage exceeds 80% or 25.2 V, respectively, the PWM signal is set to zero, and the enable signal changes to zero blocking the low-side MOSFET. When the battery voltage reaches its nominal value, the MPPT starts working normally.

According to the battery voltage, the evolution of the PV power and inductor current is presented in Figure 3.19.

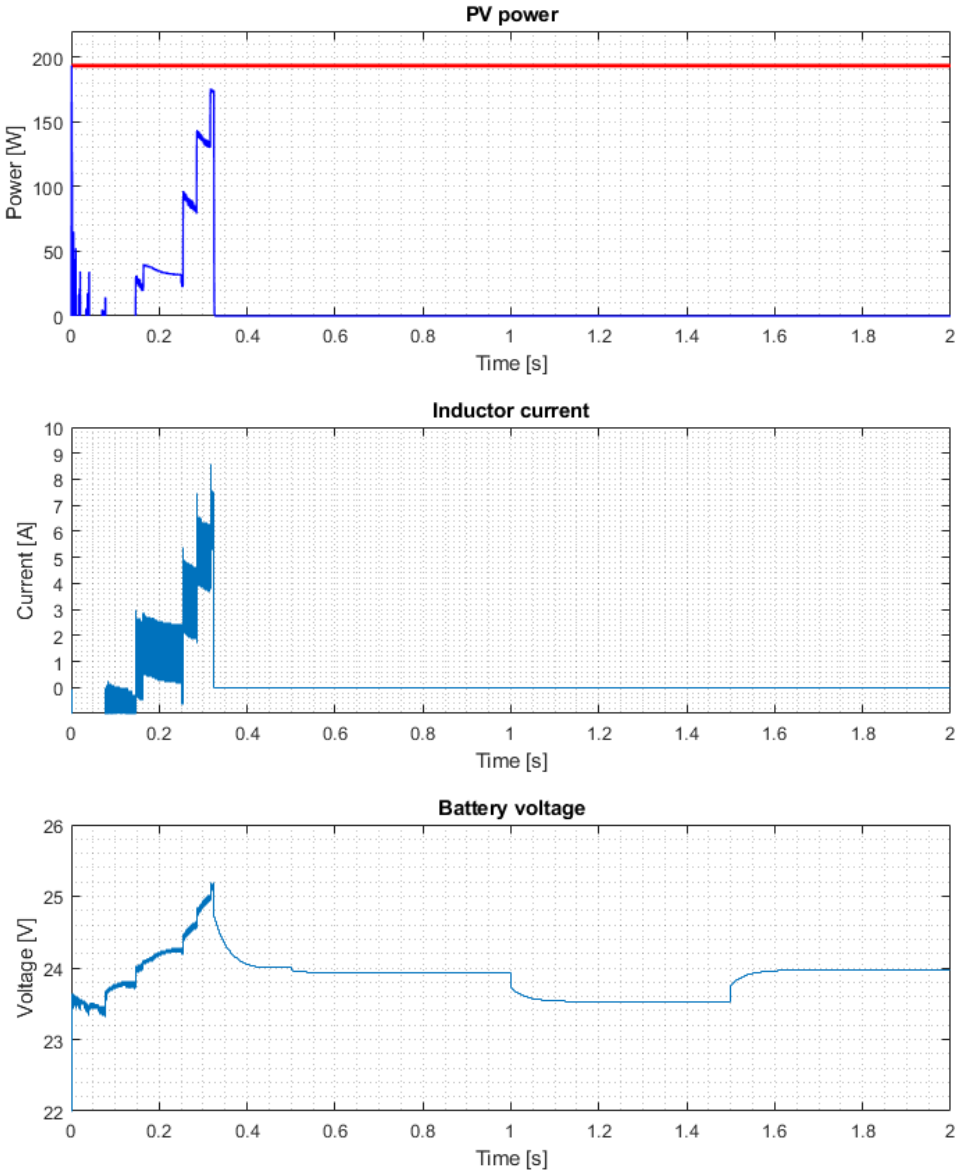

Figure 3.19: PV power, inductor current and battery voltage with MPPT stop condition.

In Figure 3.19, the PV power was increasing, but when the battery voltage reaches its maximum voltage, the MPPT algorithm stops before the PV panel reaches its MPP and stands in open circuit condition. Similarly, the inductor current was increasing until its average value, but when the MPPT stops, it changes to zero.

As before, the load variation influences the battery and load currents, visible in Figure 3.20. The battery SoC evolution is also presented.

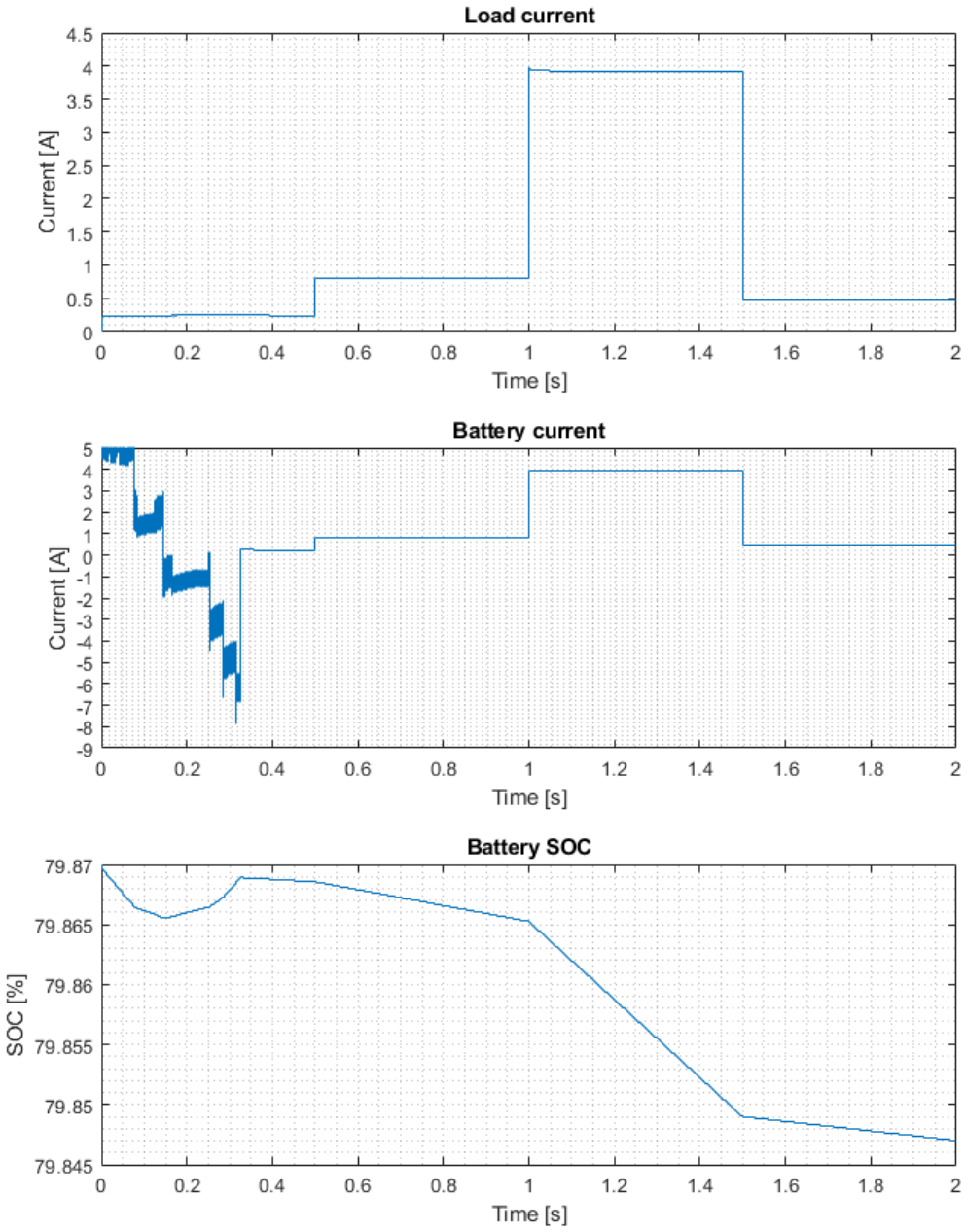

Figure 3.20: Battery and load currents, and SoC with MPPT stop condition.

In this scenario, the battery starts discharging and as no current will flow through the converter, the load current is equal to the battery current, as shown in Figure 3.20.

3.3 Summary

With the algorithm test, it is possible to conclude that the MPPT algorithm takes the PV power until its MPP in almost every input conditions. The simulated rapid temperature variations also perturb the PV power but it immediately converges to the desired MPP.

In the variable load test, the inductor current ripple is influenced by the load variation but its value is inside the defined range. The load variation also influences the PV panel voltage, but it is maintained around its MPP value.

The MPPT stop condition was verified when the battery exceeded its maximum voltage.

In the three tests, the battery was charged or discharged according to the defined conditions, and its voltage variation was inside the expected range. When the load was applied, its current and the battery current were in accordance with the imposed conditions. During all the tests, the inductor current ripple value is inside the defined range of 30%.

Chapter 4

Implementation and Testing

The implementation and testing carried out during this work is divided into two parts: PCB design and test, and MPPT programming and testing.

The PCB mainly incorporates the DC/DC converter, voltage and current measurements, and signal conditioning. It also includes additional features like PWM signals management and communications. The microcontroller board is also assembled on the main PCB.

4.1 Prototyping

The EAGLE software was used for the electrical schematic and PCB design. The final schematic can be seen in Appendix A.1.

The whole circuit can be divided into two main parts: power and control. The power part includes the DC/DC converter, with the sized components in Section 3.1 and the shoot-through and gate protections. The control part includes the microcontroller, its associated logic, and the current and voltages measurements. The chosen microcontroller was *Teensy* 4.1, a 32 & 64-bit microcontroller with a high-performance processor ARM Cortex-M7. However, it was not possible to conduct all experimental tests with it. Thus, an Arduino Uno was used instead for the following tests.

The microcontroller receives three measurements from the circuit: the current from the current sensor at the PV panels input, and the PV input and converter's output voltages from the voltage dividers.

As represented in Appendix A.1, two possible ways of measuring the current were designed. One uses a 3 $m\Omega$ shunt resistor and INA283 (a current shunt monitor) to perform a high-side current measurement. The other is a current sensor with the linear Hall-Effect IC Allegro ACS712.

The shunt resistor allows a current measurement through its minimal voltage drop since it has a very small and precise resistance value. That implies the usage of an amplifier component with high gain to acquire the voltage values, such as the INA283. This current sense amplifier can accurately measure voltages developed across current-sensing resistors on common-mode voltages from -14 V to 80 V.

On the other hand, the Allegro ACS712 outputs an analog signal, $VOUT$, that varies linearly with the sampled current. The selected IC has a 66 mV/A output sensitivity and can measure a bidirectional current up to 30 A.

In this project, the latter current measurement method was selected, allowing a more direct measurement. The PCB is ready to perform the alternative current sensing if necessary.

Two voltage regulators, L7812 and L7805, were used to obtain two auxiliary power supplies of 12 V and 5 V, respectively. That allows an independent source to power the ICs in the circuit, such as the $SN74LS00$ and the current sensor with 5 V and the LTC4444 with 12 V.

The microcontroller generates a PWM signal with a 50 kHz frequency, and controls the high-side MOSFET through the gate driver LTC4444. The IC $SN74LS00$, composed of four 2-input NAND logic ports, is used to generate the complementary PWM sent to the gate driver (BINP input) to control the low-side MOSFET. As aforementioned in the simulations section, the enable signal can turn off the low-side MOSFET if necessary. As illustrated in Figure 4.1 three NAND gates were used, and the respective truth table is represented in Table 4.1.

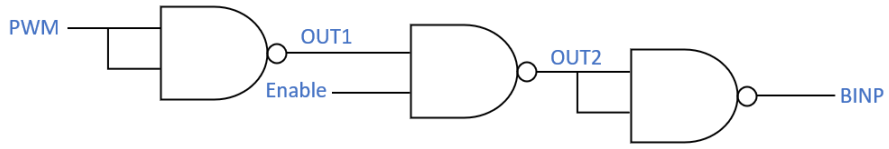

Figure 4.1: Implemented logic with 3 NAND logic gates from SN74LS00.

Table 4.1: Implemented logic with SN74LS00.

PWM	OUT 1	ENABLE	OUT 2	BINP
0	1	0	1	0
0	1	1	0	1
1	0	0	1	0
1	0	1	1	0

4.2 PCB Design and Assembly

Concluding the electrical schematic, the PCB design took place. This was an essential task since it defined the components' physical layout and connections. The PCB was ordered with 70 μm thick, with two copper layers.

Some restrictions were accounted for when designing: short tracks between the microcontroller and the MOSFET driver and gates, separating the power from the control parts and considering the flowing current to define the PCB's track width.

The microcontroller required special attention when powered by the L7805. When performing the tests, it was helpful to connect the microcontroller to the computer for debugging. However, the microcontroller can't be powered twice by the VIN and the VUSB pins to prevent the possibility of power flowing back into the computer. Therefore, the track between the L7805 and the rest of the circuit was interrupted by a jumper. In this way, the jumper can be placed when there is no USB connection and the L7805 powers the microcontroller, and it is removed when necessary to have the USB connection to the computer.

The final prototype PCB, with the components, is shown in Figure 4.2.

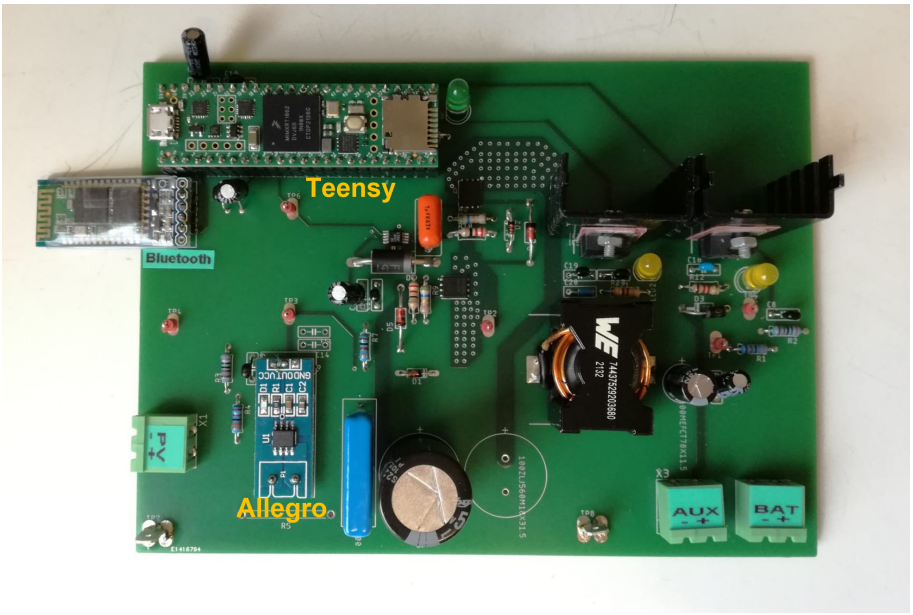

Figure 4.2: Final prototype PCB.

4.3 Algorithm Operation

Microcontroller programming is essential to guarantee the correct operation of the MPPT algorithm. The code can be divided into parts: reading the input variables, namely the PV current and voltage and the battery voltage; and using those values in the MPPT algorithm to calculate the duty-cycle for the PWM control signal.

The algorithm operation, described below, is represented in Figure 4.3.

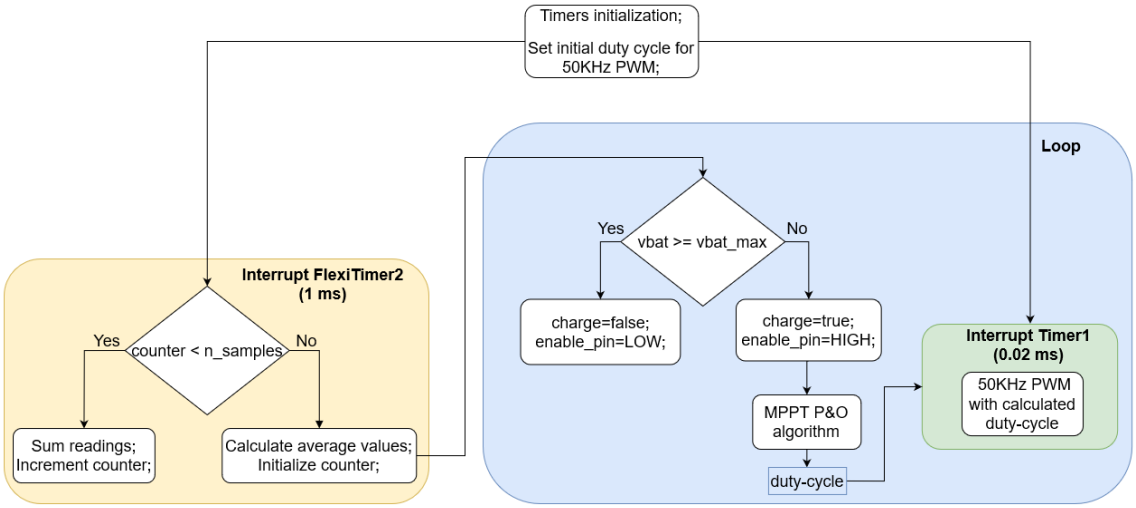

Figure 4.3: Algorithm operation flowchart.

Arduino Uno has three timers: Timer0, Timer1, and Timer2. Timer0 and Timer2 are 8-bit, and Timer1 is 16-bit. The latter was used to generate a PWM signal with a 50 kHz frequency. Timer2 was used through *FlexiTimer2* library to create an interrupt that calls a function to do the variables reading. In order to filter the readings, a number of samples was defined. For example, the input values are read every 1 ms, and an average calculation is done with a defined number of samples. Then the averaged value is used for the MPPT algorithm. In order to have a 20 Hz MPPT frequency, using a 1 ms interrupt to call the reading function, the number of samples would have to be 50. Thus, the final values are generated every 50 ms, creating a 20 Hz MPPT frequency. Therefore, the interrupt and the specified number of samples are related to one another to define the MPPT algorithm frequency.

Firstly, the MPPT frequency and the duty-cycle step (*deltaD* in Figure 2.31) started with the values implemented in the simulations but were adjusted during the tests to improve the measurement stability. An MPPT frequency of 1kHz was very high considering the speed of the actual temperature and irradiance variations, justifying the MPPT frequency decrease.

4.4 Experimental Results

The experimental tests were an iterative process that started with simple tests for the power circuit and then proceeded to more advanced tests with a PV panel to verify the MPPT algorithm.

First, the control signals were tested. Then, the tests proceeded to the PWM signals at 50 kHz (for the high and low-side MOSFETs) generation and conditioning. Finally, the gate driver operation was verified.

An illustrative diagram of the tested circuit is presented in Figure 4.4.

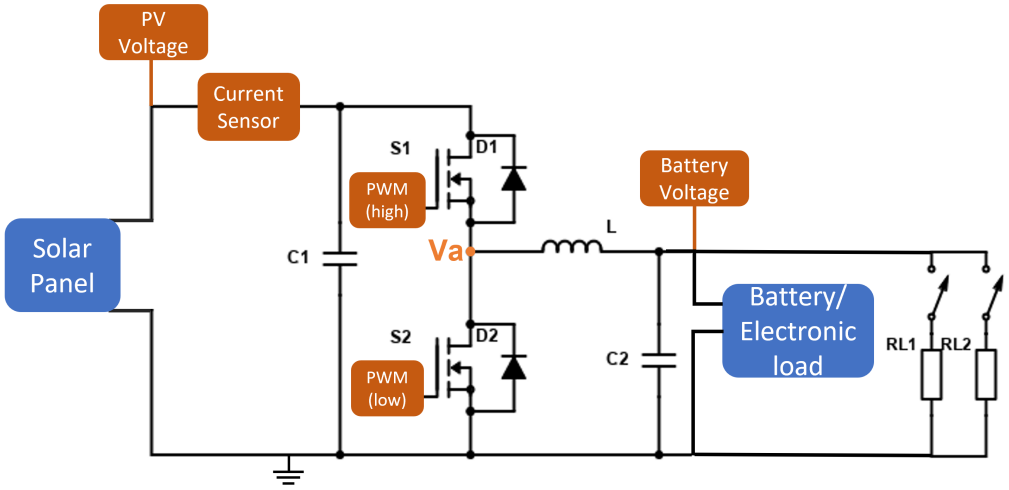

Figure 4.4: Illustrative diagram of the tested circuit.

4.4.1 Power Circuit Tests

Having verified that the implemented logic was working correctly, the DC/DC converter was tested.

A DC power supply was placed in the auxiliary connector (*AUX*) to provide the necessary 12 V and 5 V internal power supplies. Another power supply was placed at the input connector (*PV*) with a voltage equal to 36 V. The 50 kHz PWM signal was set with a duty-cycle of 70%, obtaining an output voltage of approximately 24 V.

A large bandwidth current probe with a 20 mV/A sensitivity was used to measure the currents presented in the following figures. It is an AC probe thus it does not measure DC components. Three power loads resistors with 10 Ω were used to varie the applied load. The *Va*, in Figure 4.4 is the point between the high-side MOSFET source and the low-side MOSFET drain.

In Figure 4.5, Figure 4.6 and Figure 4.7, the load was changed between one resistor, two parallel resistors and three parallel resistors, respectively. Therefore, the circuit output power is 57.6 W, 115.2 W, and 172.8 W, respectively. As expected, the high-side MOSFET current has a waveform equal to the inductor current and thus it is possible to estimate the inductor average value. In Figure 4.5, Figure 4.6 and Figure 4.7 the inductor average current is approximately 2.5 A, 5 A and 7.5 A, respectively. In the last experiment, it was measured the inductor current, which has a ripple of approximately 3 A. This ripple is slightly higher then the one used for sizing the inductor in Section 3.1.1 due to the presence of a small saturation level.

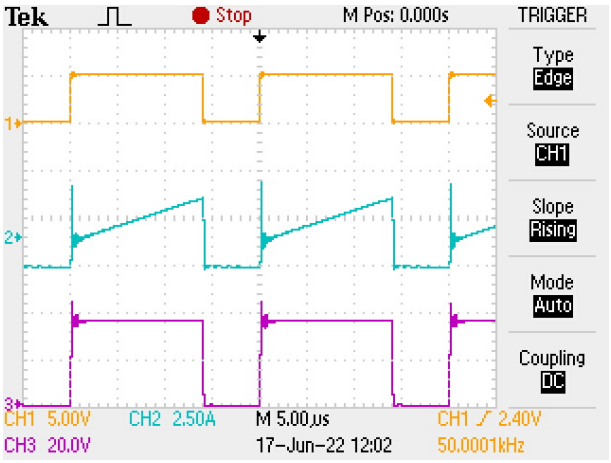

Figure 4.5: PWM (orange), high-side MOSFET current (blue) and Va voltage (purple): one load.

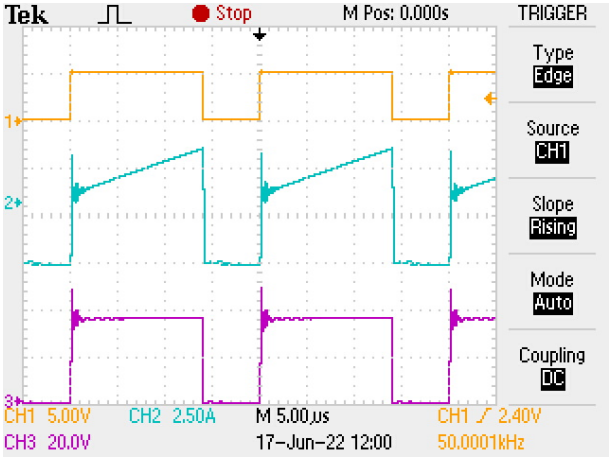

Figure 4.6: PWM (orange), high-side MOSFET current (blue) and Va voltage (purple): two parallel loads.

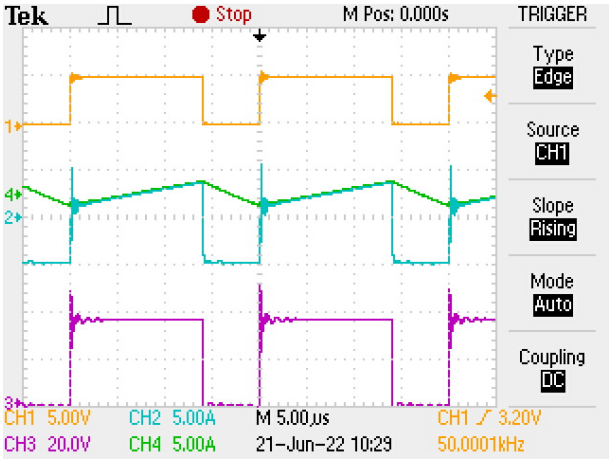

Figure 4.7: PWM (orange), high-side MOSFET current (blue), Va voltage (purple) and inductor current (green): three parallel loads.

Figure 4.8 shows the high-side MOSFET switching, using an input voltage of 36 V and output power of 173 W.

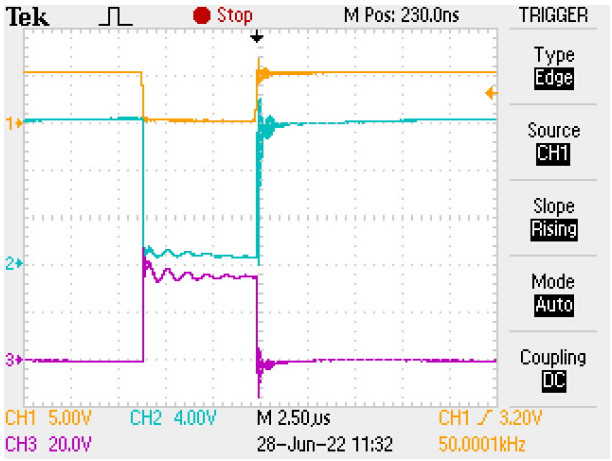

Figure 4.8: Turn-on MOSFET switching: PWM signal (orange), high-side MOSFET gate-source voltage (blue) and drain-source voltage (purple).

Figure 4.9 and Figure 4.10 show the detailed turn-on and turn-off of the high-side MOSFET, respectively, its gate-source and the drain-source voltages. The turn-on switching has very noisy signals, but it can be observed the very fast switching; less than 100 ns during turn-on and turn-off, slightly higher in the turn-on. Since the MOSFET itself has similar rise and fall times, this difference might have been caused by the implemented simple shoot-through circuit in Section 2.3.6.1.

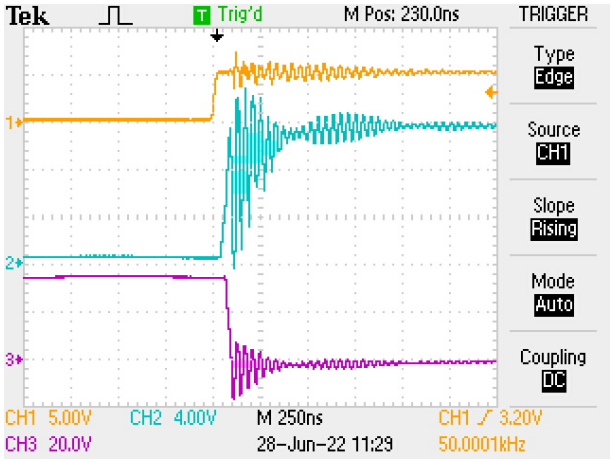

Figure 4.9: Turn-on MOSFET switching: PWM signal (orange), high-side MOSFET gate-source voltage (blue) and drain-source voltage (purple).

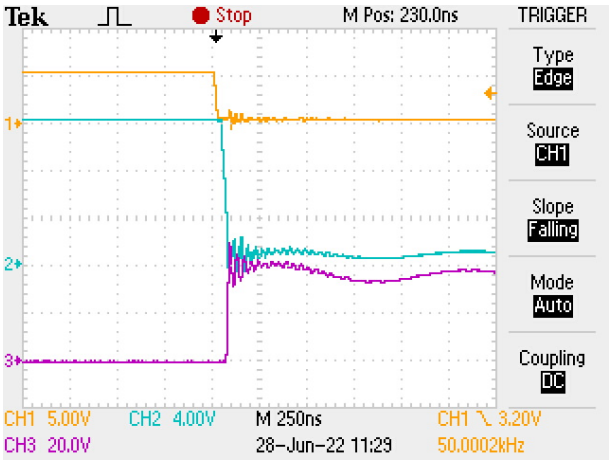

Figure 4.10: Turn-off MOSFET switching: PWM signal (orange), gate-source voltage (blue) and drain-source voltage (purple).

4.4.1.1 Converter Efficiency

Figure 4.11 shows the converter efficiency for different output power values. For this experiment, the duty-cycle was fixed, and the output voltage was maintained at 24 V by adjusting the input voltage.

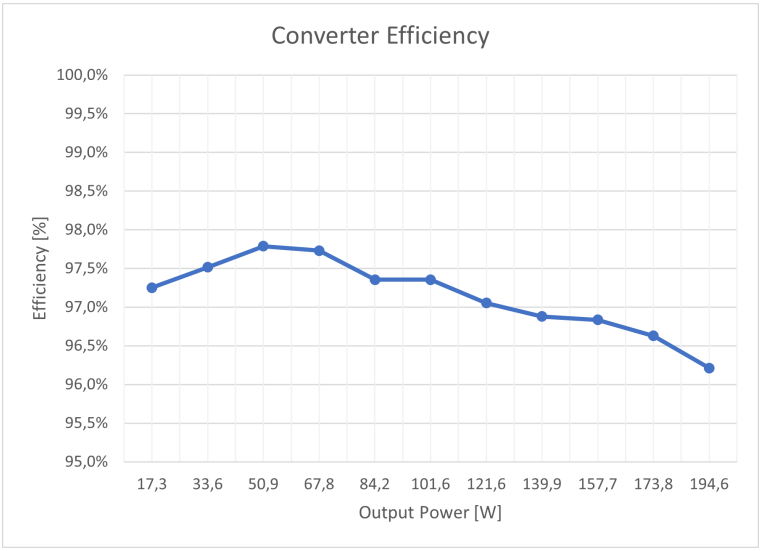

Figure 4.11: Converter Efficiency for different output power values

As it is possible to observe, the converter has high efficiency. Even for the highest power value tested, which corresponds to the desired power when using the UAV PV panel, it presents a good efficiency.

4.4.2 MPPT Algorithm Tests

Since the PV panel, with 193 W, that is meant to be used in the UAV is not yet available for testing, an alternative panel was used. Four PV modules were connected, each one with the following characteristics at 1000 W/m^2 and AM1.5 25ºC: V_{oc}=21 V, V_{mpp}=17 V and maximum power equal to 10 W.

Therefore, with the defined connection for the four modules, shown in Figure 4.12, the panel's output voltage is 34 V, the total current is approximately 1.2 A and the total power is 40.8 W.

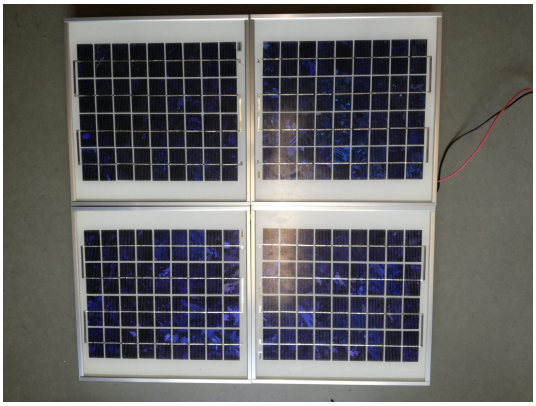

(a) Assembled PV panel for experimental tests

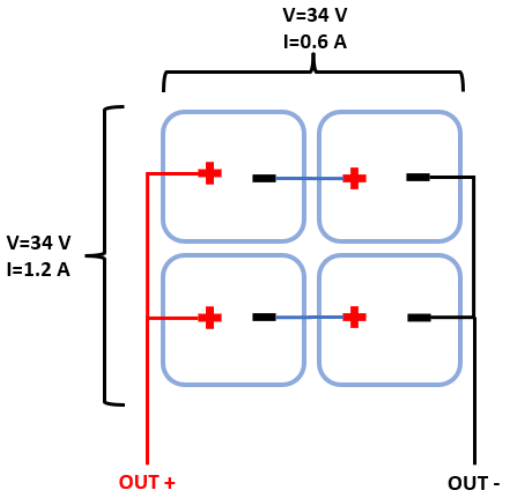

(b) 2 series PV modules in parallel

Figure 4.12: PV panel for experimental tests.

In the following tests, to simulate the battery, a programmable DC electronic load from BK Precision was used. Its voltage was fixed to 24 V.

Firstly, it was verified the steady-state PV panel's voltage and current and the convergence of the MPP according to sudden changes in the irradiance.

As one can observe in Figure 4.13, the PV panel voltage is approximately 32 V and the PV power is maintained at 35 W.

In Figure 4.14, due to a variation in the irradiance, between t=6.5 s and t=16.5 s, the PV current decreases almost to a half and consequently, so does the PV power. After, the latter returns to its initial value of approximately 32 W.

Similarly, in Figure 4.15, the PV power changes due to a variation in the irradiance, and even after the shading, it returns closer to its initial value. Finally, the power decreases to zero since the panel was completely shaded.

Then, it can be concluded that the MPPT algorithm operates in a very good tracking mode, either in steady-state, and dynamic conditions.

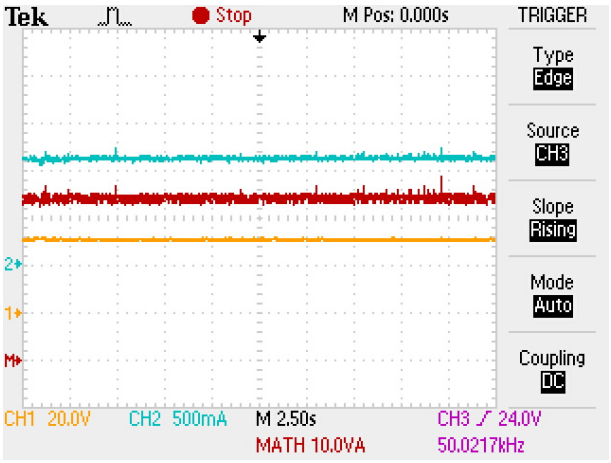

Figure 4.13: PV voltage (yellow), current (blue) and power (red) with clear sky conditions.

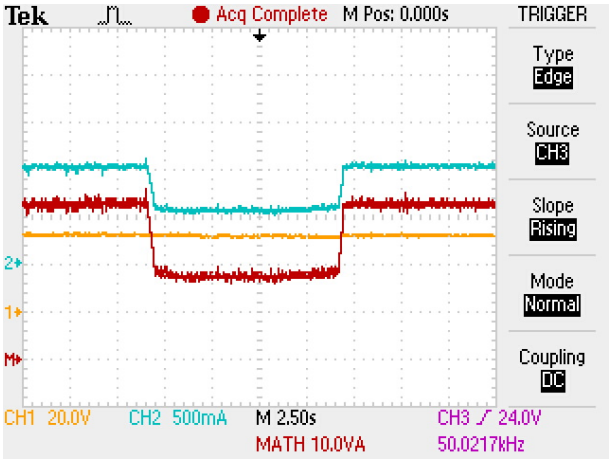

Figure 4.14: PV voltage (yellow), current (blue) and power (red) with abrupt irradiance variation.

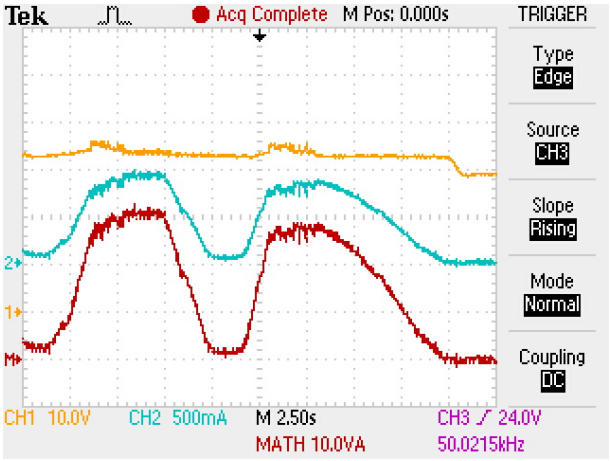

Figure 4.15: PV voltage (yellow), current (blue) and power (red) with slow irradiance variation.

4.4.3 Load Variation Test

Intending to verify the current behavior when a load is applied at the converter output, a variable resistor with a value of 33 Ω was placed in parallel with the electronic load. A circuit breaker was placed in the load wiring and its current can be observed in Figure 4.16.

In steady-state, i.e., with constant irradiance conditions, the load was switched ON and OFF. The current is divided between the resistor and the electronic load. As the electronic load has a fixed value of 24 V, a 33 Ω resistor imposes a 0.73 A output current. On the other hand, the electronic load current will decrease from 1.4 A to approximately half, since the other part flows to the load.

The PV power is at its MPP, i.e., 40 W. From the electronic load current, which is the output current, and considering a fixed output voltage of 24 V, the output power is approximately 34 W.

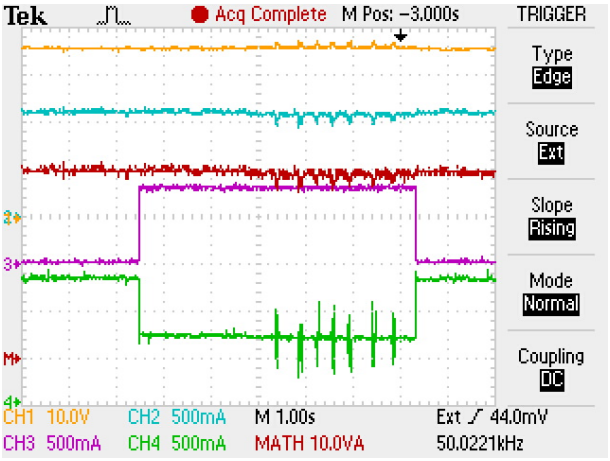

Figure 4.16: PV voltage (yellow), current (blue), power (red), load resistor current (purple) and electronic load current (green).

4.5 Summary

With the power circuit tests, it was possible to verify the correct circuit operation up to an output power of 173 W, which is close enough to the desired power for the UAV panels, validating the PCB and components sizing.

The 40 W PV panel tests allowed the validation of the implemented MPPT algorithm in steady-state conditions, and when changing the irradiance with abrupt or smoother transitions. In steady-state conditions, the tests were made using an electronic load and variable resistive load. In all conditions, the algorithm maintained the PV panel operating in its maximum power point.

Chapter 5

Conclusions

The goal of this Master's dissertation was to design, implement and test a MPPT solar charge controller for a long endurance solar UAV. Mainly, this involves the definition of the system architecture, the establishment of requirements, the design of all passive and active components, the definition of appropriate models, the simulation of relevant steady-state and transient conditions, and the implementation and testing of a prototype.

This dissertation presents the state of the art of the system's fundamental parts, namely the photovoltaic cells and arrangements, battery types, non-isolated DC/DC converters, charge controllers, namely the MPPT algorithm, and the BMS systems. The literature review allowed the familiarization with the primary requirements and power and energy specifications of the system.

From the mission requirements and UAV physical dimensions, a PV array of 56 cells in series, with 32.6 V and 193 W, was established. According to the input/output voltage ratio, power level, and isolation specification, a non-isolated DC/DC buck converter was selected, designed and validated in the presented simulations and experimental results.

The dynamic simulations with the converter's switching model allowed the verification of its fast dynamics when step variations in the PV panels conditions (irradiance and temperature) were applied and also its fast response when step variations in the DC bus load were applied. Moreover, these results allow concluding that the MPPT algorithm was correctly implemented, and it was possible to proceed with experimental tests.

The experimental results verified the correct sizing and PCB design with a power level close to the one defined for the UAV panel, with high DC/DC converter efficiency. The MPPT algorithm was validated in an alternative PV panel with lower power. Its correct operation under different conditions with irradiance and load variations was verified.

Concluding, the implemented MPPT allowed the expected power conversion between the PV panel and the electronic load. Thus, its tracking capability and efficiency were verified.

5.1 Future Work

Regarding the simulation, in the future, it would be interesting to simulate the system with the converter's average model to observe the battery's charge, discharge, and SoC in longer time intervals.

The BMS will be implemented to enable the usage of Li-ion or LiPo batteries. It should support 6S-12S cell batteries and perform accurate battery measurements and active cell balancing during charging and discharging. Besides, common features such as wired connectivity (CAN, I2C or SPI) and wireless connection (NFC) should be implemented for both MPPT and BMS.

The other team members are developing the UAV mechanical and avionics parts. Thus, this first prototype project is still ongoing. After the whole electrical system is implemented, including the emergency system and all the needed protection systems, it will be tested in the laboratory with the certification standard (AEC-Q100 Automotive standard), [42].

Some important parameters should be evaluated and might impose some iterations in the PCB design. The study and tests of the system's operation in large temperature ranges and failure or degraded modes are possible next steps.

Appendix A

Appendix

A.1 Appendix A

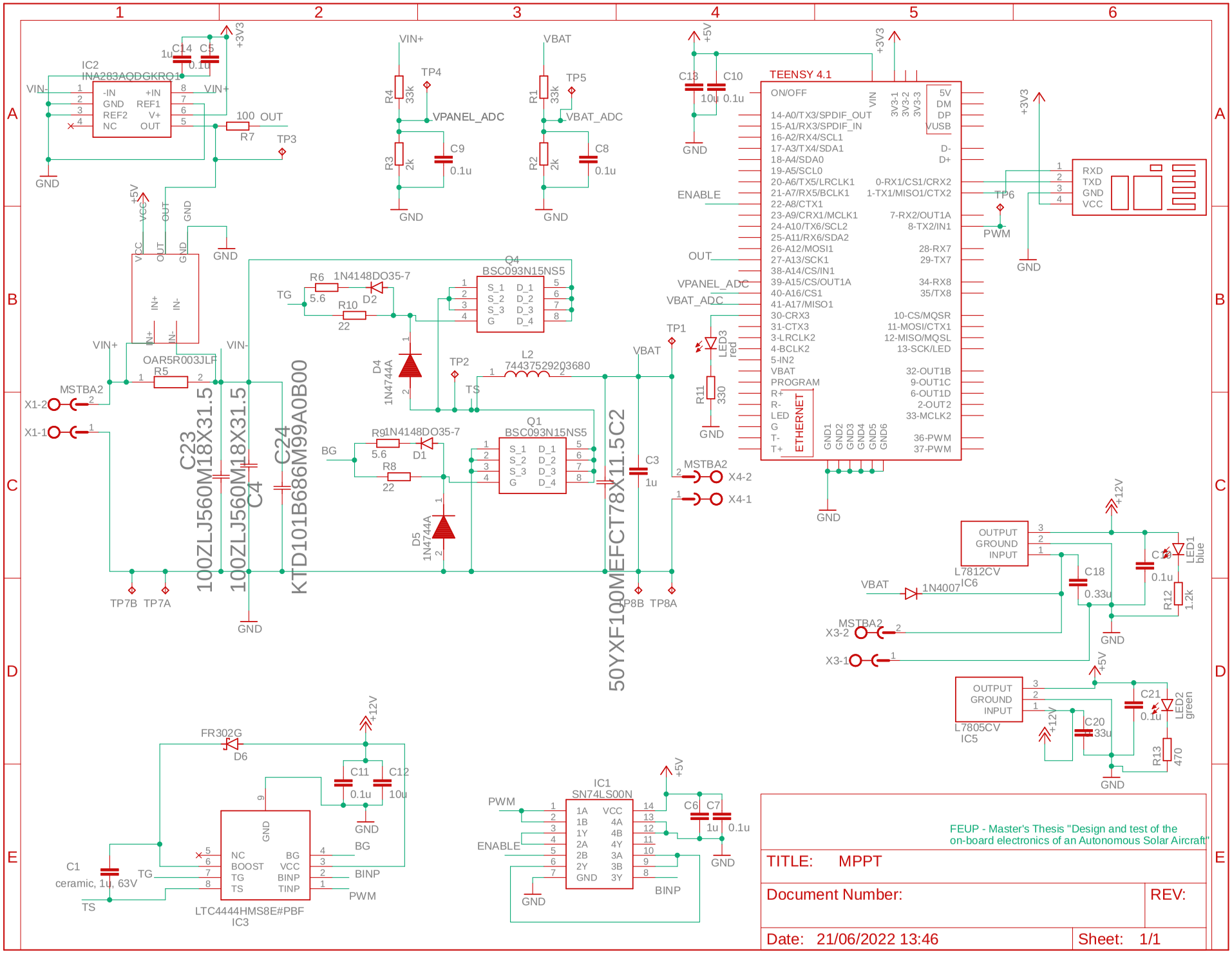
TEENSY 4.1
IC2
INA283AQDGKRQ1
IC1
SN74LS00N
IC3
LTC4444HMS8E#PBF
IC5
L7805CV
IC6
L7812CV
Q1
BSC093N15NS5
Q4
BSC093N15NS5
L2
74437529203680
OAR5R003JLF
100ZLJ560M18X31.5
KTD101B686M99A0B00
50YXF100MEFCT78X11.5C2
1N4148DO35-7
1N4744A
1N4007
FR302G
ETHERNET
FEUP - Master's Thesis "Design and test of the on-board electronics of an Autonomous Solar Aircraft"
TITLE: MPPT
Document Number:
REV:
Date: 21/06/2022 13:46
Sheet: 1/1

A.2 Appendix B

DetailedDesignData/NON24_D_20_P_10_WE3.55-9.3_E193-10.22_Inverted.txt

Report:
Warning - Takeoff I : 0
Warning - Takeoff distance too high : 0

Warning - Climb I night : 0

Warning - Cruise I day : 0
Warning - Cruise f day : 0

Warning - Landing distance to high : 0

Warning - Battery energy too low : 0

Warning - Top speed too low day : 0
Warning - V to high for max Re of polars day : 0
Warning - Top speed I : 0
Warning - Top speed too low night : 0
Warning - V to high for max Re of polars night : 0
Warning - Top speed I night : 0

Report General Day:
V cruise day : 11.3 11.8 12.3 12.8 13.3
13.8 14.3 14.8 15.3 15.8 16.3 16.8 17.3 17.8
18.3 18.8
Warning - 1.2Vstall day : 1 1 1 0 0 0
0 0 0 0 0 0 0 0 0 0
Warning - I cruise day : NaN NaN NaN 0 0
0 0 0 0 0 0 0 0 0 0
Warning - f cruise day : NaN NaN NaN 0 0
0 0 0 0 0 0 0 0 0 0
Report General night:
V cruise night : 9.9 10.4 10.9 11.4 11.9
12.4 12.9 13.4 13.9 14.4 14.9 15.4 15.9 16.4
16.9 17.4 17.9 18.4 18.9
Warning - 1.2Vstall night : 1 1 0 0 0 0
0 0 0 0 0 0 0 0 0 0
0 0
Warning - I cruise night : NaN NaN 0 0 0
0 0 0 0 0 0 0 0 0 0
0 0 0
Warning - f cruise night : NaN NaN 0 0 0
0 0 0 0 0 0 0 0 0 0
0 0 0

Geometry wing:
b of wing = 5.29 m
c of wing = 0.55 m
AR of wing = 9.6
b of tail real = 1.39 m
c of tail = 0.23 m
AR of tail = 4.8
Angle of tail (w/h) = 37.1 °

Geography:
Takeoff time = 4.00 h
Landing time = 22.00 h

```
Time takeoff before SR     = 1.03 h
Time landing after SS      = 3.03 h
Time of day/night          = 13.93/10.07 h
Climb time day             = 2.50 h
Cruise altitude day        = 3000 m
Glide time day             = 3.00 h
Cruise altitude night      = 500 m
Takeoff altitude           = 0 m
Landing altitude           = 300 m
Latitude                   = 30.0 °
Day                        = 170
Max irradiance             = 1100 W/m2

Geometry propeller:
Number of motor/propeller  = 1
D                          = 20 in
P                          = 10 in

Masses:
Mass of avionics           = 3.500 kg
Mass of payload            = 0.400 kg
Mass of av+pld             = 3.900 kg

Mass of BEC                = 0.000 kg

Mass of BMS                = 0.100 kg

Mass of Emergency          = 0.300 kg

Mass of solar cells        = 1.761 kg (A=2.62 m^2)
Mass of MPPT               = 0.540 kg
Mass of battery cell       = 1.270 kg
Mass of battery            = 6.477 kg (1S5P)
Mass of power system       = 7.417 kg

Mass of ESC                = 0.200 kg
Mass of motor              = 0.445 kg
Mass of gearbox            = 0.000 kg
Mass of propeller          = 0.100 kg
Mass of prop system        = 0.745 kg

Mass of tail               = 0.453 kg
Mass of tail boom          = 0.655 kg
Mass of fuselage           = 0.831 kg
Mass of wing               = 3.913 kg
Mass of stucture           = 5.853 kg

Mass of aux. car           = 0.000 kg
Mass of TO with car        = 19.676 kg

Total mass                 = 19.676 kg

Energy systems:
Battery nominal V          = 22.2 V
Battery nominal cap        = 8800 mAh
Solar panel efficiency     = 0.21
Camber efficiency          = 0.90
MPPT efficiency            = 0.95
```

Cruise:
V cruise day (eq.)   = 14.3 m/s (12.3 m/s)
V stall day (eq.)   = 10.2 m/s (8.8 m/s)
V cruise/stall day   = 1.4

Mission profile:
  /‾‾\
_/   _

Takeoff:
Min S takeoff   = 30.2 m
Takeoff velocity (eq.)   = 10.5 m/s (10.5 m/s)
AOA wing takeoff   = 1.0 deg
Energy takeoff   = 6956.0 J
Maximum current per motor   = 50.00 A

Climb/Climb+Cruise before sunrise:
Climb night:
Climb time   = 2.45 h
Energy climb   = 3047963.1 J
Avg climb rate   = 0.34 m/s
Maximum current per motor   = 22.11 A
Throttle - f   = 0.69

Cruise/Climb+Cruise before sunrise:
Cruise day:
Drag during cruise day   = 8.59 N
L/D cruise day   = 22.46
f cruise day   = 0.64
Current each motor day   = 13.48 A
P ele all mot cruise day   = 190 W
TS day   = 96.5 m/s
TS/a day   = 0.29
RPM day   = 3627.2 rpm
J cruise day   = 0.43
Energy cruise day   = 11295289 J
Power cruise day   = 267 W
Power required day   = 123 W
Battery efficiency day   = 0.98
Prop efficiency day   = 0.64

Average rate of glide   = 0.3 m/s
V glide eq   = 11.6 m/s
Best energy glide night   = 1580495.3 J
Maximum current per motor   = 9.73 A

Landing:
Landing distance   = 53.5 m
Landing velocity (eq.)   = 11.5 m/s (11.3 m/s)

Energy balance:
Energy Sun   = 14551567 J (4042.1 Wh)
Energy batery (use)   = 3349029 J (930.3 Wh)
Minimum energy bat (use)   = 311581 J (86.6 Wh)
Maximum energy bat (use)   = 3349029 J (930.3 Wh)

Cruise AOA of wing:

```
Incidence wing                = 2.1 deg
Incidence tail                = -0.4 deg
Alpha plane night             = 0.0 deg
Static stability              = 0.14
Day tail control              = 10.5 deg

Descend:
Descend time day           = 0.98 h
Avg descend rate day       = 0.77 m/s
Descend time night         = 0.08 h
Avg descend rate night     = 0.72 m/s

Top Speed:
Top Speed day (eq.)        = 24.2 m/s (20.9 m/s)
Current per motor day      = 28.73 A
Top Speed night (eq.)      = 22.2 m/s (21.7 m/s)
Current per motor night    = 38.37 A

Power inside fuselage:
Power pld and av day       = 62 W
Power of motor sys. day    = 14 W
Power pld and av night     = 62 W
Power of motor sys. night  = 14 W
Power of mppt              = 28 W
Power during day           = 104 W
Power during night         = 77 W
```

A.3 Appendix C

A.3.1 Normal and failure modes

As many systems, the solar aircraft has two main operation modes: normal and failure. The normal mode is when all elements or subsystems are working inside their specifications values. The failure mode is represented by the emergency power supply, as aforementioned in Section 1.2. It could also be considered a third operation mode, the degraded mode. This mode corresponds to the system operation with some parameters outside their normal range or some subsystems turned off. Usually, the degraded mode has a large set of possibilities with very different degrees of probability. In this work it will only be considered the normal and the failure modes.

Normal Mode

Normal mode occurs when all subsystems operate in their expected and desired conditions. In this mode, a specified set of scenarios should be evaluated in order to provide reliable simulation results. Accordingly, the model should be exhaustively tested in different scenarios. For example, one scenario could be the overproduction of energy from the solar cells with the battery fully charged and another scenario is the opposite one, the case of energy shortcoming from the solar cells due to atmospheric conditions with the battery approaching a warning level of discharge. Other scenarios can be tested regarding the load characteristics, either dynamically and in steady-state. Additionally, the simulation of certain conditions that may cause the activation of the emergency power supply should be carried out.

Failure Mode

A system like the one considered in this work is subject to faults and failures. The degree of importance of each one is quite variable but there are some that could be dangerous and put the mission at high risk. Thus, it is needed to develop a study that could identify the potential failures, their causes and effects, and design solutions that can mitigate these effects. There are several approaches and methodologies to conduct such analysis: Failure Mode and Effects Analysis (FMEA), Fault Tree Analysis (FTA), Event Tree Analysis (ETA), Fish-bone analysis, Pareto charts, etc., [43] [44].

In this work, the UAV subsystem under analysis is the power and energy systems. The emergency system, presented in Figure 1.1, prevents significant damage by enabling a safe aircraft landing in case of any power failure.

Among the listed methods, the FMEA method is chosen in order to assess the importance of potential failures, its possible causes and the mitigation measures for the considered subsystem, focusing on the hardware part, presented in Figure A.1.

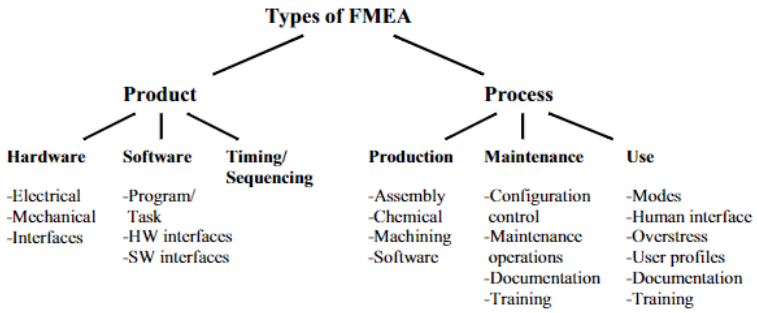

Figure A.1: FMEA types [45].

FMEA can be performed in six steps [46]:

- Define system and its associated requirements;
- Establish ground rules;
- Describe the system and its associated functional blocks;
- Identify failure modes and their associated effects;
- Identifications of possible causes;
- Document the analysis and risk reduction.

There is also the possibility of combining other safety and reliability method such as the aforementioned Fault Tree Analysis (FTA) to provide a more complete and reliable analysis tool.

References

[1] SYSTEC Research Center for Systems and Technologies. [Online] https://5cfa51f8b87b1.site123.me/. Accessed: january 2022.

[2] SunPower C60 solar cell. [Online] http://eshop.terms.eu/_data/s_3386/files/1379942540-sunpower_c60_bin_ghi.pdf. Accessed: january 2022.

[3] Z. Guo X.Zhu and Z. Hou. "Solar-powered airplanes: A historical perspective and future challenges". *Progress in Aerospace Sciences*, 71:36–53, november 2014. doi:10.1016/j.paerosci.2014.06.003.

[4] A.Noth. "History of Solar Flight". Technical report, Autonomous Systems Lab, Swiss Federal Institute of Technology Zürich, 2008.

[5] Helios Solar Aircraft. [Online] https://www.nasa.gov/centers/dryden/news/ResearchUpdate/Helios/. Accessed: june 2022.

[6] Zephyr Solar Aircraft. [Online] https://www.airforce-technology.com/projects/zephyr/. Accessed: june 2022.

[7] Swiss solar plane ends round-the-world tour. [Online] https://www.swissinfo.ch/eng/record-breaker_swiss-solar-plane-ends-round-the-world-tour/41329902. Accessed: june 2022.

[8] This Autonomous Solar-Powered Aircraft Will Fly for 90 Days Straight. [Online] https://singularityhub.com/2021/08/13/this-autonomous-solar-powered-aircraft-aims-to-fly-for-90-days-straight/. Accessed june 2022.

[9] NREL Best Research-Cell Efficiency Chart. [Online] https://www.nrel.gov/pv/cell-efficiency.html. Accessed: june 2022.

[10] A Not-So-Short History of Unmanned Aerial Vehicles (UAV). [Online] https://consortiq.com/uas-resources/short-history-unmanned-aerial-vehicles-uavs. Accessed: june 2022.

[11] Will COVID-19 lead to a drone renaissance? [Online] https://consortiq.com/uas-resourceswill-covid-19-lead-to-a-drone-renaissance. Accessed: june 2022.

[12] The History of AERL and the MPPT Solar Charge Controller. [Online] https://www.aerl.com.au/mppt-solar-charge-controller-history/. Accessed: june 2022.

[13] Genasun GVN-8 MPPT. [Online] https://cdn.shopify.com/s/files/1/0062/2959/0114/files/Genasun_GVB-8_Datasheet-ETL-2018.pdf?5193887046331177433. Accessed: june 2022.

[14] P. Hersch and K. Zweibel. "Basic photovoltaic principles and methods". *Technical Information Office*, February 1982. doi:10.2172/5191389.

[15] A. Labouret and M.Villoz. *Solar Photovoltaic Energy*. UK: Institution of Engineering and Technology, 2010.

[16] M. R. AlRashidi, M. F. AlHajri, K. M. El-Naggar, and A. K. Al-Othman. "A new estimation approach for determining the I-V characteristics of solar cells". *Solar Energy*, 85:1543–1550, May 2011. doi:10.1016/j.solener.2011.04.013.

[17] V. Bala Raju and Ch. Chengaiah. "A Comprehensive Study on Re-arrangement of Modules Based TCT Configurations of Partial Shaded PV Array with Shade Dispersion Method". *Trends in Renewable Energy*, 6:37–60, 2020. doi:10.17737/tre.2020.6.1.00111.

[18] A.G. Aberle. Thin-film solar cells. *Thin Solid Films*, vol. 517(no. 17):4706–4710, 2009. 4th International Conference on Technological Advances of Thin Films and Surface Coatings. doi:https://doi.org/10.1016/j.tsf.2009.03.056.

[19] J. P. Torres D.Leitão and J.F.P. Fernandes. "Spectral Irradiance Influence on Solar Cells Efficiency". *Energies*, 13, 10 2020. doi:10.3390/en13195017.

[20] M. Roriz et al K. Dornelles, V. Roriz. "Spectral behaviour of cool paints produced in Brazil for roof paint and their impact on the thermal comfort and energy use in buildings designed for hot climates". In Adapting to Change: New Thinking on Comfort Conference, London, April 2010. doi:10.13140/RG.2.1.4104.8802.

[21] D. Spiers. "Chapter IIB-2 - Batteries in PV Systems" . In T.Markvart A.McEvoy and L.Castañer, editors, *Practical Handbook of Photovoltaics*, pages 721–776. Academic Press, Boston, 2nd edition, 2012. doi:https://doi.org/10.1016/B978-0-12-385934-1.00022-2.

[22] L.Ramirez-Elizondo V.Vega-Garita, A.Narayan and P.Bauer. "Selecting a suitable battery technology for the photovoltaic battery integrated module". *Journal of Power Sources*, vol. 438, 2019. doi:10.1016/j.jpowsour.2019.227011.

[23] C. Zhang X. Hu, C. Zou and Y. Li. "Technological Developments in Batteries: A Survey of Principal Roles, Types, and Management Needs". *IEEE Power and Energy Magazine*, 15:20–31, September 2017. doi:10.1109/MPE.2017.2708812.

[24] Li-ion vs. Other Chemistries. [Online] https://news.inventuspower.com/blog/li-ion-vs.-other-chemistries. Accessed: january 2022.

[25] Battery Cell Comparison. [Online] https://www.epectec.com/batteries/cell-comparison.html. Accessed: june 2022.

[26] Li-S Energy Battery. A Better Battery For A Better World. [Online] https://www.lis.energy/site/li-s-energy-applications/li-s-energy-battery. Accessed: june 2022.

[27] K. Zeb et al A. Muthusamy, K. Raghavendra. "A Comprehensive Review of DC–DC Converter Topologies and Modulation Strategies with Recent Advances in Solar Photovoltaic Systems". *Electronics*, vol. 9(1), 2020. doi:10.3390/electronics9010031.

[28] T. M. Undeland N. Mohan and W. P. Robbins. *Power Electronics: Converters, Applications, and Design*. Wiley, 3rd edition, 2003.

[29] M. Kamran. "Chapter 3 - Power electronics for renewable energy systems". In *Renewable Energy Conversion Systems*, pages 53–108. Academic Press, 2021. doi:https://doi.org/10.1016/B978-0-12-823538-6.00001-4.

[30] I. Barbi. *Modelagem de conversores CC-CC empregando modelo médio em espaço de estados*. Florianópolis, author edition, 2015.

[31] Compound semiconductors: SiC and GaN. [Online] https://www.semicon.sanken-ele.co.jp/en/guide/GaNSiC.html. Accessed: april 2022.

[32] J.W. Milligan et al R.S.Pengelly, S.M Wood. "A Review of GaN on SiC High Electron-Mobility Power Transistors and MMICs". *IEEE Transactions on Microwave Theory and Techniques*, vol.60(no.6):1764–1783, 2012. doi:10.1109/TMTT.2012.2187535.

[33] A. Dolara, R. Faranda, and S. Leva. "Energy Comparison of Seven MPPT Techniques for PV Systems". *Journal of Electromagnetic Analysis and Applications*, 01:152–162, 2009. doi:10.4236/jemaa.2009.13024.

[34] D. P. Hohm and M. E. Ropp. "Comparative study of maximum power point tracking algorithms. *Progress in Photovoltaics: Research and Applications*, 11:47–62, 1 2003. doi:10.1002/pip.459.

[35] H. S. Lee and J. J Yun. "Advanced MPPT algorithm for distributed photovoltaic systems". *Energies*, vol. 12, September 2019. doi:10.3390/en12183576.

[36] A. M. Othman H. A. Gabbar and M. R. Abdussami. "Review of Battery Management Systems (BMS) Development and Industrial Standards". *Technologies*, vol. 9(no. 2), 2021. doi:10.3390/technologies9020028.

[37] D. Andrea. *Battery Management Systems for Large Lithium-Ion Battery Packs*. Artech House, 2010.

[38] G. Abad and D. Garrido. "Section 7.8 - Battery management systems (BMS)". In *Power Electronics and Electric Drives for Traction Applications*. Wiley, 2017.

[39] B. Hauke. Basic Calculation of a Buck Converter's Power Stage. Technical report, Texas Instruments, 2015.

[40] M. Xie. "How to select input capacitors buck converter". *Analog Applications Journal*, 2016.

[41] Analog Devices. LTC4444 High Voltage Synchronous N-Channel MOSFET Driver. [Online] https://www.analog.com/en/products/ltc4444.html#product-overview. Accessed: april 2022.

[42] AEC-Q100 Automotive standard. [Online] www.renesas.com/us/en/products/automotive-products/aec-q100. Accessed: january 2022.

[43] D. Bručas D. Udris and R. Pomarnacki. "Reliability Improvement of Power Distribution System for UAV". *Electronics*, 8(6), 2019. doi:10.3390/electronics8060636.

[44] G. K. Fourlas and G. C. Karras. "A survey on fault diagnosis and fault-tolerant control methods for unmanned aerial vehicles". *Machines*, 9, September 2021. doi:10.3390/machines9090197.

[45] H. Pentti and A. Helminen. Failure mode and effects analysis of software-based automation systems. Technical report, Radiation and Nuclear Safety Authority (STUK), August 2002.

[46] B. S. Dhillon. "Chapter 6 - Failure Modes and Effect Analysis" . In *Design Reliability: Fundamentals and Applications*. CRC Press, 1999. doi:https://doi.org/10.1002/qre.430.